UNIVERSITAT DE BARCELONA

Wave propagation in metamaterials mimicking spacetime geometry: black holes and cosmic strings

Isabel Fernández Núñez

A thesis submitted for the degree of
Doctor of Philosophy
Barcelona, 2018

Wave propagation in metamaterials mimicking spacetime geometry: black holes and cosmic strings

Isabel Fernández Núñez

Departament de Física Quàntica i Astrofísica

Universitat de Barcelona

Universitat de Barcelona

ICCUB Institute of Cosmos Sciences

Excelencia María de Maeztu

Wave propagation in metamaterials mimicking spacetime geometry: black holes and cosmic strings, PhD thesis

Wave propagation in metamaterials mimicking spacetime geometry: black holes and cosmic strings

Una memòria presentada per

Isabel Fernández Núñez

a la Facultat de Física de la Universitat de Barcelona per optar al grau de Doctor en Física. Aquesta tesi ha estat preparada sota la supervisió de

Dr. Enric Verdaguer Oms

i

Dr. Oleg Bulashenko

i sota la tutela de

Dr. Domènec Espriu Climent

tots tres del departament de Física Quàntica i Astrofísica de la Universitat de Barcelona.

Barcelona, abril de 2018

A Daniel, María, Manuel y Lolita

"If I had a world of my own, everything would be nonsense.
Nothing would be what it is, because everything would be what it isn't.
And contrary wise, what is, it wouldn't be.
And what it wouldn't be, it would. You see?"

– Lewis Carroll,
Alice's Adventures in Wonderland & Through the Looking-Glass

Acknowledgments

Primero, me gustaría agradecer a Oleg por haberme guiado y apoyado durante estos años. Todo empezó con un pequeño trabajo de final de grado que fue evolucionando en distintos proyectos que han culminado en esta tesis. Gracias por todo lo que me has enseñado. A l'Enric, gràcies per estar sempre disponible i haver supervisat la nostra feina.

A mis padres, gracias por haberme dado siempre lo mejor, animarme a aprender y haber hecho posible que llegue hasta aquí. Gracias, Papá, por los pequeños experimentos en casa, los programas Clic y haber sido la primera persona en hablarme de los novedosos "metamateriales". Creo que todo ha tenido un poco que ver con lo que ha venido luego. Gracias, Mamá, por haber sido siempre un ejemplo a seguir y por haberme enseñado que "la experiencia es la madre de la ciencia". A Marta le agradezco todas las conversaciones, bromas, tonterías, noticias, recomendaciones y hasta los conciertos privados. Gracias por todo vuestro apoyo y cariño. També m'agradaria recordar a la meva altra família *química*, Núria i Àngel.

La sort va voler que el primer dia de carrera em trobés a la Laia i el Marc. Llavors no podíem imaginar totes les experiències que viuríem amb la resta de *croquetetes*: Albert, Ana, Dani, Laura, Manel, Marta, Oriol. Mai oblidaré les classes, els dinars, les tardes a l'hemeroteca, les alegries i angoixes compartides, les tertúlies, els viatges... Gràcies per fer que cada moment sigui una aventura i per estar sempre al meu costat.

Manel, gràcies per haver aguantat cinc anys seient a la meva esquerra i per haver seguit sent el meu crític i guia des de la distància. T'agraeixo molt haver estat sempre disponible per parlar de qualsevol cosa, resoldre dubtes científics, estètics, lingüístics i per les correccions a aquesta tesi. Gràcies per, junt amb la Raquel, haver escoltat les meves preocupacions i haver-me recolzat, sempre amb humor.

Laura i Pere, gràcies pels *cafès de germanor*, els debats, els passeigs per la ciutat, les tardes de platja i per escoltar-me més del que de vegades em penso. Us agraeixo molt el vostre suport i confiança durant tants anys, però especialment en la recta final d'aquesta tesi.

Agradezco también haberme podido encontrar en casa con Rafa y Dani para poder compartir nuestros problemas y alegrías del día a día del doctorado. Gracias por descubrirme mi ciudad con restaurantes, bares y paseos. Gracias, Juanlu, por haber sido la conexión que lo hizo posible y por haber sido amigo mío durante tantos años pese a la distancia. Víctor, crec que ja puc respondre la teva pregunta diaria de "Quan acabes la tesi?".

Muchas gracias a *mis amigos de física* Albert, Marina, Carla, Adriana, Vicente, Nuria, Eli, Miquel, David, Genís, Iván sin los que la hora de comer hubiera sido mucho más aburrida. Ha sido un placer compartir tantos momentos con vosotros.

M'agradaria agrair també el bon ambient al despatx 4.10 aquests anys. Gràcies Ignacio, Guille, Pere, Javi, Nikos i Jairo per les fustracions compartides, els dubtes resolts i els necessaris moments de distracció. Nikos and Jairo, thank you for having dealt with my *cheerfulness* these past months and for the outings, lunches and dinners with Sotiris and Elena.

Aquesta tesi ha estat elaborada amb el finançament de l'ajut APIF-UB (2015-2018).

Resum

Gravitació anàloga i metamaterials

En ciència, no és sorprenent trobar que dos fenòmens estan descrits per la mateixa equació. Quan això passa, podem fer servir els conceptes associats a un cas per fer-los servir en l'altre. D'aquesta manera, l'enfocament que donem al nostre problema pot canviar.

En el cas de la gravitació anàloga, s'estudien sistemes que reprodueixen algun dels aspectes de la física dels espaitemps corbats. Els models anàlegs estudiats sovint ofereixen la possibilitat de realitzar experiments que no es podrien fer d'una altra manera. Per exemple, en un laboratori es podrien controlar alguns dels paràmetres que la natura fixa per l'objecte cosmològic en qüestió. Depenent de les característiques que es volen estudiar, els models de gravitació anàloga s'han basat en diferents sistemes físics: ones sonores en fluids, condensats de Bose-Einstein o fotònica, entre altres [1–3]. De fet, un dels casos més senzills és el del forat negre acústic, que va ser proposat per Unruh el 1981 [4]. Un forat negre és una regió de l'espaitemps on l'atracció gravitatòria és tan forta que res (ni partícules ni llum) no pot escapar de dins d'ella. La frontera d'aquesta regió és el que s'anomena "horitzó d'esdeveniments". L'anàleg sonor es basa en la idea que si en un fluid en moviment hi ha una regió supersònica, és a dir, una regió on la velocitat del fluid és superior a la velocitat de propagació del so en el medi, les ones sonores s'hi veuran atrapades.

Aquesta tesi se centra en l'analogia entre els materials i la geometria de l'espaitemps. Una distribució espacial de la permitivitat i permeabilitat (que regeixen la resposta electromagnètica d'un medi a un camp extern) pot fer que la llum es corbi com si estigués en un altre sistema de coordenades. El mètode matemàtic que permet trobar l'expressió d'aquests paràmetres per a una transformació geomètrica concreta és l'*òptica de transformació* [5–8]. De fet, es pot demostrar que la propagació d'ones electromagnètiques en l'espai buit corbat per un camp gravitatori és formalment equivalent a la propagació en un medi en un espaitemps Minkowskià [9–17].

Tanmateix, no va ser fins l'aparició dels *metamaterials* a principis de segle [18] que la realització d'aquests medis exòtics es va considerar assolible en la pràctica. Existeixen diferents definicions de "metamaterial" però certes característiques apareixen sovint en la seva descripció [6, 8, 19–21]:

- Els metamaterials són materials artificials compostos. Els seus elements estructurals normalment s'anomenen "meta-àtoms".
- Per poder definir propietats macroscòpiques del material (com la permitivitat o la permeabilitat), cal que els meta-àtoms i la separació entre ells sigui inferior a la longitud d'ona de la radiació incident.
- Les propietats que manifesta el metamaterial no es troben a la natura o als seus elements constituents.

Els metamaterials, doncs, ofereixen l'oportunitat de dissenyar medis on la llum té comportaments extraordinaris i han donat lloc a aplicacions ben diverses: materials amb índex de refracció negatiu [18, 22, 23], invisibilitat [24], superlents [25–30] o metamaterials hiperbòlics [31–33]. Aquests desenvolupaments també han inspirat metamaterials per controlar altres tipus d'ones com sonores [34,35] o sísmiques [36]. Deguda a aquesta versatilitat, el camp de l'òptica de transformació va tornar a guanyar popularitat amb els metamaterials i des de llavors diversos fenòmens de la relativitat general han inspirat el seu estudi des d'aquest punt de vista: forats negres òptics [37–44], espaitemps de Schwarzschild [45–49], espaitemps de Kerr [50], cordes còsmiques [51–55], forats de cuc [56, 57], radiació de Hawking [58, 59], etc. En aquesta tesi hem fet servir aquesta teoria per estudiar en detall dos objectes estàtics: un forat negre i una corda còsmica.

Forat negre

Poc després que Einstein publiqués la seva teoria de la relativitat general en forma d'equacions de camp que relacionaven la matèria i l'energia amb la curvatura de l'espaitemps [60], Schwarzschild va trobar-ne la primera solució no-trivial [61]. Aquesta descriu el camp gravitatori produït per una distribució esfèrica de massa, però a més, també pot correspondre a un forat negre ja que presenta un horitzó d'esdeveniments a un cert radi r_s, el radi de Schwarzschild.

Donada la simetria d'aquesta mètrica, decidim treballar primer amb el cas general d'un espaitemps estàtic amb simetria esfèrica i després aplicar els resultats al cas concret del forat negre de Schwarzschild. Fent servir les equacions d'òptica de transformació de Plebanski [13], podem trobar quina permitivitat i permeabilitat un metamaterial anisòtrop ha de tenir per simular aquest espaitemps. Tot i això, en aquest cas es pot fer una transformació de coordenades per tal d'obtenir la mètrica en una forma *conforme* a l'espai pla. D'aquesta manera, el metamaterial equivalent que s'obté és isòtrop i només cal definir un índex de refracció inhomogeni $n(r)$ per caracteritzar-lo. Aquest cas serveix d'exemple per mostrar que la transformació de geometria a medi no és única i l'elecció de diferents coordenades dóna lloc a diferents materials anàlegs [45,62]. Aquesta llibertat permet triar les coordenades i el material més adients per a cada situació. No obstant això, els observables físics com l'angle de deflexió haurien de ser independents del sistema de coordenades triat i, per tant, del metamaterial.

Un cop hem derivat l'expressió dels paràmetres del medi pel cas general, es pot particularitzar per la mètrica de Schwarzschild i obtenir els dos medis: un anisòtrop i un isòtrop. Estudiem la propagació d'un feix gaussià en tots dos realitzant simulacions numèriques. D'aquesta manera podem comparar els resultats amb les geodèsiques que segueix la llum en el camp gravitatori del forat negre però també observem els fenòmens ondulatoris que van més enllà de l'òptica de raigs. Tant en el cas anisòtrop com isòtrop obtenim molt bona coincidència entre les simulacions i les trajectòries teòriques, que estan simplement determinades pel paràmetre d'impacte del feix de llum. De fet, trobem que l'expressió de l'Hamiltonià òptic i el que descriu les geodèsiques de llum en el context de relativitat són idèntiques. A més, veiem que la permitivitat i la permeabilitat estan relacionades independentment amb el terme de dilatació temporal de la mètrica o amb els coeficients espacials, segons la polarització del camp electromagnètic que considerem.

Finalment, cal destacar que els metamaterials que imiten el comportament d'un forat negre podrien tenir diverses aplicacions en el camp de la fotònica. Donat que absorbeixen la radiació provinent de qualsevol lloc (només depenent del paràmetre d'impacte), sovint se'ls anomena "absorbents electromagnètics omnidireccionals" [37–42, 44]. Per exemple, aquests dispositius es podrien fer servir en sistemes fotovoltaics o com a trampes per fotons en muntatges òptics [37, 38, 63].

Corda còsmica

Les cordes còsmiques són defectes topològics unidimensionals que es podrien haver format durant alguna transició de fase que hauria trencat la simetria en l'univers primigeni [64–66]. Els efectes gravitacionals que aquest tipus d'objecte no-compacte té sobre les ones que es propaguen en el seu entorn és ben diferent del que pot passar en el cas d'una lent gravitatòria compacta. L'objecte compacte té una mida característica que s'ha de comparar amb la longitud d'ona de la radiació incident per determinar si els efectes ondulatoris són rellevants i si serien detectables [67–69]. En canvi, el paràmetre característic de la corda còsmica no és una mida sinó un angle Δ, que és proporcional a la densitat lineal de la corda. Per aquest motiu, els efectes de difracció i interferència poden ser del mateix ordre de magnitud que els termes corresponents al límit d'òptica geomètrica. Per tant, és important determinar com es propaguen les ones en l'espaitemps de la corda i no simplement quedar-se en aproximacions a primer ordre.

La corda té una topologia cònica que també es troba en defectes a altres sistemes físics com sòlids elàstics o cristalls líquids en els quals s'acostumen a anomenar "disclinacions" [70–77]. La geometria cònica es pot interpretar com un espai pla al qual se li ha tret o afegit un tascó. Això dóna lloc a un espai amb curvatura positiva o negativa, respectivament. El cas de la corda còsmica correspon a l'extracció d'un tascó d'angle 2Δ. De fet, fem servir aquesta propietat per descriure la propagació d'ones en l'espai cònic. Podem tractar cada cara del tascó com una pantalla semi-plana que difracta l'ona incident. D'aquesta manera reduïm el problema de la corda al problema canònic de Sommerfeld de difracció sobre un semi-pla [78]. Després només cal combinar adequadament les expressions per a cada cara amb la transformació de coordenades corresponent.

Fem servir teories asimptòtiques de difracció per tal de resoldre el cas del semi-pla de manera senzilla ja que d'aquesta manera s'obtenen expressions fàcils d'interpretar físicament. En concret, aplicant la teoria geomètrica de difracció [79], el camp en un cert punt P de l'espaitemps de la corda es pot arribar a expressar com la suma de quatre termes: dues ones que van directament de la font al punt P (que corresponen al límit d'òptica geomètrica) i dues ones difractades que també van de la font al punt P però tocant la corda, seguint el camí més curt. Gràcies a aquesta expressió, podem interpretar els patrons ondulatoris que s'observarien com a interferències d'aquestes quatre ones. Malgrat això, aquesta solució presenta divergències en certs punts. Per obtenir un model regular en tot l'espai, fem sevir la teoria asimptòtica uniforme [80, 81], que amb pocs termes dóna resultats precisos. Aquestes teories presenten un clar avantatge respecte les altres solucions que es poden trobar a la literatura en forma integral [82] o com a sèries infinites [83].

Així mateix, en aquest context es pot introduir la noció de les "zones d'observació de Fresnel", que estan relacionades precisament amb els màxims de difracció del camp. Aquestes zones ens poden ajudar a localitzar les regions – en espai o freqüència – on els efectes ondulatoris són més grans i, per tant, es poden fer servir per determinar les condicions d'observació òptimes. En aquest sentit, obtenim també el patró de difracció característic de la corda. Remarquem que aquests resultats són vàlids tant per ones electromagnètiques com ones gravitacionals (en un gauge determinat). Per aquest motiu, trobem esperançador el futur que la primera detecció d'ones gravitacionals pel Laser Interferometer Gravitational-Wave Observatory (LIGO) [84] va obrir. Amb aquest tipus d'observacions altres objectes que fins ara han estat invisibles, com les cordes còsmiques, podrien ser detectats.

La topologia cònica també es pot estudiar amb l'òptica de transformació. De la mateixa manera que hem fet pel cas del forat negre, trobem la permitivitat i permeabilitat d'un metamaterial

anàleg a la corda còsmica. Hi estudiem la propagació de la llum mitjançant simulacions numèriques. Observem els efectes característics de la corda, com la regió d'imatges dobles. També comprovem que s'obtenen els patrons que hem predit amb la teoria geomètrica de difracció i que hi ha un bon acord amb la teoria asimptòtica uniforme. A més, també s'han trobat possibles aplicacions a aquest tipus de metamaterials com a *beam-splitters* [52, 85] o com a dispositius que sempre desvien el mateix angle un feix incident [52].

Contents

CHAPTER 1

Introduction

1.1 Analogue gravity

As physicists, we are used to recurring to analogies when we try to explain in layman's terms a physical concept to our friends and families. We begin from a familiar situation similar to what we try to describe to ease our way to a more complex idea. These conversational comparisons might be vague, but in physics we find many instances of common mathematical analogies. For example, the ever-present Poisson and Laplace equations are satisfied by different physical fields that lead us to defining homologous variables [86]. A good analogy can make us look at a problem from a different point of view. In that way, ideas may be transferred from one field of science to another, allowing to model new phenomena after previous, well-studied ones.

In the case of analogue gravity we are concerned with the study of systems that mimic aspects of the physics of curved spacetimes. Even if it mostly deals with reproducing celestial mechanics, the chosen analogous models often offer the possibility to perform experiments that otherwise would not be possible. These models have ranged from sound waves in fluids to photonics [1–3]. Given their diverse nature, different features of general relativity can be investigated with each of them.

In acoustics, we find the simplest black hole analogue, which was first noted by Unruh in 1981 [4]. A black hole is a region of spacetime in which the gravitational attraction is so strong that neither particles nor light can escape from inside it. The event horizon is the boundary of the black-hole region. The main idea behind its sonic analogue is that if a moving fluid presents a supersonic region, sound waves will be trapped in it. This apparent equivalence is also true at a deeper level given that a scalar field in a curved spacetime satisfies the same equations as sound waves in flowing fluids (under the appropriate conditions) and an acoustic metric that governs sound propagation emerges [1, 4, 87]. Once the analogy was established, the next natural step was to describe how common notions related to cosmological black holes such as the horizon, superradiance or Hawking radiation were to manifest in the acoustic model [1, 2, 87], focusing on potential experiments with superfluid Helium [88, 89] or Bose-Einstein condensates (BECs) [90–92]. It was not until 2009 [93] that a BEC-based sonic black hole (also called "acoustic black hole" or "dumb hole") was experimentally realised. In this case, they used a step-like potential to accelerate the flow of the condensate to supersonic velocities, creating a region that traps sonic perturbations.

We can also find an event-horizon analogue in gravity waves in a shallow basin filled with a liquid. Under certain conditions, the surface waves of the fluid are seen to be described by an effective metric equivalent to the acoustic case [94]. The main advantage of this proposal is that the velocity of the surface waves can be adjusted simply by varying the depth of the basin and therefore, it is easily realizable in the laboratory [95]. Given its classical nature, quantum effects are not expected to be observed with this type of model. To do that, one should refer to other systems such as the aforementioned superfluid Helium and BEC-based analogues or graphene models [73, 96, 97], for instance.

This thesis is focused on the analogy between media and geometry. Before going into mathematical detail, one can already get the intuition that there are similarities in the behaviour of light in a medium and in a gravitational field. On the one hand, according to Fermat's principle, to go from one point to another, light rays follow extremal paths. In the case of an inhomogeneous medium, that path might be curved. On the other hand, electromagnetic and gravitational waves can be distorted due to spacetime curvature (the effect called "gravitational lensing"). As will be exposed in Chapter 2, it can be shown that the propagation of electromagnetic waves in a curved vacuum manifold is formally equivalent to the propagation in a medium embedded in a flat Minkowski spacetime [9–17]. This analogy combined with the advances in the design of artificial materials with exotic properties (known as "metamaterials") [6–8, 19], has motivated extensive research in optical devices inspired by cosmological models. Apart from providing another point of view and the possibility of experimental realization, the analogue models have also offered new applications and challenges to the optics and metamaterial engineering community.

1.2 Scope

In the present work, we study two objects: the analogues of a Schwarzschild black hole (as an example of a static spherically symmetric spacetime) and a cosmic string. Regarding optical black holes, there have been two approaches to the research. The best method to reproduce the behaviour of light in the exterior of a black hole would be using transformation optics, the mathematical theory behind the analogy between media and geometry we have introduced in the previous section (and will be explained in detail in Chapter 2). In this way, which is the one followed in this thesis, one models a particular black hole spacetime in a metamaterial [45–50]. This generally requires metamaterials with anisotropic permittivity and permeability, which are more difficult to manufacture. Therefore, researchers began studying simpler designs inspired by the deflection of light in gradient-index materials (GRINs), that is, inhomogeneous media with a spatially varying refractive index (this is the case, for instance, of the crystalline lens of the human eye). In this case, the metamaterial can be characterized just by an isotropic refractive index. With an appropriately designed GRIN, one can either deflect or capture light by an absorber in a way inspired by black-hole behaviour. These are generally referred to by authors as "omnidirectional electromagnetic absorbers" given that they could absorb nearly all light hitting them from every direction [37–44].

Cosmic strings are one-dimensional topological defects that may have been formed during a phase transition in the early universe [64–66]. They present a conical topology that gives rise to gravitational lensing effects such as the appearance of double images. This is due to the fact that light rays are deflected by the same angle, independently of the impact parameter [98]. Double images can be explained in the geometrical optics limit, however, wave effects in this setting such as interference and diffraction are significant and should be taken into account. Wave diffraction by a non-compact object like this is different from that on a compact-mass gravitational lens. The compact object has a characteristic size that should be compared with the wavelength of

the incident radiation in order to determine if wave effects would be detectable [67–69]. In the case of the cosmic string, the relevant parameter is an angle, the *deficit angle*, which is proportional to the linear mass of the string. As a result, diffraction effects can be of the same order as the geometrical optics terms. This type of linear defect is also found in other systems that have the same conical topology such as disclinations (or wedge dislocations) in nematic liquid crystals, graphene or elastic solids [70–77]. Moreover, one can make use of transformation optics to characterize a medium that would mimic the cosmic string spacetime. These optical devices with conical singularities are also expected to have applications in photonics as beam-steering elements [52]. Despite the importance of wave effects in all the different systems with conical topology, not many detailed studies dealing with wave propagation in this geometry are known [82, 83, 99–101].

We believe that the contents of this thesis are multidisciplinary and can be of interest to several scientific communities. Transformation optics researchers will find a detailed study of wave propagation in the analogous metamaterials. The considered media could have potential optical applications that may attract the attention of those working in photonics. The analytical theory we obtain for wave propagation in the cosmic string spacetime can be used to study the gravitational lensing of electromagnetic and gravitational waves. As we have pointed out,the conical geometry of the cosmic string is also present in condensed matter systems, therefore, our results could be applied to those cases as well.

1.3 Objectives

One of the goals of this thesis is to determine the constitutive relations of metamaterials mimicking two types of static spacetimes: one with spherical symmetry and the other with conical geometry. Both are motivated by cosmological cases corresponding to solutions to Einstein's field equations, that is, the Schwarzschild black hole [61] and the cosmic string [65, 102], respectively. We aim to study the propagation of electromagnetic waves in the resulting media by means of numerical simulations and compare them with analytical theories from general relativity. In that way, we can observe that wave propagation in an appropriately designed metamaterial is equivalent to that under the influence of a gravitational field.

For the case of the black hole, we want to compare a Gaussian beam propagating in the metamaterial with the null-geodesics (the trajectories followed by massless particles) obtained from the Hamiltonian. We also derive the optical Hamiltonian by applying the eikonal approximation to the wave equation and we find the two to be identical. We do this for both an anisotropic and isotropic analogous metamaterial given that the symmetries of the considered metric allow to perform a coordinate transformation to an isotropic form [103].

In the study of the cosmic string, our main focus is on obtaining analytical models to describe wave diffraction by the linear topological defect given that many previous studies only dealt with light rays, for which expressions can be easily calculated [52, 75, 104, 105]. We begin by examining the wave field in the geometrical optics limit. We see that the characteristic double-imaging effect of the cosmic string manifests as an amplification of the observed intensity in a certain region. Then, we apply asymptotic diffraction theories that allow us to write the wave field as the sum of a few terms while providing good accuracy. As a result, the interference and diffraction effects can be analysed in detail. For instance, these produce a modulation of the intensity giving rise to diffraction maxima and minima that can be related to the Fresnel observation zones. They can be used to determine where wave effects are more significant and, therefore, the conditions in both space and frequency domain for which the string would be easier to detect. Moreover,

we believe these results to be valid for both electromagnetic waves and gravitational waves (in an appropriately chosen gauge).

1.4 Methodology

In order to achieve the goals of this thesis, we will make use of the following tools:

- Transformation optics, in particular Plebanski's formulation of the electromagnetic constitutive equations [13], to parametrize the metamatateriales analogous to spacetime geometries. In this way, the curvature caused by the gravitational field of the cosmological object is mapped to the medium parameters.
- Hamiltonian formulation, to obtain the null-geodesics in the spacetimes considered. These are equivalent to the light rays in the geometrical optics limit propagating in the analogous metamaterials.
- Asymptotic diffraction theories, to describe wave propagation in the cosmic string spacetime (i.e. in conical geometry). In particular, we use the geometrical theory of diffraction and the uniform asymptotic theory in a Minkowskian virtual space. Our approach allows to interpret analytically the numerical results with just a few terms, which contrasts with previous studies that involved expressions in the form of integral representation [82] or infinite series [83].
- Numerical simulations of wave propagation in the equivalent media. We use the COMSOL Multiphysics software package to solve the electromagnetic wave equation by means of a finite element method. Therefore, the results go beyond the limit of ray optics (or, equivalently, null-geodesics) and allow to observe the whole wave picture.

1.5 Outline

This thesis is divided in three main chapters and one final closing chapter. In Chapter 2, we give a brief introduction to metamaterials and how they are used in the context of analogue gravity. In that sense, we give an overview of hyperbolic metamaterials and introduce the theory of transformation optics. We stablish the framework of the analogy between media and curved spacetimes that will be used in later chapters. In Chapter 3 we apply the theory to the Schwarzschild black hole. We begin by analysing the general case of a static spherically symmetric spacetime, which can be transformed from an anisotropic form to isotropic coordinates. We give the expression of the corresponding medium parameters (for both isotropic and anisotropic cases). Then, we use these expressions to focus on the Schwarzschild black hole and provide the results of the numerical simulation of light propagation in the two equivalent materials. We compare the numerics with the null-geodesics in the Schwarschild spacetime obtained from the Hamiltonian. We also contrast our approach based on transformation optics with other optical black holes based on GRINs. In Chapter 4, we address the problem of wave propagation in conical geometry, motivated by its cosmological analogue: the cosmic string. As done in the previous chapter, we obtain the permittivity and permeability of media that mimic the geometry of this kind of topological defect. We provide the numerical simulation of a cylindrical wave propagating in the metamaterial. But before, in order to interpret the full-wave results, we study the wave equation in the cosmic string spacetime and examine in detail different asymptotic approximations that

allow us to express the wave field as the sum of a few terms. (We do this for both a line source at a finite distance and a infinitely distant source.) Moreover, we define the Fresnel observation zones, which are associated to the diffraction maxima. They help localize the regions of highest amplification of the wave field due to the string. Finally, the conclusions and future perspectives are discussed in Chapter 5.

To complement the material provided in the main chapters, additional information is given in the appendices. In Appendix A we give an alternative formulation of the medium parameters for the Schwarzschild spacetime (suggested in Chapter 3) and provide the corresponding numerical simulations. In Appendix B we give a summary of the different models of the diffraction by a conducting half-plane screen used in Chapter 4 to derive the wave field in the cosmic string spacetime. We show the corresponding plots as well to be compared with the case of conical geometry. In Appendix C we offer the numerical simulations of the propagation of a cylindrical wave in metamaterials mimicking cosmic string topology for a wider range of parameters than those used in Chapter 4 and, for completeness, the propagation of a Gaussian beam.

1.6 List of publications

The work presented in this thesis has been published in the following papers:

- I. Fernández-Núñez and O. Bulashenko, *Anisotropic metamaterial as an analogue of a black hole*, Phys. Lett. A **380**, 1 (2016).
- I. Fernández-Núñez and O. Bulashenko, *Wave diffraction by a cosmic string*, Phys. Lett. A **380**, 2897 (2016).
- I. Fernández-Núñez and O. Bulashenko, *Emergence of Fresnel diffraction zones in gravitational lensing by a cosmic string*, Phys. Lett. A **381**, 1764 (2017).
- I. Fernández-Núñez and O. Bulashenko, *Wave propagation in metamaterials mimicking the topology of a cosmic string*, J. Opt. **20**, 045603 (2018).

CHAPTER 2

Metamaterials and transformation optics

2.1 Introduction to metamaterials

One of the hot topics of modern technology is to build artificial materials whose permittivity and permeability can be engineered by incorporating structural elements of subwavelength sizes. As a result, one can create hybrid materials (called metamaterials) designed to exhibit exotic electromagnetic properties [6–8, 19]. The prefix "meta" comes from the Greek word "μετα" meaning "beyond". In that sense, metamaterials are said to be beyond conventional materials [6]. Ever since the term first appeared at the beginning of the century [18], several key features repeatedly appear in its definition [6, 8, 19–21]:

- Metamaterials are artificial composite materials. Its structural elements are generally referred to as "meta-atoms".
- In order to define macroscopic properties, the meta-atoms and the distance between them must be significantly smaller than the wavelength of the incident radiation (see Fig. 2.1).
- The properties the metamaterials exhibit are not found in nature or in their constitutive elements.

This contrasts with the anomalous light propagation seen in photonic crystals, whose periodic structure produces photonic band gaps preventing photons from propagating in certain directions (for a certain bandwidth) [106]. Similarly to X-rays in their solid-state analogue, the dominating effect in this case is Bragg diffraction. This is primarily due to the similar size of the unit cells (and periodicity) and the wavelength of the external radiation (see Fig. 2.1). In order to define macroscopic medium parameters such as relative permittivity ε and permeability μ as done with metamaterials, the inhomogeneities in the composite (i.e. the meta-atoms) must be sub-wavelength in scale [6, 8, 22, 107].

The first motivation behind designing metamaterials was to observe the unusual propagation of light in media with simultaneously negative permittivity and permeability theoretically investigated by Veselago in 1968 [108]. He showed that the consequences of this situation required a negative index of refraction n. In negative index materials (NIMs), group velocity and phase velocity are antiparallel, that is, phase and energy propagate in opposite directions. The electrodynamic consequences include reversed Doppler and Cherenkov effects and anomalous refraction. The permittivity and permeability summarize the response a material has when exposed to an

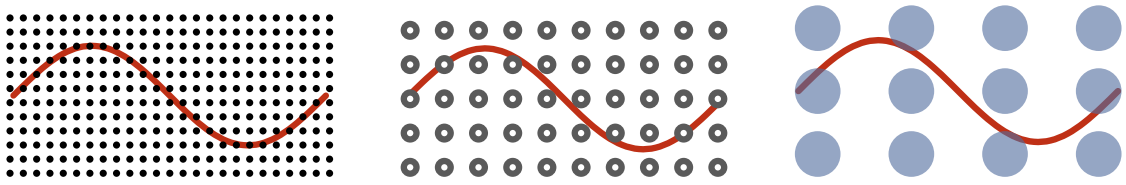

(a) Material. (b) Metamaterial. (c) Photonic crystal.

Figure 2.1: (a) A periodic array of atoms constitutes a common material. (b) In a metamaterial, these are substituted by meta-atoms, which must be much smaller than the wavelength of the incident radiation. The inhomogeneities are not "perceived" by the radiation and macroscopic medium parameters can be defined. (c) The unit cells of a photonic crystal are on the same order of magnitude than the wavelength. Depending on the structure of the crystal, certain wavelengths will not be allowed to propagate (*photonic band gaps*) and others will (*modes*). This phenomenon is equivalent to Bragg diffraction of X-rays in crystalline solids.

external electric or magnetic field [109]. In conventional media, these parameters are dependent on their molecular and crystalline structure. In metamaterials, these properties arise from the meta-atoms. As Pendry et al. proposed [110, 111], plasmon modes and resonances in the elements of a composite material can be used to generate a medium with unusual electromagnetic properties. Inspired by these ideas, in 2000, Smith et al. [18] designed a metamaterial using a periodic array of wires and split-ring resonators of some mm in size that led to simultaneously negative ε and μ within a certain band of the microwave frequencies.

Given that metamaterials attain their properties from resonances, they are highly dispersive (i.e. the medium parameters are frequency-dependent) [6–8, 107]. During the last decade, the size of the meta-atoms has been tremendously reduced owing to the advances in the control of electromagnetic phenomena down to the nanoscale and, consequently, the operating frequency has increased, even reaching the optical domain. However, optical devices should consist of large-scale 3D metamaterials and the manufacturing of such still remains a challenge [6, 8, 112].

It rapidly became clear that the potential of metamaterials went beyond NIMs and nowadays, their fabrication method, structure, periodicity and composition are as diverse as their applications [6–8, 113]. For electromagnetic waves, they offer opportunities for realizing exotic phenomena such as negative refraction [18, 22, 23], cloaking (invisibility) [24], super-lenses for sub-wavelength imaging [25–30] or hyperbolic (indefinite) dispersion [31–33] (see Sec. 2.3 for further details). The developments in electromagnetic metamaterials inspired the emergence of metamaterials aimed at controlling propagation of other types of waves. Examples include an acoustic analogue to Veselago's NIM [34], a cloak for ultrasound waves [35], a seismic metamaterial to mould surface waves [36] or conical refraction for elastic waves [114], among others.

In the recent years, metamaterial research has been focused on reconfigurable or tunable devices. That is, metamaterials whose electromagnetic properties may be changed in space and time by modifying the geometry, structure or individual unit cells. This unprecedented control can allow, for instance, to shift the operating bandwidth of the device, to spatially vary its medium parameters or to alter the intensity and polarization of propagating waves [115, 116].

Almost two decades ago, when the subject of metamaterials arose, it was difficult to imagine how vast and diverse it would become. Thus, it is hard to predict all the possibilities that are yet to come. However, we can say that, despite the remaining challenges and limitations, innovative ideas and rapid technological development give metamaterials a very promising future.

2.2 Overview of metamaterial design and fabrication

Many tasks are involved in metamaterial research: theoretical models predicting exotic phenomena, design proposals and the actual manufacturing of novel structures. Even though this thesis is focused on theoretical aspects, the possibilities of experimental realization should always be taken into account. For this reason, in this section we provide a brief presentation of the different elements involved in the fabrication of electromagnetic metamaterials.

The artificial electromagnetic response of a metamaterial can be achieved with a great variety of structures. A simple but useful model is that of a layered metal-dielectric composite [see Fig. 2.2(a)]. The electrical permittivity of the bulk can be related to that of the constitutive elements and the thickness of the layers [6,21]. An artificial permittivity can also be engineered with an array of wires (the *wire medium* or *rodded medium*, which can be two- or three-dimensional). We illustrate a 2D example in Fig. 2.2(b). These structures were already investigated by Rotman in the 1960s [117] to simulate plasma but regained popularity with metamaterials, particularly NIMs [18, 110]. The wires are designed to exhibit collective electron oscillations at a certain effective plasma frequency directly related to the geometry of the rodded medium [19, 110]. In this way, the metamaterial can be tuned to exhibit the desired permittivity (which is extremely dependent on the frequency) at practically any frequency range from the microwave region to the optical range [6]. Regarding magnetism, split-ring resonators (SRRs) have become the paradigm of meta-atoms. SRRs are concentric almost-closed metallic[1] loops with the gaps in opposite directions [see Fig. 2.2(c)]. The structure of the SRR leads to a resonant capacitance (due to the separation between the rings) and inductance (arising from the gap of the rings). When a time-varying magnetic field is applied parallel to the axis of the rings of a SRR, it induces a current that generates a field that may enhance or oppose the incident field, depending on the frequency. The SRR can be put into an array and, given that they respond to an external magnetic field, a frequency-dependent effective permittivity determined by the nature and geometry of the rings can be defined [6, 18, 21, 111]. Different structures and meta-atoms can be combined in order to obtain the desired medium parameters. For instance, SRRs and a wire medium were used to achieve the simultaneously negative permittivity and permeability for the first NIM [18].

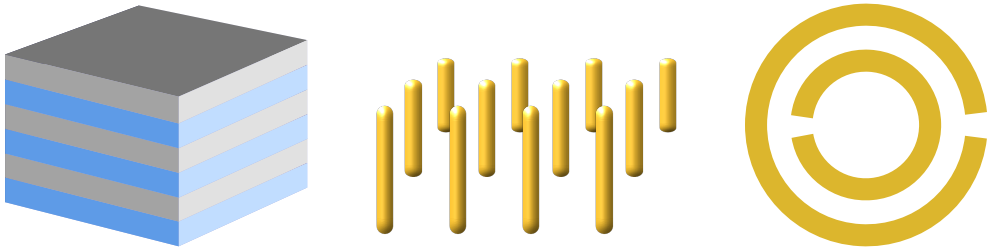

(a) (b) (c)

Figure 2.2: Illustration of a (a) layered metal-dielectric composite, (b) two-dimensional wire medium and (c) split-ring resonator.

It is clear why, from the whole electromagnetic spectrum, metamaterial engineers have chosen to work with microwave radiation many times: the meta-atoms are only required to be of some mm in size, making them fairly easy to handle. In order to manufacture an optical metamaterial, the scale has to be substantially reduced. Nanofabrication techniques such as electron beam lithography, focused ion beam milling, nanoimprint lithography or direct laser writing have all

[1] Gold is one of the preferred metals for SRRs (and meta-atoms in general) due to its stability and good performance in various nanofabrication processes. Silver is a popular choice as well [6, 8]. Other researchers have pointed towards all-dielectric metamaterials to overcome certain issues such as heat dissipation [118].

been successful in rendering structures with periodicities and features of some hundreds nm or even less [6, 8, 21, 112].

One of the most common methods for the fabrication of planar metamaterials is electron beam lithography (EBL). It employs a focused beam of electrons to generate a pattern on a surface covered with a sensitive film. Given the small de Broglie wavelength of high-energy electrons, this technique has the high resolution in the nanoscale (about 10 nm) needed for optical metamaterials. However, EBL is only used for small areas due to its high cost and long times to obtain the desired patterns [6, 8, 21, 119].

To obtain rapid results, the focused ion beam (FIB) milling approach can be used. It consists in shining a surface with a focused beam of gallium ions in order to sputter or implant atoms on it. FIB is also used to obtain 3D structures by stacking several 2D layers. (In principle, it could also be done with layers obtained by EBL, but its poor efficiency in time and money limit this possibility.) The destructive nature of the FIB process is the cause of its main drawback: the removed ions may contaminate the finished metamaterial. These impurities can affect the material properties resulting in an unpredicted performance [6, 21, 119].

For three-dimensional metamaterials with a complex geometry, direct laser writing (DLW) is one of the most popular options. It is a 3D printing technique where a ultra-fast laser beam is tightly focused in a volume of a *photoresist* (a light-sensitive material). In this way, a polymerization process via nonlinear multiphoton absorption takes place locally. The beam is controlled with a computer, allowing arbitrary polymer structures to be fabricated. Despite providing structures that are not possible for conventional lithography techniques, only a limited number of substrates can be used for DLW [6, 8, 112, 120].

Once a metamaterial is built using the most suitable method (according to its geometry and constitutive materials, it has to be characterized. That is, the medium parameters have to be determined. To do that, the heterogeneous structure of the metamaterial has to be subwavelength so it can be considered as a homogenized effective medium. There have been different proposed approaches to do the characterization. For instance, one can measure the complex transmission and reflection coefficients and relate them to the refractive index. This method, however, can lead to non-unique answers for devices with asymmetries [121]. An alternative can be making use of an effective medium theory to determine analytical expressions for anisotropic metamaterials [122].

2.3 Hyperbolic metamaterials

One case of electromagnetic metamaterials that is of interest to analogue gravity research is hyperbolic metamaterials. They are strongly anisotropic and exhibit indefinite (or hyperbolic) dispersion. It can be said that they behave as a metal in one direction and as a dielectric in the perpendicular one [8, 31].

This phenomenon can be explained by means of crystal optics, which describes the behaviour of light in anisotropic media. Consider an anisotropic permittivity tensor $\underline{\underline{\varepsilon}}$ that connects the electric field $\mathbf{E}$ and the electric displacement field $\mathbf{D}$ through the constitutive relation $\mathbf{D} = \underline{\underline{\varepsilon}}\mathbf{E}$. The tensor $\underline{\underline{\varepsilon}}$ can always be found to be diagonal in the system of the *principal axes* of the material, taking the form [33, 123, 124]

$$\underline{\underline{\varepsilon}} = \mathrm{diag}\left(\varepsilon_x, \varepsilon_y, \varepsilon_z\right). \tag{2.1}$$

The optical properties of the crystal will be significantly different depending on the values of the

dielectric constants. Accordingly, they can classified into three categories: when $\varepsilon_x = \varepsilon_y = \varepsilon_z$, the medium is said to be *isotropic*; if $\varepsilon_x = \varepsilon_y \neq \varepsilon_z$, the crystal is *uniaxial* and $\varepsilon_x \neq \varepsilon_y \neq \varepsilon_z$ corresponds to a *biaxial* crystal. Hyperbolic metamaterials represent a particular type of uniaxial crystals where either $\varepsilon_x = \varepsilon_y \equiv \varepsilon_\perp$ or $\varepsilon_z \equiv \varepsilon_\parallel$ is negative (i.e. $\varepsilon_\perp \varepsilon_\parallel < 0$), with the subscripts $\perp$ and $\parallel$ referring to perpendicular and parallel to the anisotropic axis z, respectively [31–33].

Anisotropic media allow the propagation with different velocities of two monochromatic plane waves with different linear polarizations. These are the *ordinary* wave, corresponding to the electric field $\mathbf{E}$ perpendicular to the optic axis z; and the *extraordinary* wave, with $\mathbf{E}$ parallel to the plane containing the wavevector $\mathbf{k}$ and the optic axis [123, 124]. It can be seen that this leads to two dispersion relations in uniaxial crystals, one for each type of wave, which can be readily derived from Maxwell's equations in free space [33, 123, 124]. For the ordinary wave, we obtain

$$k_x^2 + k_y^2 + k_z^2 = \frac{\omega^2}{c^2}\varepsilon_\perp, \tag{2.2}$$

with k_x, k_y, k_z being the components of the wavevector $\mathbf{k}$, ω is the frequency of the monochromatic wave and c is the speed of light in vacuum. Note that this expression represents a sphere in (k_x, k_y, k_z) space, which is the same result one would obtain for an isotropic material. For the extraordinary wave, the dispersion relation reads

$$\frac{k_x^2 + k_y^2}{\varepsilon_\parallel} + \frac{k_z^2}{\varepsilon_\perp} = \frac{\omega^2}{c^2}. \tag{2.3}$$

In dielectric uniaxial crystals with $\varepsilon_\parallel, \varepsilon_\perp > 0$, Eq. (2.3) describes an ellipsoid. However, when $\varepsilon_\perp \varepsilon_\parallel < 0$, it represents an hyperboloid (hence the name of "hyperbolic" metamaterials). Note that this hyperboloid will have two sheets if $\varepsilon_\perp > 0$, $\varepsilon_\parallel < 0$ (called "Type I") and one sheet if $\varepsilon_\perp < 0$, $\varepsilon_\parallel > 0$ (called "Type II") [31–33]. The isofrequency surfaces for the different cases are shown in Fig. 2.3.

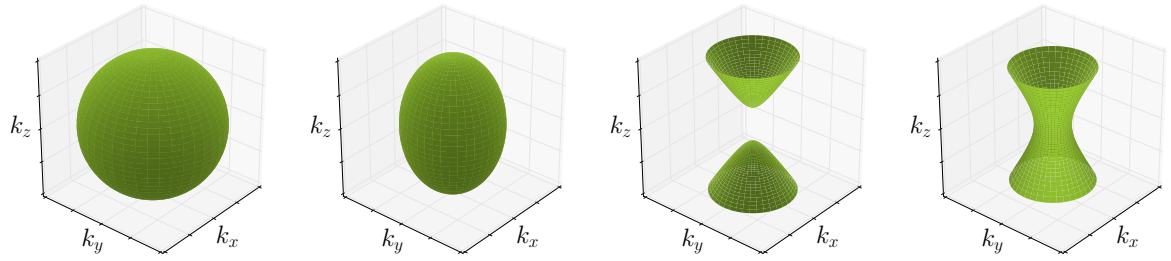

(a) Isotropic material. (b) Uniaxial dielectric. (c) Hyperbolic Type I. (d) Hyperbolic Type II.

Figure 2.3: Isofrequency surfaces given by $\omega(\mathbf{k}) =$ constant in (k_x, k_y, k_z) space for different media. Note that (a) could correspond as well to an ordinary wave in a uniaxial crystal while (b), (c) and (d) are only possible for extraordinary waves.

One of the most significant implications of the indefinite dispersion is the fact that, ideally, waves with infinitely large wavevectors could propagate and thus, there will not be evanescent modes [31, 32, 125]. (Nevertheless, a metamaterial is always limited to its operating bandwidth, determined by its internal structure.) Consequently, hyperbolic metamaterials have been studied for the design of superlenses for subwavelength imaging [27–30].

The wave equation for the electric field $\mathbf{E}$ in a non-magnetic anisotropic medium can be written as [123]

$$\boldsymbol{\nabla} \times \boldsymbol{\nabla} \times \mathbf{E} + \frac{\underline{\underline{\varepsilon}}}{c^2} \frac{\partial^2 \mathbf{E}}{\partial t^2} = 0. \tag{2.4}$$

If we consider a monochromatic extraordinary wave of frequency ω with only z component, $\mathbf{E} = E_z \mathrm{e}^{-\mathrm{i}\omega t}\hat{\mathbf{z}}$, Eq. (2.4) for a hyperbolic metamaterial Type I becomes [126]

$$\frac{1}{|\varepsilon_{\parallel}|}\left(\frac{\partial^2 E_z}{\partial x^2}+\frac{\partial^2 E_z}{\partial y^2}\right)-\frac{1}{\varepsilon_{\perp}}\frac{\partial^2 E_z}{\partial z^2}=\frac{\omega^2}{c^2}E_z. \tag{2.5}$$

Note that this expression also corresponds to a (2+1) Klein-Gordon equation for a massive field in which z behaves like a time-like variable [127]. Because of this, hyperbolic metamaterials have been proposed to model (2+1) spacetimes and study different phenomena such as cosmological inflation [128], the Rindler horizon [129] or the Milne universe [130].

2.4 Transformation optics

2.4.1 Geometry and media

Metamaterials have provided the ability to control light in unprecedented ways. Spatial distributions of the permittivity and permeability alter the electromagnetic field and can cause light to bend as if it was on another set of coordinates. Given that Maxwell's equations are form-invariant under coordinate transformations, the appropriate medium parameters corresponding to a certain geometrical transformation can be found. The mathematical technique that enables the design of such materials is called transformation optics [5–8]. This is the method behind the invisibility cloak that guides light around an object to make it seem invisible [24, 131].

The analogy between geometry and anisotropic media was already theoretically investigated by Gordon [9] and Tamm [10, 11] in the 1920s. Gordon pointed out that moving media can create an effective spacetime geometry for light, whereas Tamm studied the electromagnetic equations in anisotropic media and found them to be analogous to the propagation of light in gravitational fields. Years later, Skrotskii [12] wrote as well about this equivalence and applied it to the field generated by a spherical mass moving uniformly. Finally, in 1960, Plebanksi [13] formulated concise constitutive equations that related the propagation of light in medium with that in a gravitational field (some later studies dealt with this analogy as well [14–17]). However, it was not until the appearance of metamaterials that the realization of such media became possible and interest in the field reemerged [45, 131, 132]. This analogy has inspired the investigation of several general relativity phenomena from the point of view of metamaterial implementation: optical analogues of black holes [37–44], Schwarzschild spacetime [45–49], Kerr spacetime [50], cosmic strings [51–55], wormholes [56, 57], Hawking radiation [58, 59], etc.

To mark out the framework where the analogy between media and celestial mechanics is established, let us consider a spacetime metric in arbitrary coordinates

$$\mathrm{d}s^2 = g_{00}\,\mathrm{d}t^2 + 2g_{0i}\,\mathrm{d}t\,\mathrm{d}x^i + g_{ij}\,\mathrm{d}x^i\,\mathrm{d}x^j, \tag{2.6}$$

where g_{ij} is the spatial part of the metric tensor with $i,j = 1,2,3$ and the system of units in which the speed of light $c = 1$ is assumed. Then, it can be shown [17] that the covariant Maxwell's equations written in curved coordinates can be transformed into their standard form for flat space but in the presence of an effective medium. To do that, we begin by introducing the electromagnetic field tensor $F_{\mu\nu}$

$$F_{\mu\nu} = \begin{pmatrix} 0 & -E_x & -E_y & -E_z \\ E_x & 0 & B_z & -B_y \\ E_y & -B_z & 0 & B_x \\ E_z & B_y & -B_x & 0 \end{pmatrix}, \tag{2.7}$$

which includes the components of the electromagnetic fields $\mathbf{E}$ and $\mathbf{B}$. Note that we use Greek indices to denote time and space components, $\mu, \nu = 0, 1, 2, 3$ and Latin letters for the spatial components only. Then, Maxwell's equations in arbitrary curvilinear coordinates can be written as [133]

$$\partial_{[\lambda} F_{\mu\nu]} = 0, \quad \frac{1}{\sqrt{-g}} \partial_\nu (\sqrt{-g} F^{\mu\nu}) = j^\mu, \tag{2.8}$$

where g is the determinant of the spacetime metric $g_{\mu\nu}$, j^μ is the four-current and the square brackets denote antisymmetrization. Inspecting these equations, the fields $\mathbf{E}$, $\mathbf{D}$, $\mathbf{H}$ and $\mathbf{B}$ can be expressed in terms of the electromagnetic tensor as [13]

$$E_i = F_{i0}, \quad D^i = \sqrt{-g} F^{0i}, \quad H_i = \frac{1}{2} \epsilon_{ijk} \sqrt{-g} F^{jk}, \quad B^i = \frac{1}{2} \epsilon^{ijk} F_{jk}, \tag{2.9}$$

with ϵ_{ijk} being the Levi-Civita symbol. However, the fields are not independent and can be related through the equations [13, 17]

$$F_{0i} = g_{0\mu} g_{i\nu} F^{\mu\nu}, \quad F^{ij} = g^{i\mu} g^{j\nu} F_{\mu\nu}. \tag{2.10}$$

By substituting Eqs. (2.9) in Eqs. (2.10), the constitutive relations of the equivalent medium are obtained in the form [13]:

$$D^i = \varepsilon^{ij} E_j - (\mathbf{\Gamma} \times \mathbf{H})^i, \quad B^i = \mu^{ij} H_j + (\mathbf{\Gamma} \times \mathbf{E})^i, \tag{2.11}$$

with the permittivity and permeability tensors given in Cartesian coordinates by

$$\varepsilon^{ij} = \mu^{ij} = -\frac{\sqrt{-g}}{g_{00}} g^{ij}, \tag{2.12}$$

and a vector $\mathbf{\Gamma}$ that couples the electric and magnetic fields given by

$$\Gamma_i = -\frac{g_{0i}}{g_{00}}. \tag{2.13}$$

In this way, the information about the gravitational field is mapped into the parameters of the material. The medium prescribed by Eqs. (2.11) has sometimes been referred to by authors as "bianisotropic" [8, 20, 21, 134]. In Cartesian coordinates, the vector $\mathbf{\Gamma}$ has the dimension of a velocity and it is closely related to the velocity of the medium [132]. Indeed, the simplest example of a magneto-electric coupling in a material is a moving medium because, even if the dielectric responds to the electromagnetic field in its local frame, it is moving and Lorentz transformations mix electric and magnetic fields [109, 131, 132]. However, given that in the cases considered in the following chapters the space and time components of the metric are decoupled, $g_{0i} = 0$, the magneto-electric coupling vector vanishes, $\mathbf{\Gamma} = 0$, and the constitutive equations take the simpler form of a regular anisotropic material

$$D^i = \varepsilon^{ij} E_j, \quad B^i = \mu^{ij} H_j, \tag{2.14}$$

with ε^{ij} and μ^{ij} given by Eq. (2.12).

Nevertheless, it has been pointed out that this transformation is not uniquely defined and that different choice of coordinates can lead to different analogue materials [45, 62]. However, this freedom allows to choose the most appropriate transformation for every situation. In Ch. 3 we see how two equivalent sets of coordinates lead to different medium parameters, with one having a simpler form than the other. In this way, we can choose the one that may be easier to implement in a laboratory experiment.

2.4.2 Electromagnetic fields in anisotropic media

Due to the anisotropy of the medium, the electric displacement field $\mathbf{D}$ is not in the direction of $\mathbf{E}$, and the magnetic induction field $\mathbf{B}$ is not in the direction of $\mathbf{H}$. To simplify the treatment of this problem, we consider the propagation of light in the equatorial plane, $z = 0$. In the case of the metrics studied in the following chapters, this will allow to eliminate one of the anisotropies (electric or magnetic).

Consider an electromagnetic wave with transverse electric (TE) polarization, that is, the electric field $\mathbf{E}$ is perpendicular to the x–y plane, $\mathbf{E} = E_z\hat{\mathbf{z}}$; and a material with $\varepsilon^{xz} = \varepsilon^{yz} = 0$ (it will be shown in future chapters that this is satisfied for both the black hole spacetime at $z = 0$ and the cosmic string metric). Because of that, the directions of $\mathbf{D}$ and $\mathbf{E}$ coincide, making ε^{zz} the only relevant matrix element since it connects the electric components of the field: $\mathbf{D} = \varepsilon^{zz}\mathbf{E}$. Thus, the electric anisotropy of the medium becomes irrelevant. As for the magnetic components, seeing how the permittivity and permeability tensors are equal [see Eq. (2.12)], $\mu^{xz} = \mu^{yz} = 0$. Consequently, we obtain: $B^z = H^z = 0$, $B^x = \mu^{xx}H_x + \mu^{xy}H_y$ and $B^y = \mu^{xy}H_x + \mu^{yy}H_y$. We can see that $\mathbf{B}$ and $\mathbf{H}$ are confined to the x–y plane and their directions do not coincide. We will refer to this as a "magnetically anisotropic medium". A similar argument can be made for the transverse magnetic (TM) polarization, for which $\mathbf{H}$ is perpendicular to the x–y plane: $\mathbf{H} = H_z\hat{\mathbf{z}}$. In this case, the magnetic anisotropy is the one becoming irrelevant: the directions of the magnetic vectors coincide, $\mathbf{B} = \mu^{zz}\mathbf{H}$, and the electric field is confined to the x–y plane, $D^x = \varepsilon^{xx}E_x + \varepsilon^{xy}E_y$ and $D^y = \varepsilon^{xy}E_x + \varepsilon^{yy}E_y$. We call this "electrically anisotropic medium". These two cases are summarized in Fig. 2.4 [47].

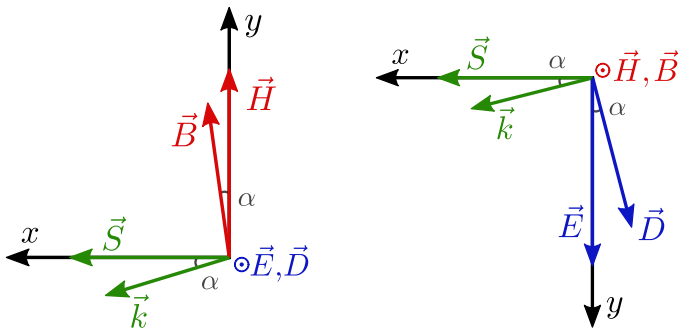

(a) Magnetic anisotropy. (b) Electric anisotropy.

Figure 2.4: Electromagnetic fields $\mathbf{H}$, $\mathbf{B}$, $\mathbf{E}$, $\mathbf{D}$, wavevector $\mathbf{k}$ and Poynting vector $\mathbf{S}$ for: (a) TE polarization in a magnetically anisotropic medium, and (b) TM polarization in an electrically anisotropic medium.

The medium anisotropy has very important physical consequences on the propagation of the electromagnetic waves. If we take a monochromatic plane wave with wavevector $\mathbf{k}$ and consider Maxwell's equations in a source-free form,

$$\boldsymbol{\nabla}\cdot\mathbf{B} = 0, \quad \boldsymbol{\nabla}\cdot\mathbf{D} = 0, \quad \boldsymbol{\nabla}\times\mathbf{E} = -\frac{\partial\mathbf{B}}{\partial t}, \quad \boldsymbol{\nabla}\times\mathbf{H} = \frac{\partial\mathbf{D}}{\partial t}. \tag{2.15}$$

then it can be shown that $\mathbf{D}$, $\mathbf{B}$ and $\mathbf{k}$ form an orthogonal vector triplet. On the other hand, the Poynting vector $\mathbf{S} \sim \mathbf{E}\times\mathbf{H}$, by definition, forms another orthogonal vector triplet with $\mathbf{E}$ and $\mathbf{H}$. Therefore, energy does not propagate in the direction of the wavevector, that is, the ray velocity and the phase velocity are not equal, unlike what happens for an isotropic medium [123]. It can be seen that the angle between $\mathbf{S}$ and $\mathbf{k}$ (denoted by α in Fig. 2.4) is equal to that between $\mathbf{B}$ and $\mathbf{H}$ in the TE polarization or between $\mathbf{D}$ and $\mathbf{E}$ in the TM polarization. This angle α can be

found as:

$$\tan\alpha = -\frac{\mu^{xy}}{\mu^{yy}} = -\frac{\varepsilon^{xy}}{\varepsilon^{yy}}. \tag{2.16}$$

Wave propagation in the equivalent medium (2.12) is described by Maxwell's equations (2.15) supplemented by the constitutive relations (2.14). If the operating frequency bandwidth is sufficiently narrow, the dispersion can be neglected and one can consider a monochromatic wave with frequency ω. Equations (2.15) can then be reduced [124] to the wave equation for a time-harmonic electric field vector $\mathbf{E}_\omega$

$$\boldsymbol{\nabla} \times \left[\underline{\underline{\mu}}^{-1}(\boldsymbol{\nabla} \times \mathbf{E}_\omega)\right] = \omega^2 \underline{\underline{\varepsilon}}\, \mathbf{E}_\omega, \tag{2.17}$$

where $\underline{\underline{\varepsilon}}$ and $\underline{\underline{\mu}}^{-1}$ denote the permittivity and inverse permeability tensors, respectively. The electromagnetic propagation in the equatorial plane, $z = 0$, can be described in terms of either TE or TM waves. For the TE wave, $\mathbf{E}_\omega(x, y) = E(x, y)\hat{\mathbf{z}}$, we obtain the equation for the z-component of the electric field E in the two-dimensional (x, y) space

$$\frac{\partial}{\partial x}\left(\mu_{xy}\frac{\partial E}{\partial y} - \mu_{yy}\frac{\partial E}{\partial x}\right) - \frac{\partial}{\partial y}\left(\mu_{xx}\frac{\partial E}{\partial y} - \mu_{xy}\frac{\partial E}{\partial x}\right) = \omega^2 \varepsilon^{zz} E, \tag{2.18}$$

where $\mu_{xx}, \mu_{xy}, \mu_{yy}$ are the corresponding components of the inverse permeability tensor $\underline{\underline{\mu}}^{-1}$ and ε^{zz} corresponds to the permittivity $\underline{\underline{\varepsilon}}$. Since only one component of $\underline{\underline{\varepsilon}}$ has entered into the final equation (2.18), the permittivity can be chosen isotropic with all its diagonal elements equal to ε^{zz} and the off-diagonal terms equal to zero. In this case, the equivalent medium will be magnetically anisotropic [see Fig. 2.4(a)].

The wave equation for the TM case can also be easily obtained from the above formulas by means of the substitutions: $\varepsilon^{ij} \rightleftarrows \mu^{ij}$, $E \to H$. In such a case, the medium is electrically anisotropic [Fig. 2.4(b)], and one should solve the equation for the magnetic field $H(x, y)$.

2.5 Summary

The main ideas exposed in this chapter can be summarized as follows:

- Metamaterials are artificial composite materials whose building blocks are substantially smaller than the wavelength of the incident radiation. Their properties arise from their internal structure rather than from the constitutive materials. Given that they exhibit exotic behaviour, they are used for a wide variety of applications.
- Certain general relativity phenomena can be modelled with metamaterials in the context of analogue gravity.
- Hyperbolic metamaterials are strongly anisotropic and exhibit indefinite dispersion. The wave equation in these media has the form of a (2+1) Klein Gordon equation, where one of the spatial coordinates behaves as a time-like variable. As a consequence, hyperbolic metamaterials can be used to model (2+1) spacetimes.
- By means of transformation optics, it can be shown that light propagation in a curved spacetime is formally equivalent to that in a bianisotropic medium. In this way, the permittivity and permeability of the analogous material are determined for future implementation in a metamaterial so experiments can be carried out.

- In general, the equivalent medium will be anisotropic (i.e. the permittivity and permeability are given by a tensor). However, we find that for the two geometries studied in this thesis (that is, a system with spherical symmetry and a conical topological defect) only one of the anisotropies – either electric or magnetic – is relevant when considering a TE- or TM-polarized wave propagating in the $z = 0$ plane (see Fig. 2.4). This will be justified in more detail in Secs. 3.2.1 and 4.2.1. Moreover, the equations for the TE and TM cases are completely equivalent.

CHAPTER 3

Schwarzschild black hole

3.1 Introduction

Einstein's theory of general relativity changed the way we think about gravity, space and time. His field equations of 1915 [60] relate mass and energy with the curvature of *spacetime*. In this way, it was established that gravitational phenomena do not arise from instant forces and fields, but from four-dimensional geometry.

One of the most important predictions of general relativity is that light also feels the spacetime curvature and, therefore, its trajectory can be affected by heavy objects. (This contrasted with the Newtonian idea that only massive bodies are subject to the gravitational force.) This effect was famously verified for the first time in 1919 by Eddington and his collaborators [135], who measured the apparent change in position of stars as their light passed near the Sun during an eclipse.

General relativity also has astrophysical implications: it predicts the existence of *black holes*. They are created when a massive body collapses into a volume small enough that the gravitational pull at the surface is too strong for anything to escape from it, not even light. The surface of the black hole is called "event horizon" and, in classical physics, nothing can emerge from it [124, 133, 136].

Not long after the publication of the Einstein field equations, in 1916, Schwarzschild [61] found a non-trivial solution to them that determined the gravitational field in vacuum produced by any spherically symmetric mass distribution. Its line element in spherical coordinates (r, φ, θ) reads:

$$\mathrm{d}s^2 = -\left(1 - \frac{\mathrm{r_s}}{r}\right)\mathrm{d}t^2 + \frac{\mathrm{d}r^2}{1 - \frac{\mathrm{r_s}}{r}} + r^2(\sin^2\theta\,\mathrm{d}\varphi^2 + \mathrm{d}\theta^2). \tag{3.1}$$

Here, the speed of light $c = 1$, the Schwarzschild radius $\mathrm{r_s} = 2GM$, G is the universal gravitational constant and M is the mass of the source of gravitation. In particular, this metric is said to represent a black hole since it presents an event horizon at $r = \mathrm{r_s}$ [124, 133, 136]. In this chapter we study how to characterize a metamaterial mimicking a static spherically symmetric spacetime, such as the Schwarzschild black hole, making use of the transformation optics equations introduced in Sec. 2.4. We obtain full-wave simulations in the medium and then they are compared with the null-geodesics in this spacetime.

3.2 Medium parameters

3.2.1 Static spherically symmetric spacetime

We note that the Schwarzschild metric (3.1) has certain symmetries, therefore we will begin by considering the more general case of a static spherically symmetric spacetime. The metric (2.6) in (t, r, θ, φ) coordinates can then be written in a generic form as [103]

$$\mathrm{d}s^2 = g_{00}(r)\,\mathrm{d}t^2 + g_{rr}(r)\left\{\mathrm{d}r^2 + f(r)\left[r^2\,\mathrm{d}\theta^2 + r^2\sin^2\theta\,\mathrm{d}\varphi^2\right]\right\}, \tag{3.2}$$

where $f(r)$ is an *anisotropic factor*. Note that the metric (3.2) obeys the rotational symmetries in the three-dimensional (r, θ, φ) space.

To obtain the medium parameters in the Cartesian coordinate system, the metric (3.2) needs to be projected into a flat background. After performing a coordinate transformation and substituting in Eq. (2.12), we get the permittivity and permeability tensors in the form [47]:

$$\varepsilon^{ij} = \mu^{ij} = \sqrt{-\frac{g_{rr}}{g_{00}}}\left[\delta^{ij} - (1-f)\frac{x^i x^j}{r^2}\right], \tag{3.3}$$

where δ^{ij} is the Kronecker delta, $r = \sqrt{x^2+y^2+z^2}$, and the Cartesian coordinates are denoted by $(x^1, x^2, x^3) \equiv (x, y, z)$. Note that, as stated in Sec. 2.4.2, $\varepsilon^{xz} = \varepsilon^{yz} = \mu^{xz} = \mu^{yz} = 0$ in the equatorial plane $z = 0$, which allows to eliminate one of the anisotropies by using TE- or TM-polarized waves. It is also seen that whenever $f \neq 1$, the permittivity and permeability tensors contain off-diagonal elements and the equivalent medium is essentially anisotropic, with the angle α between the ray and phase velocity being

$$\tan\alpha = \frac{(1-f)xy}{x^2 + fy^2}. \tag{3.4}$$

Only when $f = 1$, the off-diagonal elements vanish and the medium becomes completely isotropic with all the diagonal elements equal to the refractive index: $n(r) = \sqrt{-g_{rr}/g_{00}}$. In general relativity, the spacetime with $f = 1$ in Eq. (3.2) is said to be conformal to flat space. (A transformation is considered to be *conformal* if it preserves the angles, but not necessarily the lengths [137].) Every static spherically symmetric spacetime with $f \neq 1$ can be converted to conformally flat form by an appropriate transformation of the radial coordinate: $r \to \rho$ [103]. The new radial coordinate is obtained by

$$\rho = r\exp\left\{\int_r^\infty \left[1 - \frac{1}{\sqrt{f(r')}}\right]\frac{\mathrm{d}r'}{r'}\right\}, \tag{3.5}$$

where the isotropic boundary condition at infinity, $f(\infty) = 1$, is taken into account. The line element in the $(t, \rho, \theta, \varphi)$ *isotropic* coordinates takes the conformally flat form:

$$\mathrm{d}s^2 = g_{00}[r(\rho)]\,\mathrm{d}t^2 + \Lambda(\rho)\left(\mathrm{d}\rho^2 + \rho^2\sin^2\theta\,\mathrm{d}\varphi^2 + \rho^2\mathrm{d}\theta^2\right), \tag{3.6}$$

where the time dilation term g_{00} and the conformal factor $\Lambda = g_{rr}fr^2/\rho^2$ are calculated by means of the function $r(\rho)$ which should be obtained by inverting (3.5). Thus, the permittivity and permeability tensors are simply reduced to the isotropic refractive index (see also [15]):

$$\varepsilon^{ij} = \mu^{ij} = \delta^{ij}\sqrt{-\frac{\Lambda}{g_{00}}} \equiv \delta^{ij}\,n(\rho). \tag{3.7}$$

Note that the medium determined by (3.7) is isotropic (and therefore the phase and ray velocities are parallel) but it is still inhomogeneous since the refractive index varies with the radial coordinate ρ. Due to the isotropy, we believe this design would be much easier to implement in a metamaterial.

3.2.2 Schwarzschild spacetime

We can now apply the results for the static spherically symmetric spacetime to the Schwarzschild metric. Comparing Eq. (3.1) with Eq. (3.2), one can easily identify: $g_{00} = -(1 - \mathrm{r_s}/r)$, $g_{rr} = -1/g_{00}$, and $1 - f = \mathrm{r_s}/r$. Since the Schwarzschild metric (3.1) is not in a conformally flat form, one obtains the anisotropic equivalent medium tensors

$$\varepsilon^{ij} = \mu^{ij} = \frac{1}{1 - \frac{\mathrm{r_s}}{r}} \left(\delta^{ij} - \frac{x^i x^j}{r^3} \mathrm{r_s} \right), \tag{3.8}$$

(also given in matrix form in Ref. [46]) and from Eq. (3.4) we find the angle between the ray and phase velocities:

$$\tan \alpha = \frac{xy\mathrm{r_s}}{r^3 - y^2 \mathrm{r_s}}. \tag{3.9}$$

As seen in the previous section, a spherically symmetric spacetime can be written in a conformally flat form. In the case of the Schwarzschild metric, this is done by means of the substitution (see, e.g. [103, 133])

$$r = \rho \left(1 + \frac{\mathrm{r_s}}{4\rho} \right)^2. \tag{3.10}$$

Then, the inverted formula for the isotropic radial coordinate ρ is

$$\rho = \frac{1}{2} \left(r - \frac{1}{2}\mathrm{r_s} + \sqrt{r^2 - \mathrm{r_s} r} \right), \tag{3.11}$$

which can also be obtained from Eq. (3.5) by substituting $f = 1 - \mathrm{r_s}/r$. The coordinate transformation $r \to \rho$ is plotted in Fig. 3.1. We can see that the event horizon will now be located at $\rho = \mathrm{r_s}/4$, which separates two distinctive regions. For $\mathrm{r_s}/4 < \rho < \infty$, the radial coordinate r increases at the same rate as ρ. On the other hand, the region $0 < \rho < \mathrm{r_s}/4$ is mapped to the exterior of the Schwarzschild black hole too, $\mathrm{r_s} < r < \infty$.

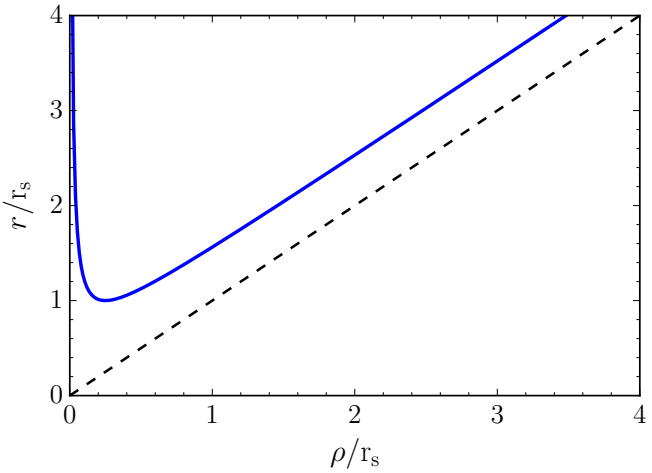

Figure 3.1: Transformation from the radial coordinate r to the isotropic ρ given by Eq. (3.10). Dashed line corresponds to the identity, $r = \rho$.

In the new isotropic coordinates $(t, \rho, \varphi, \theta)$, the Schwarzschild metric becomes

$$\mathrm{d}s^2 = -\left(\frac{1 - \frac{\mathrm{r_s}}{4\rho}}{1 + \frac{\mathrm{r_s}}{4\rho}} \right)^2 \mathrm{d}t^2 + \left(1 + \frac{\mathrm{r_s}}{4\rho} \right)^4 (\mathrm{d}\rho^2 + \rho^2 \sin^2\theta \, \mathrm{d}\varphi^2 + \rho^2 \mathrm{d}\theta^2). \tag{3.12}$$

Finally, the refractive index of the equivalent medium is found from Eq. (3.7) as (see also [14]):

$$n(\rho) = \frac{\left(1+\frac{\mathrm{r_s}}{4\rho}\right)^3}{1-\frac{\mathrm{r_s}}{4\rho}}. \tag{3.13}$$

In Sec. 3.5 we will model both media – anisotropic (3.8) and isotropic (3.13) – and perform full-wave numerical simulations.

3.3 Hamiltonian formulation

In the limit of geometrical optics, for which the wavelength is much smaller than the scale of variation of the medium parameters, electromagnetic waves should follow ray trajectories (null-geodesics of the background spacetime). To test the validity of our model, it would be interesting to compare the full-wave numerical simulation of the propagation of light in the metamaterial with its geometrical optics limit, for which analytical solutions exist. To do this, we will use Hamiltonian mechanics.

Let us start with the wave equation (2.17), which we apply again to the equatorial plane $z = 0$, and consider a TE-polarized wave. To keep our analysis as general as possible, we consider the static spherically symmetric spacetime (3.2). Given that the medium tensors (3.3) are diagonal in the spherical coordinate system (r, φ, θ),

$$\varepsilon^{ij} = \mu^{ij} = \sqrt{-\frac{g_{rr}}{g_{00}}}\,\mathrm{diag}(f, 1, 1), \tag{3.14}$$

it is advantageous to rewrite Eq. (2.18) in polar coordinates: $E(x, y) \to E(r, \varphi)$. One gets

$$\frac{1}{r}\frac{\partial}{\partial r}\left(\frac{r}{\mu_\varphi}\frac{\partial E}{\partial r}\right) + \frac{1}{r^2}\frac{\partial}{\partial \varphi}\left(\frac{1}{\mu_r}\frac{\partial E}{\partial \varphi}\right) + \omega^2 \varepsilon_z E = 0, \tag{3.15}$$

where we denote $\mu_r \equiv \mu^{rr}$, $\mu_\varphi \equiv \mu^{\varphi\varphi}$ and $\varepsilon_z \equiv \varepsilon^{zz}$, which are the medium parameters in polar coordinates[2].

In the *eikonal approximation* we seek a solution in the form: $E(r, \varphi) = E_0 \exp[\mathrm{i}\mathcal{S}(r, \varphi)]$, where E_0 is the slowly varying amplitude and $\mathcal{S}(r, \varphi)$ is the fast varying eikonal [123, 138]. Substituting into Eq. (3.15) and neglecting the small terms (corresponding to the derivatives of slowly varying functions), we obtain:

$$\frac{1}{\mu_\varphi}\left(\frac{\partial \mathcal{S}}{\partial r}\right)^2 + \frac{1}{\mu_r r^2}\left(\frac{\partial \mathcal{S}}{\partial \varphi}\right)^2 - \varepsilon_z\,\omega^2 = 0, \tag{3.16}$$

which can be rewritten in terms of the spacetime metric coefficients by means of Eq. (3.14) as

$$\frac{1}{g_{rr}}\left[\left(\frac{\partial \mathcal{S}}{\partial r}\right)^2 + \frac{1}{f r^2}\left(\frac{\partial \mathcal{S}}{\partial \varphi}\right)^2\right] + \frac{1}{g_{00}}\,\omega^2 = 0. \tag{3.17}$$

But this is nothing else than the eikonal equation for a light ray in a gravitational field [138]

$$g^{\alpha\beta}\frac{\partial \mathcal{S}}{\partial x^\alpha}\frac{\partial \mathcal{S}}{\partial x^\beta} = 0, \tag{3.18}$$

[2] Given that we are considering the equatorial plane $z = 0$, $\varepsilon_\theta = \varepsilon_z$.

with the indices α, β running over time and space coordinates. The Hamiltonian representation of Eq. (3.18) is obtained by rewriting it in terms of the variables $p_\alpha = \partial\mathcal{S}/\partial x^\alpha$, where p_α is the 4-momentum[3]. That is,

$$2\mathcal{H} = g^{\alpha\beta} p_\alpha p_\beta = p^\beta p_\beta = 0. \tag{3.19}$$

Thus, using the definitions $p_r = \partial\mathcal{S}/\partial r$, $p_\varphi = \partial\mathcal{S}/\partial\varphi$, and $p_t = \omega$ and substituting in Eq. (3.17), we obtain

$$2\mathcal{H} = \frac{1}{g_{00}}\, p_t^2 + \frac{1}{g_{rr}}\left(p_r^2 + \frac{1}{fr^2}\, p_\varphi^2\right). \tag{3.20}$$

The optic Hamiltonian $\mathcal{H}$ given by Eq. (3.20) describes the ray trajectories in the analogue anisotropic medium and is precisely the one used to determine the null-geodesics in a gravitational field. It takes into account the time dilation by means of the term g_{00}, the spatial curvature by the metric coefficient g_{rr} and the medium anisotropy through the function f. The latter should result in the deviation of an angle α of the phase gradient from the ray propagation direction.

The Schwarzschild Hamiltonian can be readily obtained by the corresponding substitutions in Eq. (3.20)

$$2\mathcal{H} = -\frac{1}{1 - \frac{\mathrm{r_s}}{r}}\, p_t^2 + \left(1 - \frac{\mathrm{r_s}}{r}\right) p_r^2 + \frac{1}{r^2}\, p_\varphi^2. \tag{3.21}$$

On the other hand, in isotropic coordinates (3.12), the Hamiltonian becomes

$$2\mathcal{H} = -\left(\frac{1 + \frac{\mathrm{r_s}}{4\rho}}{1 - \frac{\mathrm{r_s}}{4\rho}}\right)^2 p_t^2 + \frac{1}{\left(1 + \frac{\mathrm{r_s}}{4\rho}\right)^4}\left(p_\rho^2 + \frac{1}{\rho^2}\, p_\varphi^2\right). \tag{3.22}$$

Note that Eq. (3.19), when applied to the optical medium, gives the generalized dispersion relation [132] also known as the Fresnel equation [123, 124]. The discussion of this relation for the Schwarzschild equivalent medium can be found, for instance, in Ref. [45].

By comparing the terms in Eqs. (3.16) and (3.17), one can see that for the TE wave, the time dilation term g_{00} is determined by the dielectric permittivity of the equivalent medium, while the spatial metric components g_{rr} and f is related to the magnetic permeability. In other words, the time and space metric coefficients correspond to different properties of the medium: either electric or magnetic. Similarly, if we consider the TM wave, one should replace: $\varepsilon^{ij} \rightleftarrows \mu^{ij}$; $E \to H$ (see Sec. 2.4.2), and the correspondence will be just the opposite: g_{00} will be related to μ_z, while g_{rr} and f will correspond to ε_r and ε_φ.

Equation (3.16) can be divided by ε_z and the medium parameters can be redefined according to: $\tilde{\mu}_\varphi = \mu_\varphi\varepsilon_z$, $\tilde{\mu}_r = \mu_r\varepsilon_z$ and $\tilde{\varepsilon} = 1$. It is easy to check that the new medium gives exactly the same ray trajectories, although it has the scalar permittivity $\tilde{\varepsilon}$ of free space and the inhomogeneous permeability $\underline{\underline{\tilde{\mu}}}$. Actually, the Hamiltonian $\mathcal{H}$ may be multiplied by any arbitrary function of the coordinates (by g_{00}, in this case) without changing the ray paths obtained from the equations of motion since only the parametrization of the affine parameter changes. This means that in the geometrical optics limit, one can introduce a set of equivalent media, all giving the same trajectories for light. Nevertheless, the wave equation (3.15) cannot be renormalized in this way, and therefore the interference patterns in those analogous media will be different (see App. A for the numerical results in the medium with the renormalized parameters).

[3]The definition of the momentum of the photon has been subject to debate for over a century, the problem known as the "Abraham–Minkowski dilemma" [139]. The Abraham or kinetic momentum is a vector p^i in the direction of ray propagation, whereas the Minkowski or canonical momentum is a one-form p_i proportional to the phase gradient [132]. Only in isotropic media the two point to the same direction. In the Hamiltonian formulation we use, the one-form p_α naturally appears, therefore we will refer to it as the momentum for simplicity.

3.4 Null-geodesics in Schwarzschild spacetime

In order to understand how light behaves in the exterior of a Schawrzschild black hole, we should study the null-geodesics, that is, the path that a massless particle follows. As stated in Eq. (3.19), in the Hamiltonian formulation this corresponds to setting $\mathcal{H} = 0$. With that in mind, the ray dynamics can easily be calculated from Hamilton's equations of motion:

$$\dot{q}^\alpha = \frac{\partial \mathcal{H}}{\partial p_\alpha}, \quad \dot{p}_\alpha = -\frac{\partial \mathcal{H}}{\partial q^\alpha}, \tag{3.23}$$

where the canonical coordinates in our case are: $q^\alpha = (t, r, \varphi)$, $p_\alpha = (p_t, p_r, p_\varphi)$ and the dot denotes the derivative over an affine parameter which varies along the trajectory. Note that, for the static spherically symmetric spacetime (3.2), the coefficients g_{00}, g_{rr} and f are functions of only the radial coordinate. Therefore, there exist two integrals of motion, $\dot{p}_t = 0$ and $\dot{p}_\varphi = 0$, which just state the conservation of energy and angular momentum for the static spherically symmetric system, respectively. In principle, these two constants of motion can be introduced; but in fact, since photons are massless, the ray trajectories are determined by only one constant – the impact parameter b, which is the ratio between them [136].

We can determine the ray trajectories in the Schwarzschild spacetime (3.1) by means of Eqs. (3.23):

$$\dot{t} = -\frac{p_t}{1 - \frac{\mathrm{r_s}}{r}}, \quad \dot{r} = \left(1 - \frac{\mathrm{r_s}}{r}\right) p_r, \quad \dot{\varphi} = \frac{p_\varphi}{r^2}. \tag{3.24}$$

Combining them with the Hamiltonian (3.21) and introducing the energy $e \equiv p_t$ and the angular momentum $l \equiv p_\varphi$ of the photon at infinity, we obtain

$$\dot{r}^2 = e^2 - \frac{l^2}{r^2}\left(1 - \frac{\mathrm{r_s}}{r}\right), \tag{3.25}$$

which can be interpreted as an energy integral where we can introduce the effective potential [136]

$$V^2(r) = \frac{l^2}{r^2}\left(1 - \frac{\mathrm{r_s}}{r}\right). \tag{3.26}$$

By studying this potential we can find the different types of possible photon trajectories in this spacetime. If we divide Eq. (3.25) by $\dot{\varphi}$ to obtain the orbital equation and introduce the impact parameter $b \equiv l/e$,

$$\left(\frac{\mathrm{d}r}{\mathrm{d}\varphi}\right)^2 = \frac{r^4}{b^2} - r^2\left(1 - \frac{\mathrm{r_s}}{r}\right) \tag{3.27}$$

we see that the null-geodesics only depend on the parameter b.

In Fig. 3.2, we plot the effective potential $V(r)$ as a function of r. As suggested by Eq. (3.25), we can compare it with the energy e to classify the trajectories. In the units of Fig. 3.2(a), that corresponds to $\mathrm{r_s}/b$ (as expected, b is the only relevant parameter). We see that the potential has a maximum at $r = 3\mathrm{r_s}/2$ for a critical impact parameter $b_\mathrm{c} = 3\sqrt{3}\mathrm{r_s}/2$. This will be an unstable circular orbit, the *photonic sphere*. There are two other possible scenarios: for $b < b_\mathrm{c}$, the photon will be captured by the black hole, and for $b > b_\mathrm{c}$, the ray will be deflected. These are summarized in Fig. 3.2(b).

It should be remarked that the impact parameter b is independent of the chosen set of coordinates, since it is defined as a ratio between the angular momentum and energy of the photon measured at infinity. Therefore, the same classification of trajectories in relation to b_c should be made for isotropic coordinates. However, in this case, the photonic sphere will be of radius $\rho = (2+\sqrt{3})\mathrm{r_s}/4$

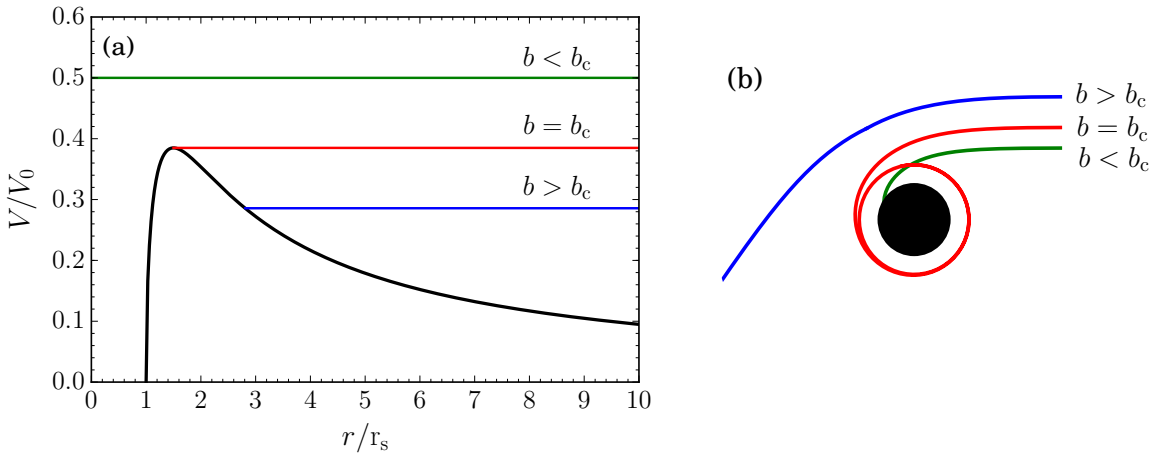

Figure 3.2: (a) Effective potential $V(r)$ in units of $V_0 = l/\mathrm{r_s}$ compared to the energy for different impact parameters b [see Eq. (3.25)]. The corresponding null-geodesics are shown in (b). They are representative of each type of trajectory: capture (green), unstable circular orbit (red) and deflection (blue).

and, as seen in Fig. 3.1, the event horizon will be at $\rho = \mathrm{r_s}/4$. For completeness, we give the equations of motion in isotropic coordinates,

$$\dot{t} = -\frac{\left(1+\frac{\mathrm{r_s}}{4\rho}\right)^2}{\left(1-\frac{\mathrm{r_s}}{4\rho}\right)^2} p_t, \quad \dot{\rho} = \frac{p_\rho}{\left(1+\frac{\mathrm{r_s}}{4\rho}\right)^4}, \quad \dot{\varphi} = \frac{p_\varphi}{\rho^2\left(1+\frac{\mathrm{r_s}}{4\rho}\right)^4}, \tag{3.28}$$

calculated from Eqs. (3.23), which should be supplemented by setting $\mathcal{H} = 0$ in the Hamiltonian (3.22).

In the following section, we will compare the different kinds of trajectories with the full-wave numerical simulations for both cases – isotropic and anisotropic.

3.5 Comparison of wave propagation with ray dynamics

We solve Eq. (2.18) in a rectangular 2D geometry of (x, y) space for a TE-polarized wave injected from the right boundary (see Fig. 3.3). The medium parameters we use are given by Eq. (3.8) for the anisotropic material and by Eq. (3.13) for the isotropic case. The computational domain is surrounded by a perfectly matched layer (PML) that absorbs the outward waves to ensure that there are no unwanted reflections. The simulations were carried out by the COMSOL Multiphysics software package and the data was processed in Python.

The black hole metric has a coordinate singularity at the event horizon, which translates into singular medium parameters. To avoid it, we set an effective horizon at $\mathrm{r_s} + \delta$ with δ being small positive number[4] and impose an absorbing inner core for $r < \mathrm{r_s} + \delta$ [38, 46]. For the simulations in isotropic coordinates, this will be changed accordingly to $\mathrm{r_s}/4 + \delta$.

[4] We set $\delta = 0.05\,\mathrm{r_s}$ (anisotropic case) and $\delta = 0.11\,\mathrm{r_s}$ (isotropic) in the calculations. We have checked that the variation of δ, whenever it is small enough, does not affect the global distribution of fields in the whole domain except some tiny shell at the horizon.

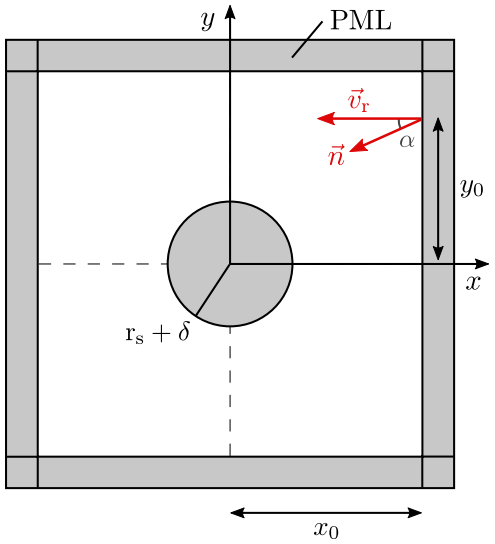

Figure 3.3: Diagram of the geometry for the numerical simulation of wave propagation in a metamaterial mimicking Schwarzschild spacetime. The ray velocity $\mathbf{v}_r$ and wave normal vector $\mathbf{n}$ are depicted at the injection point (x_0, y_0) and form an angle α. An absorbing core of radius $r_s + \delta$ is at the center of the domain (for isotropic coordinates this will be $r_s/4 + \delta$), which is all surrounded by a PML.

We use a Gaussian shape for the TE wave injected at (x_0, y_0) on the right boundary. For our geometry, that would mean imposing that the electric field E be [140]

$$E = \exp\left[-\left(\frac{y - y_0}{w_0}\right)^2\right], \tag{3.29}$$

on the boundary; with w_0 being the *waist radius*, i.e. the characteristic width of the beam. If the medium is anisotropic, one should remember that the beam does not propagate in the direction of the wave normal, as we discussed in Sec. 2.4.2. To ensure that the wave is always injected in a controlled way (in our case that is along the x-axis), we impose: $\mathbf{n} = -(\cos\alpha)\hat{\mathbf{x}} - (\sin\alpha)\hat{\mathbf{y}}$ for the normal unit vector $\mathbf{n}$ of the wave front. The angle α is determined by Eq. (3.4) applied to the point of injection (x_0, y_0). The fields correspond to those depicted in Fig. 2.4(a). In particular, the electric field vector is perpendicular to the plane of simulation and the medium has a magnetic anisotropy. Figure 2.4(b) corresponds to the case of TM wave injection into an electrically anisotropic medium, which could also be simulated. Because the injected wave is not a plane wave, the wavevector $\mathbf{k}$ in Fig. 2.4 should be replaced by the wave normal vector $\mathbf{n}$ of the Gaussian beam (see Fig. 3.3). Note that $\mathbf{n} = -\hat{\mathbf{x}}$ in the isotropic medium given that $\alpha = 0$.

The anisotropy of the medium is a result of the spacetime anisotropy. In that case, the injection momentum $\mathbf{p} = p_x\hat{\mathbf{x}} + p_y\hat{\mathbf{y}}$ is not collinear with the propagation direction[5]. Since we impose that initially the ray propagates along the x-axis, at the injection point the momentum forms an angle with the horizontal given by

$$\frac{p_{y0}}{p_{x0}} = \frac{(1-f)x_0y_0}{x_0^2 + fy_0^2} = \tan\alpha. \tag{3.30}$$

This is exactly the same angle α between the wave normal and the Poynting vector or between the $\mathbf{B}$ and $\mathbf{H}$ fields, all given by Eq. (3.4). As expected, if we set $f = 1$ in Eq. (3.30) for the isotropic medium, we obtain $\alpha = 0$.

[5]See Footnote 3.

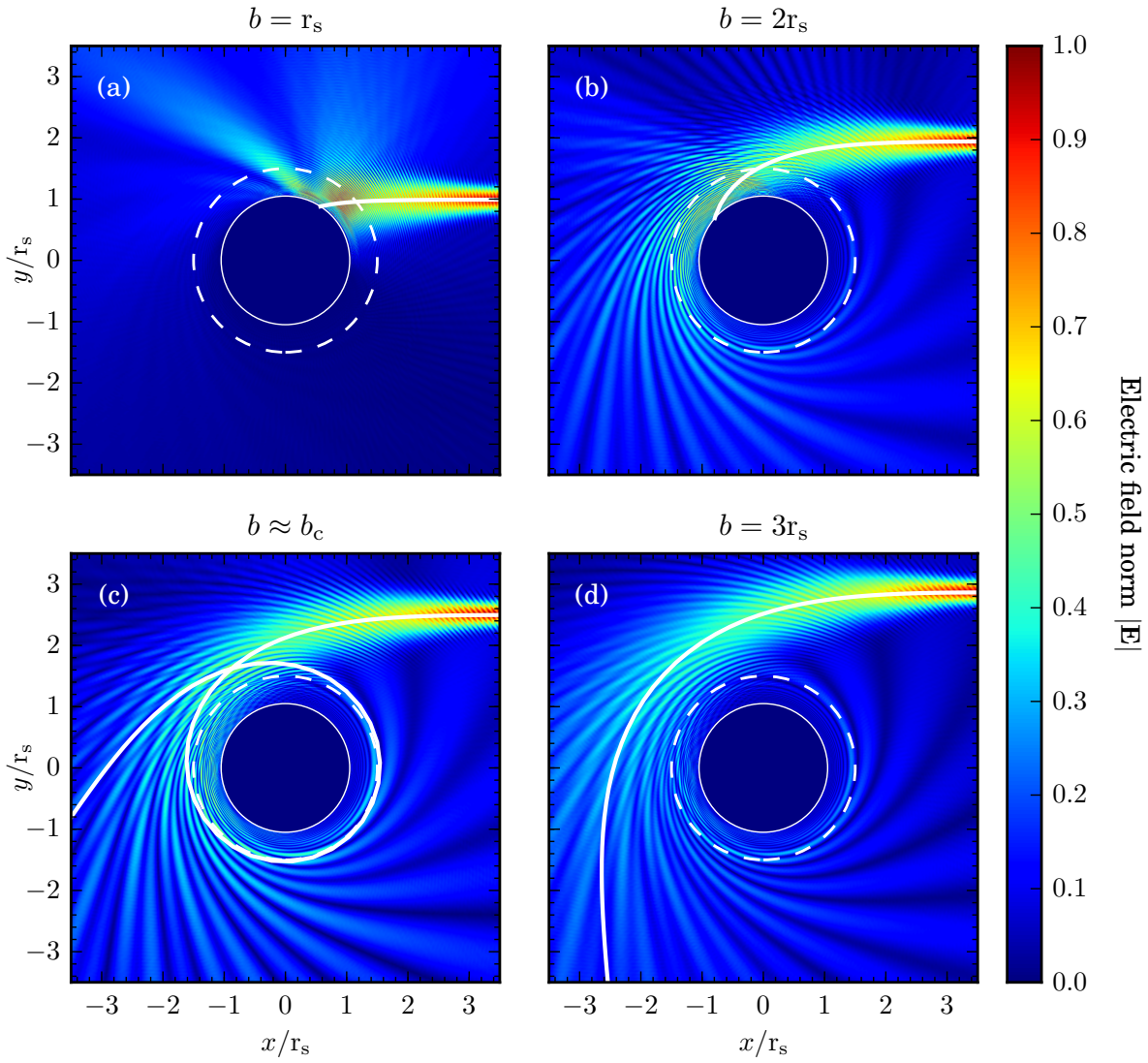

Figure 3.4: Simulation of a TE Gaussian beam of wavelength $\lambda = 0.15\mathrm{r_s}$ and waist radius $w_0 = 0.2\mathrm{r_s}$ compared with ray path (superimposed in white) in an anisotropic metamaterial mimicking the Schwarzschild spacetime for different impact parameters: (a) $b = \mathrm{r_s}$, (b) $b = 2\mathrm{r_s}$, (c) $b \approx b_c$ (slightly above), and (d) $b = 3\mathrm{r_s}$. The event horizon $\mathrm{r_s}$ and the photon sphere of radius $3\mathrm{r_s}/2$ are depicted by white circles with a solid and dashed line respectively. The electric field norm $|\mathbf{E}|$ is given in arbitrary units.

As we have seen in the previous section, the impact parameter b is the key quantity which allows us to distinguish between the different types of ray trajectories. For the geometry we are considering, the value of b can be related to the initial coordinates (x_0, y_0) by means of the following expression:

$$b = y_0 \sqrt{-\frac{g_{rr}}{g_{00}}} \frac{r_0 f}{\sqrt{x_0^2 + f y_0^2}}, \tag{3.31}$$

with the metric parameters taken at $r_0 = \sqrt{x_0^2 + y_0^2}$. Equation (3.31) has been derived under the assumption that the ray velocity lies on the x-axis, $\dot{y} = 0$, at the injection point. It can be verified that at infinity ($r_0 \to \infty$) b approaches y_0, as it should according to the definition of the impact parameter. We remark that this expression is valid for both the anisotropic and isotropic case.

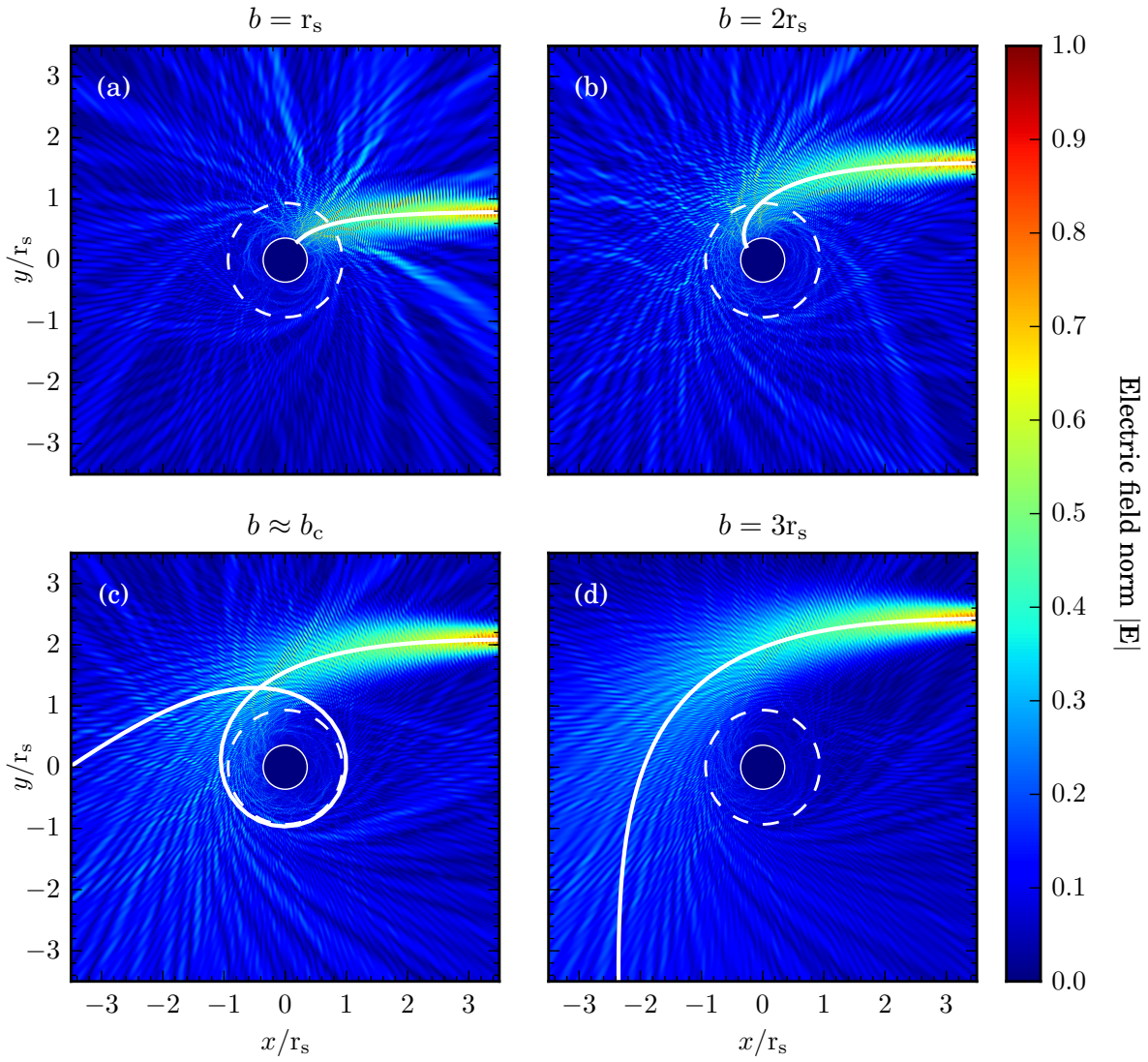

Figure 3.5: Simulation of a TE Gaussian beam of wavelength $\lambda = 0.15\mathrm{r_s}$ and waist radius $w_0 = 0.2\mathrm{r_s}$ compared with ray path (superimposed in white) in an isotropic metamaterial mimicking the Schwarzschild spacetime for different impact parameters: (a) $b = \mathrm{r_s}$, (b) $b = 2\mathrm{r_s}$, (c) $b \approx b_c$ (slightly above), and (d) $b = 3\mathrm{r_s}$. The event horizon $\mathrm{r_s}/4$ and the photon sphere of radius $(2+\sqrt{3})\mathrm{r_s}/4$ are depicted by white circles with a solid and dashed line respectively. The electric field norm $|\mathbf{E}|$ is given in arbitrary units.

In Fig. 3.4 we show the results of the numerical simulations for incident Gaussian beams with different impact parameters b in an anisotropic medium given by Eq. (3.8) mimicking a Schwarzschild black hole (3.1). The ray paths calculated from the Hamilton equations (3.24) are superimposed in white on the wave pattern (shown in color) simulated by solving the wave equation (2.18). We observe a good correspondence between the two approaches: the null-geodesics follow the center of the Gaussian beam even when it deflects. Moreover, the trajectories are consistent with the behaviour expected from theory: we observe ray capture for $b < b_c$ [Fig. 3.4(a),(b)] and deflection for $b > b_c$ [Fig. 3.4(c),(d)]. The full-wave simulations present a more complex behaviour due to interference effects. The Gaussian beam splits into a set of rays or *subbeams*, one part of it is captured due to having $b < b_c$ and another part bends around the photonic sphere of the black hole and interferes with the primary beam. This effect is more pronounced in Figs. 3.4(b),(c) given that the values of b are not very far from the critical value $b_c \approx 2.598$.

It is interesting to see that the subbeams are regularly spaced while bending around the black hole and some of them exhibit smaller subwavelength ripples. Similar behaviour was observed in Ref. [46] for a larger value of the wavelength. Finally, by closely examining Fig. 3.4, we can see that the wavefronts are indeed not perpendicular to the direction of propagation.

In Fig. 3.5 we present the results of the full-wave simulations in an isotropic medium with the refractive index given by Eq. (3.13) that mimics the Schwarzschild metric (3.12), using the same set of the impact parameters b as for the anisotropic case of Fig. 3.4. Again, we observe a good agreement between wave propagation and ray tracing: we obtain either capture or deflection depending on the value of b. The main difference is that now the local velocity of light becomes isotropic and it is determined by a scalar function – the refractive index $n(\rho)$. As a consequence, the interference pattern we observe is substantially different. One can see irregular jets leaving the system in radial directions, similar to those obtained by Genov et al. for isotropic spacetimes [37]. The small ripples observed in the anisotropic case are also clearly seen here too. Since we simulate an isotropic medium, we observe another distinctive feature: the wavefronts are perpendicular to the direction of beam propagation because $\alpha = 0$.

We can also confirm that the ray trajectories for the isotropic and the anisotropic cases are rather similar: the same kinds of orbits (capture or deflection) are observed corresponding to the same value of the impact parameter b. Even if the different choice of coordinates has provided two different materials [45,62], physical properties like the deflection angle between the incoming and outgoing light rays measured by a distant observer at infinity should be equal independently of the coordinate system used. We believe that this is an advantage given that one can choose the most adequate or simplest material for each case.

3.6 Optical black holes based on gradient-index materials

We have seen that we can design a metamaterial that mimics a Schwarzschild black hole, which will capture or deflect light only depending on the impact parameter of the incident beam. Given its spherical symmetry, light coming from any direction could absorbed with this device. This is why optical black holes (that is, metamaterials reproducing black-hole behaviour) are often referred to as "omnidirectional electromagnetic absorbers". Moreover, the capture condition does not depend on the wavelength of the incident light, so we would expect broadband absorption as long as the unit cells of the metamaterial are small enough.

However, some of these interesting properties can be achieved with simpler designs. Researchers have studied both theoretically [37,38,42–44] and experimentally [39–42] optical attractors based on gradient-index materials (GRINs) for which light is deflected or captured for a specific range of impact parameters [63]. These optical black holes consist on an absorbing core (as we chose for our simulation) surrounded by concentrating shell with a spatially-varying refractive index that makes light trajectories bend. This is possible because, to go from one point A to another point B, light rays follow extremal paths according to Fermat's principle. In calculus of variations it can be expressed as [123,140]

$$\delta \int_A^B n(\mathbf{r}) \mathrm{d}\ell = 0, \tag{3.32}$$

where $\mathrm{d}\ell$ is the differential length along the path from A to B and $n(\mathbf{r})$ is the refractive index in the material. If the medium is homogeneous, light will follow a straight line. On the other hand, if the refractive index is a function of the position, this path will be curved. Therefore, one can design a device based on this principle which *attracts* light by bending its trajectory. This effect can be obtained, for instance, with a GRIN that has an isotropic refractive index in the form

$n(r) \sim 1/r^N$ with $N \geq 2$ surrounding the absorbing core [38, 39, 42].

There have been different proposals by authors on how to achieve optical black holes based on GRINs. Until now, most designs have been two-dimensional because one can obtain the main desired features without the complex manufacturing of 3D metamaterials. In that category, we can find multilayered cylindrical structures that achieve the gradient distribution of the refractive index by changing accordingly the size of the meta-atoms of each layer [39, 40]. With this same symmetry, a composite GRIN in which the ratio of the component materials is changed to obtain a variation of the permittivity ε has also been proposed [37, 38]. A different 2D approach was followed by Sheng et al. [42]. They used a microsphere embedded in a planar waveguide to mimic the trapping of light around a black hole or a compact neutron star. The microsphere distorted the surface of the waveguide resulting on a continuous change of the refractive index that could be used to reproduce the gravitational lensing effects. As for spherical designs, 3D printers can be employed to manufacture GRIN structures that act as optical attractors [41]. Other geometries for this absorbing devices such as spheroids and ellipsoids [44] or elliptical cylinders [43] have also been studied.

These types of structures have also inspired similar devices for sound waves such as an omnidirectional broadband acoustic absorber [141, 142]. Alternatively, an omnidirectional acoustic deflector has also been developed [143]. In this case, instead of having a core in the metamaterial that absorbs the incident sound waves, it redirects them to a certain direction regardless of the incidence angle.

We would like to remark the difference between the transformation optics method introduced in Sec. 2.4 to characterize a matematerial equivalent to a spherically symmetric black hole and the omnidirectional absorbers discussed in this section. When using transformation optics, we find the medium parameters that mimic a specific metric. As we have seen, light propagation in the material is analogous to that in the curved spacetime. In fact, numerical simulations in equivalent media could be used to study scattering in curved spacetimes [49]. On the other hand, the label of "optical black holes" includes devices that qualitatively reproduce certain features inspired by cosmological black holes. Due to technological limitations, isotropic metamaterials are easier to manufacture and, therefore, the optical black holes based on GRINs that we have described in this section were the researchers' first approach. Nowadays, more complicated metamaterial structures are being fabricated, thus we believe the next step would be the development of optical black holes based on transformation optics, which may give anisotropic medium parameters. Nevertheless, the omnidirectional absorbers are expected to have important applications in photovoltaic devices or as photon-trapping elements in optical systems [37, 38, 63].

3.7 Conclusions and outlook

In this chapter we have made use of transformation optics to derive the permittivity and permeability of a medium mimicking a static spherically symmetric spacetime. The equivalent material is anisotropic but it has been shown that only one of the anisotropies is essential (either magnetic or electric) depending on the wave polarization (see Sec. 2.4.2). For both anisotropies, light does not propagate in the direction of the wave normal. There is an angle between the phase velocity and the ray velocity, which is related to the anisotropic factor of the metric. The same angle is found in light propagation in the spacetime: due to the curvature, the phase gradient and the direction followed by the ray are different. This deviation must be taken into account in the numerical simulation. We do that by giving an angle to the injected beam. By applying a specific coordinate transformation, a metric with spherical symmetry can be written in a conformally flat

form, which leads to isotropic medium parameters and an inhomogeneous refractive index can be introduced. In this case, energy and phase do propagate in the same direction. In particular, we have applied these results to the Schwarzschild spacetime.

By considering the eikonal approximation in the wave equation, we have obtained the expression for the optical Hamiltonian. We have found that it coincides with the Hamiltonian obtained from general relativity for massless particles. In this way, we have noted that for the spacetime we have considered, the time and space metric coefficients correspond to different properties of the medium: either electric or magnetic. For instance, for the TE-polarized wave, the time dilation term determines the dielectric permittivity of the equivalent medium, while the spatial metric components correspond to its magnetic permeability. This analogy cannot be seen in the isotropic medium characterized by the scalar refractive index.

In order to understand the behaviour of light in the exterior of a Schwarzschild black hole, the differential equations for the null-geodesics in the two coordinate systems considered have been derived. The key quantity to classify the different types of trajectories is the impact parameter. Given that it is a ratio between the angular momentum and energy at infinity, it is independent of the chosen coordinates. The ray paths for both cases have been compared with the corresponding full-wave simulation in the equivalent metamaterial. We have obtained a very good correspondence between the wave propagation and the ray trajectories for both the anisotropic and isotropic media. Since we have used a TE wave in our simulations, the anisotropic medium should be magnetically anisotropic. However, the case of the TM wave in the electrically anisotropic medium perhaps would be easier to realize in the laboratory experiment. Both considerations are theoretically equivalent.

Typically, isotropic metamaterials are easier to manufacture and, consequently, we would expect the case of the inhomogeneous refractive index to be the first approach to mimicking the Schwarzschild black hole. Despite their fabrication difficulty, we believe that metamaterials with certain anisotropies will also be available in the future years due to the rapid progress in metamaterial technology [118, 122, 144, 145]. In that case, other cosmological phenomena could be modelled in the laboratory and many physically interesting properties could be observed.

CHAPTER 4

Static cosmic string

4.1 Introduction

Symmetry breaking phase transitions during the early universe may have led to the formation of cosmic topological defects like strings, domain walls or monopoles. Since they are very different from other more familiar systems, they can give rise to unusual gravitational properties [64–66].

The first direct detection of gravitational waves by the Laser Interferometer Gravitational-Wave Observatory (LIGO) [84] opened up a new way to observe the universe. With this success, there are many hopes that other previously invisible cosmological objects such as these, which emit or scatter gravitational waves, will be observed in the near future. Therefore, it is interesting to study the characteristic wave effects of these systems in order to understand their observational signature.

This chapter is focused on cosmic strings, one-dimensional topological defects with conical curvature. However, such defects are also known to appear in elastic solids and nematic liquid crystals (called disclinations or wedge dislocations) and they are actively studied [70–77]. Conical curvature can be interpreted as the addition or removal of a wedge from a flat geometry (see Fig. 4.1).

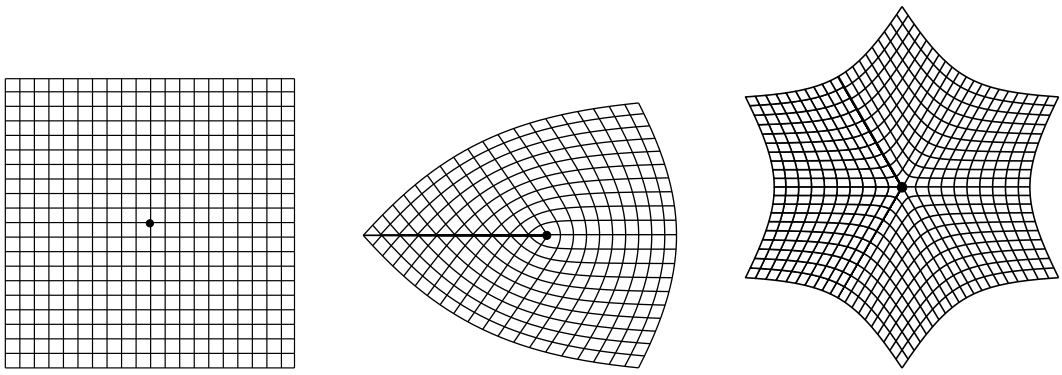

(a) Flat space. (b) Positive curvature. (c) Negative curvature.

Figure 4.1: Disclinations: the flat 2D topology of (a) is distorted when a wedge is (b) removed or (c) added to the geometry. This creates a conical space with (b) positive or (c) negative curvature.

The study of this kind of defects in the geometrical optics limit, or equivalently null-geodesics in general relativity, has been performed by different approaches given that analytical expressions can be easily obtained [52,75,104,105]. Nevertheless, diffraction effects can be of the same order as the geometrical optics terms but due to the complexity of the wave picture, not many detailed studies are available [82,83,99–101]. It should be emphasized that the interference and diffraction effects caused by the cosmic string are substantially different from those of a rod or a slit. For instance, the topological defect gives no shadow region.

In this chapter, we obtain analytical expressions of the wave field in the cosmic string spacetime. By means of the geometrical theory of diffraction, we are able to write it as a sum of four characteristic waves, that allow us to interpret the whole interference picture. In this way, we can also introduce the "Fresnel observation zones" that are associated to the diffraction maxima and that can help localize the regions (of space and frequency) for optimal observation. We use as well the uniform asymptotic theory which provides an accurate analytical expression that is regular in the whole space. Moreover, by applying the equations of transformation optics, we obtain the medium parameters of a metamaterial mimicking conical curvature. We give the full interference and diffraction description of wave propagation in the medium by providing the full-wave numerical simulation and comparing the results with the analytical theories.

4.2 Anisotropic metamaterial mimicking the cosmic string spacetime

4.2.1 Medium parameters

Consider the metric of a static cosmic string described in cylindrical coordinates (r, φ, z) [65,146]

$$\mathrm{d}s^2 = -\mathrm{d}t^2 + \mathrm{d}r^2 + (1 - 4G\mu_\mathrm{S})^2 r^2 \mathrm{d}\varphi^2 + \mathrm{d}z^2, \tag{4.1}$$

where G is the gravitational constant, μ_S is the linear mass density of the string lying along the z-axis and the system of units in which the speed of light $c = 1$ is assumed. With a new angular coordinate $\theta = (1 - 4G\mu_\mathrm{S})\varphi$, the metric (4.1) takes a locally Minkowskian form

$$\mathrm{d}s^2 = -\mathrm{d}t^2 + \mathrm{d}r^2 + r^2 \mathrm{d}\theta^2 + \mathrm{d}z^2, \tag{4.2}$$

having, however, a limitation on the angular range. It is assumed here, that a wedge of angular size $8\pi G\mu_\mathrm{S}$ is taken out and the two faces of the wedge are identified [65, 66]. By introducing the deficit angle 2Δ with

$$\Delta = 4\pi G\mu_\mathrm{S}, \tag{4.3}$$

the angular coordinate θ spans a range of $2\pi - 2\Delta$. Note that Eq. (4.1) also represents the effective geometry of a linear topological defect in condensed-matter systems (e.g., disclination in nematic liquid crystals [74, 75], or wedge dislocation in elastic solids [71]). Cosmic strings formed in the early universe are expected to have a rather small angular deficit, typically with $\Delta \sim 10^{-7}$ [65,66]. In the following sections, we provide simulation results for a larger scale range, $0 < \Delta \lesssim \pi/2$, which is of broader interest in applications and can be easily visualized. Yet, our analytical results are valid in the limit $\Delta \ll 1$ as well.

By applying the transformation optics equation (2.12) to the conical geometry (4.1), one can find the medium parameter tensors to be diagonal in cylindrical coordinates (r, φ, z),

$$\varepsilon^{ij} = \mu^{ij} = \mathrm{diag}\,(\beta, 1/\beta, \beta)\,, \tag{4.4}$$

which can also be written in the usual Cartesian base (x, y, z) as

$$\varepsilon^{ij} = \mu^{ij} = \frac{1}{\beta}\begin{pmatrix} \beta^2\cos^2\varphi + \sin^2\varphi & -(1-\beta^2)\cos\varphi\sin\varphi & 0 \\ -(1-\beta^2)\cos\varphi\sin\varphi & \beta^2\sin^2\varphi + \cos^2\varphi & 0 \\ 0 & 0 & \beta^2 \end{pmatrix}, \tag{4.5}$$

with $\beta = 1-4G\mu_S$. We note that the parameters (4.5) vary with the angle φ but are independent of r and z. This fact is clearly seen in Fig. 4.2, where the spatial distributions of the tensor are plotted. Another distinctive feature is the singularity at the origin, which we will discuss in detail later on. The medium parameters are in agreement with those found in Ref. [51] for the case of a spinning cosmic string when the static condition is assumed.

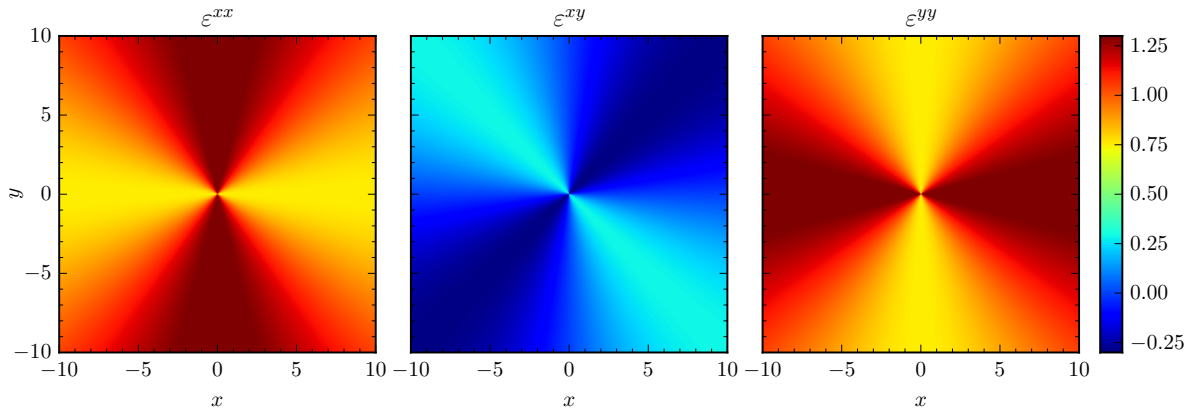

Figure 4.2: Spatial distributions of the components of the medium tensor ε^{ij} for the conical geometry with $\beta = 3/4$. Axes x and y are given in arbitrary units.

As stated in Sec. 2.4.2, we see that $\varepsilon^{xz} = \varepsilon^{yz} = \mu^{xz} = \mu^{yz} = 0$, which allows to eliminate one of the anisotropies by using TE- or TM-polarized waves. Moreover, given that only the z component of the permittivity $\underline{\underline{\varepsilon}}$ enters into the wave equation (2.18), and it is constant [see Eq. (4.5)], one can redefine the electric field $\tilde{E} = \beta E$ and the medium parameters as

$$\tilde{\varepsilon}^{ij} = \delta^{ij}, \quad \tilde{\mu}^{ij} = \delta^{ij} - (1-\beta^2)\begin{pmatrix} \cos^2\varphi & \cos\varphi\sin\varphi & 0 \\ \cos\varphi\sin\varphi & \sin^2\varphi & 0 \\ 0 & 0 & 1 \end{pmatrix}, \tag{4.6}$$

where $\delta^{ij} = \mathrm{diag}\,(1,1,1)$. In this way, the metamaterial has the permittivity $\tilde{\varepsilon}$ of free space and the permeability $\tilde{\mu}$ is inhomogeneous in two dimensions, simplifying its design. We remind that for the TM-polarized wave the substitutions $\varepsilon^{ij} \leftrightarrows \mu^{ij}$, $E \to H$ should be made. In that case, a 2D non-magnetic metamaterial with anisotropic permittivity would be required. Finally, if we write the wave equation (2.18) in polar coordinates for the metamaterial parametrized by Eq. (4.6), we obtain

$$\frac{\partial^2\tilde{E}}{\partial r^2} + \frac{1}{r}\frac{\partial\tilde{E}}{\partial r} + \frac{1}{\beta^2 r^2}\frac{\partial^2\tilde{E}}{\partial\varphi^2} + \omega^2\tilde{E} = 0, \tag{4.7}$$

which is precisely the wave equation in the cosmic string background (4.1) corresponding to a time harmonic source (see, e.g. [82, 83]). This equation will be discussed in detail in Sec. 4.3.

4.2.2 Curvature singularity

A conical spacetime (4.1) is an example of a geometry with a singularity at which the curvature cannot be calculated by standard formulas [147, 148]. Yet one can determine the integral of

the curvature by applying the Gauss-Bonnet theorem that relates the Gaussian curvature K over some region Σ to the geodesic curvature k_g calculated along the smoothly closed boundary $\partial\Sigma$ [137]:

$$\iint_{\Sigma} K\, d\sigma = 2\pi - \oint_{\partial\Sigma} k_g\, \mathrm{d}s. \tag{4.8}$$

On the other hand, the rhs of Eq. (4.8) is the angle a transported frame is rotated through as a result of parallel propagation around $\partial\Sigma$ [148], which we denote by

$$\chi = 2\pi - \oint_{\partial\Sigma} k_g\, \mathrm{d}s \equiv 2\pi - \tilde{\chi}, \tag{4.9}$$

with $\tilde{\chi}$ being the total geodesic curvature. Intuitively, the geodesic curvature measures how far a curve is from being a geodesic, the shortest path between two points [137].

To calculate the curvature for the metric (4.1), let us first determine $\tilde{\chi}$ over a curve which encloses the singularity. We take Σ to be a disk of radius R, at the $z = 0$ plane, centred at $r = 0$, and its circumference $\partial\Sigma$ to be a curve γ parametrized by the arc length s [see Fig. 4.3(a)]. We obtain

$$\tilde{\chi} = \oint_{\gamma} \Gamma^{r}_{\varphi\varphi}\, \dot{\varphi}^2\, \mathrm{d}s = \int_0^{2\pi} \Gamma^{r}_{\varphi\varphi}\, \dot{\varphi}\, \mathrm{d}\varphi, \tag{4.10}$$

with $\Gamma^{r}_{\varphi\varphi}$ being the only relevant Christoffel symbol and $\dot{\varphi} \equiv \mathrm{d}\varphi/\mathrm{d}s$ being the angular velocity in units of the arc length. For the metric (4.1), $\Gamma^{r}_{\varphi\varphi} = -\beta^2 R$ and $\dot{\varphi} = -1/(\beta R)$, so the product $\Gamma^{r}_{\varphi\varphi}\,\dot{\varphi} = \beta$ is constant. That gives $\tilde{\chi} = 2\pi\beta$, meaning that the frame is rotated

$$\chi = 2\pi(1 - \beta), \tag{4.11}$$

which is equal to the angular deficit 2Δ. Hence, the integral curvature of a disk centred at the singularity is $2\pi(1-\beta)$ independently of its radius R.

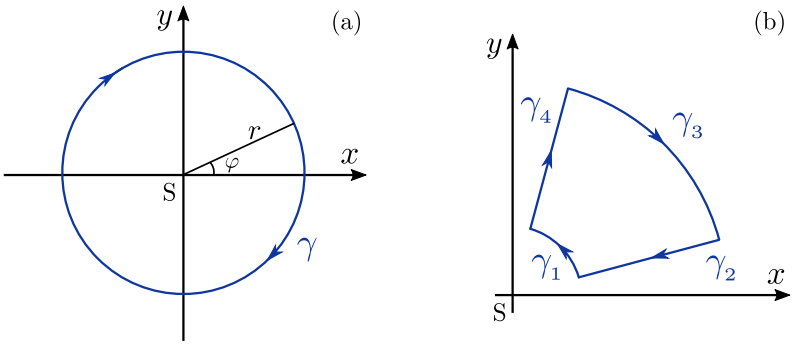

Figure 4.3: Parallel transport along two closed paths in the spacetime of a cosmic string S located at $r = 0$: (a) a circle enclosing the singularity at S, and (b) piecewise path leaving the singularity out.

Next, we consider the closed path that does not enclose the singularity, as shown in Fig. 4.3(b). Since the product $\Gamma^{r}_{\varphi\varphi}\,\dot{\varphi} = \beta$ calculated on the arc is independent of the radius, the integrals over γ_1 and γ_3, following opposite directions, cancel each other out. The paths γ_2 and γ_4 are geodesics (radial lines are not affected by the angular stretching of conical geometry), therefore they do not contribute to the geodesic curvature. As a result, for the total path we get $\tilde{\chi} = 0$. To apply the Gauss-Bonnet theorem for this case, we have to take into account that, instead of a smoothly closed curve, we have a piecewise curvilinear polygon. The theorem still holds, but we must include a correction for the vertices of the polygon where the curve is not smooth [137]. In our case, these are four straight angles, so we obtain $\chi = 2\pi - 4 \cdot (\pi/2) = 0$.

Summarizing the above arguments for the two loops, one can conclude that the Gaussian curvature K for the conical spacetime (4.1) can be defined in terms of a δ-function with its singularity at the origin. Moreover, in a two-dimensional manifold, only one component of the Riemannian curvature tensor is independent and can be related to the Gaussian curvature as $K = R^{r\varphi}{}_{r\varphi}$ [137]. Consequently, the corresponding components of the Riemannian and Ricci tensors can be found in the form [147, 148]

$$R^{r\varphi}{}_{r\varphi} = R^{r}{}_{r} = R^{\varphi}{}_{\varphi} = 2\pi\frac{1-\beta}{\beta}\delta_2(r), \tag{4.12}$$

where $\delta_2(r)$ is a two-dimensional Dirac δ-function in flat space, which is equal to $\delta(x)\delta(y)$ in Cartesian coordinates. In the following, we only consider the case $\beta < 1$ that corresponds to a singularity with positive curvature [Fig. 4.1(b)]. The value of $\beta = 1$ gives an everywhere flat Minkowskian spacetime with no curvature [Fig. 4.1(a)]. The singularity with negative curvature would correspond to $\beta > 1$, that is, the addition of a wedge of 2Δ [Fig. 4.1(c)].

It should be noted that the conical singularity is topological in nature and cannot be eliminated by a coordinate transformation. Therefore, when we consider a metamaterial analogue in flat spacetime by applying the transformation (2.12) to the conical geometry (4.1), the singularity should persist, being embedded, in this case, in the medium parameters. (See Ref. [149] for an application of the Gauss-Bonnet theorem to an effective cosmic string optical metric.) We also notice an interesting property which follows from the Gauss-Bonnet theorem: for the conical spacetime no curve enclosing the singularity could be a geodesic line since it must have a zero geodesic curvature which is in contradiction with Eq. (4.11).

The δ-like curvature has important physical consequences similar to those which arise in the Aharonov-Bohm setting [127]. Photons or particles constrained to move in a region where the Riemann tensor vanishes may nonetheless exhibit physical effects arising from non-zero curvature confined to the string core $r = 0$, i.e. a region from which they are excluded. This can be interpreted as a gravitational analogue of the Aharonov-Bohm effect for a static mass distribution [102, 150–152].

4.3 Wave diffraction by a cosmic string

4.3.1 Wave equation in conical space

We aim to describe wave propagation in conical topology and explain the resulting interference and diffraction effects using analytical theories. To do that, we begin by setting the framework: we write the wave equation in the cosmic string background (4.1) corresponding to a time harmonic source, situated at a finite distance from the string. In order to keep the problem two-dimensional, we consider a line source parallel to the string that emits TE-polarized waves. Our aim is to see how a wave emitted by the line source is diffracted in conical spacetime. The wave equation in background (4.1) for the z-component of the electric field $E(r,\varphi)$ is (see, e.g. [82, 83, 100, 101])

$$\left(\frac{\partial^2}{\partial r^2} + \frac{1}{r}\frac{\partial}{\partial r} + \frac{1}{\beta^2 r^2}\frac{\partial^2}{\partial \varphi^2} + \omega^2\right) E = 0. \tag{4.13}$$

We assume that Eq. (4.13) is also valid for gravitational waves (in an appropriately chosen gauge) when the effect of gravitational lensing on polarization is negligible and can be described by a scalar field [133]. Note that this equation is the same as Eq. (4.7), the wave equation in the metamaterial with parameters (4.6). The line source A is located at $\mathbf{r_0} = (r_0, \pi)$ and emits

cylindrical waves described by [123]

$$E = \mathcal{E}\, H_0^{(1)}(k|\mathbf{r}-\mathbf{r_0}|) \approx \frac{\mathrm{e}^{\mathrm{i}k|\mathbf{r}-\mathbf{r_0}|}}{\sqrt{k|\mathbf{r}-\mathbf{r_0}|}}, \tag{4.14}$$

where $\mathcal{E}$ is a normalization constant and $H_0^{(1)}$ is the Hankel function of the first kind which satisfies the Helmholtz equation (4.13) and corresponds to an outward-propagating solution [123]. It is advantageous to perform the angular transformation $\theta = \beta\varphi$ and to work in the Minkowskian geometry (4.2) with a wedge removed rather than in the metric (4.1). To conveniently perform the transformation, we put the origin at the string location S and join the point S with the source A by a radial line [see Fig. 4.4(a)]. Then we assign respectively the values $\varphi^- = -\pi$ and $\varphi^+ = \pi$ below and above the line SA that will be the cut line. Assuming that the emitting wave is symmetric (isotropic), we obtain a zero derivative $\partial_\varphi U = 0$ at the cut. After the angular transformation, the line SA converts to the wedge SA^-, SA^+, given by the angles $\pm(\pi - \Delta)$ [see Fig. 4.4(b)]. The two faces of the wedge should be identified since they represent the same plane in the spacetime (4.1) [66]. Thus, the propagation of a wave in conical spacetime can be represented as the propagation of two waves in flat geometry with a wedge removed. In our consideration, each emitting source lies on the corresponding face of the wedge.

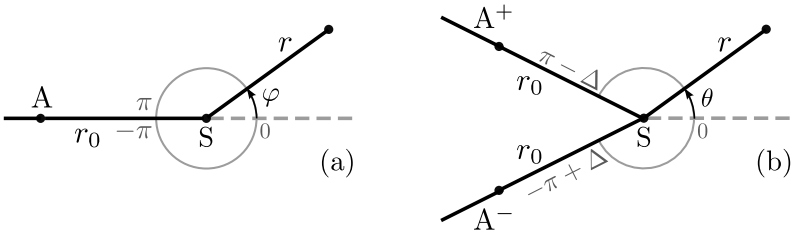

Figure 4.4: Geometry of conical space at the $z = 0$ plane for two equivalent backgrounds with the point S indicating the location of the string: (a) polar coordinates (r, φ) with a source A; (b) Minkowskian coordinates (r, θ) with deficit angle 2Δ and two image sources A^-, A^+.

4.3.2 Geometrical optics limit

To better understand the effects that conical geometry has on wave propagation, let us begin by analysing the null-geodesics. They can be readily found by the same method used in Sec. 3.4. For the Hamiltonian we obtain:

$$2\mathcal{H} = -p_t^2 + p_r^2 + \frac{p_\varphi^2}{\beta^2 r^2}, \tag{4.15}$$

and then, the equations of motion are

$$\dot{t} = -p_t, \quad \dot{r} = p_r, \quad \dot{\varphi} = \frac{p_\varphi}{\beta^2 r^2}. \tag{4.16}$$

Note that p_t and p_φ are conserved quantities for this system as well. They will be determined by the boundary conditions of our problem. Solving these equations, one can find that the conical singularity has the effect of focusing rays whenever $\beta < 1$ (see, e.g. [104]). In (r, θ) representation, the geodesics are simply straight lines and it is easy to see that the area $-\Delta < \theta < \Delta$, the *double-imaging region*, is illuminated by both image sources A^- and A^+. Indeed, an observer located at P_1 in Fig. 4.5 will see two images of the source A. On the other hand, an observer at P_2 will only see one image, being beyond the shadow line for the other image source [66]. Thus, the conical singularity caused by the string gives rise to a double-imaging region behind it, in which

two image sources interfere. From the view of (r, φ) coordinates, there is only one source but the rays passing on opposite sides of the string, are deflected and interfere in the double-imaging region [see Fig. 4.5(a)]. Another important feature of this topology is that the light deflection angle is Δ/β independently of the impact parameter (given that in cosmic strings $\Delta \ll 1$, the deflection angle can be simply approximated by Δ) [65, 98].

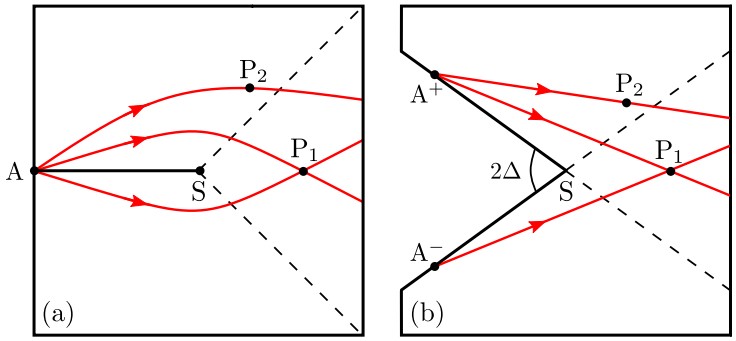

Figure 4.5: Light rays emitted by a source A in the neighbourhood of the string S for the geometry: (a) given by the metric (4.1); (b) Minkowskian geometry (4.2) with a wedge of 2Δ removed and two image sources A^-, A^+ identified. The double-imaging region is bounded by dashed lines.

In the geometrical optics (GO) limit, when the wavelength is small enough, one can construct the field at a point (r, θ) as the sum of two cylindrical waves coming directly from the image sources A^+, A^-. That is,

$$E_{\mathrm{GO}} = \frac{\mathrm{e}^{\mathrm{i}ks^-}}{\sqrt{ks^-}} h^- + \frac{\mathrm{e}^{\mathrm{i}ks^+}}{\sqrt{ks^+}} h^+, \tag{4.17}$$

where $s^\pm = \sqrt{r^2 + r_0^2 + 2rr_0\cos(\Delta \pm \theta)}$ are the path lengths of the GO waves from the image sources A^+ and A^- to the observation point, respectively; and $h^\pm \equiv \Theta(\Delta \pm \theta)$, with $\Theta(x)$ being the Heaviside step function that guarantees that the double-imaging region is determined by $-\Delta < \theta < \Delta$.

4.3.3 Geometrical theory of diffraction

To advance in our analysis, it will be helpful to make use of the canonical problem of diffraction on a perfectly conducting half-plane screen. We can treat the faces of the removed wedge as two half-plane screens. The cylindrical waves emitted by each image source A^+, A^- are diffracted by the corresponding half plane [100, 101].

Half-plane

Let us consider a half-plane screen defined in polar coordinates (r, α) by: $\alpha = 0$ (upper surface) and $\alpha = 2\pi$ (lower surface). According to our geometry, the source is located on the upper surface of the screen at a distance r_0 from the edge, i.e., at $(r_0, 0)$ (see Fig. 4.6).

The emission field is a cylindrical wave that can be defined by [123]

$$E_{\mathrm{i}} = \sqrt{\frac{\pi}{2}} \mathrm{e}^{\mathrm{i}\pi/4} H_0^{(1)}(kR) \approx \frac{\mathrm{e}^{\mathrm{i}kR}}{\sqrt{kR}}, \tag{4.18}$$

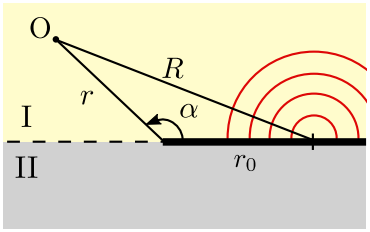

Figure 4.6: Cylindrical wave emitted from a source on the upper surface of a half-plane screen (thick line). The space is split into two regions: (I) illuminated and (II) shadow.

with $R = \sqrt{r^2 + r_0^2 - 2rr_0\cos\alpha}$ and the subscript "i" meaning "incident" field. By means of the geometrical theory of diffraction (GTD) [79], one can write the field as a sum of two waves,

$$E \approx E_\mathrm{i}\,\Theta(\pi-\alpha) + E_\mathrm{i}^0\,D\,\frac{\mathrm{e}^{\mathrm{i}kr}}{\sqrt{kr}}. \tag{4.19}$$

Here, the first term is the geometrical-optics contribution of the incident wave. It is multiplied by the Heaviside step function $\Theta(\pi-\alpha)$ that guarantees that this wave only contributes to the illuminated region (see Fig. 4.6). The second term is the leading order term $\sim O(k^{-1})$ of the diffracted field. It describes a cylindrical wave emanating from the edge (see, e.g. [123]). Its amplitude is given by the product of the incident wave evaluated at the edge, $E_\mathrm{i}^0 \equiv \mathrm{e}^{\mathrm{i}kr_0}/\sqrt{kr_0}$, and the diffraction coefficient [79]

$$D = -\frac{\mathrm{e}^{\mathrm{i}\pi/4}}{2\sqrt{2\pi}}\frac{1}{\cos(\alpha/2)}. \tag{4.20}$$

The expression (4.19) is singular at $\alpha = \pi$, that is, in the neighbourhood of the light-shadow boundary. It should also be remarked that the diffraction coefficient D is determined by the local geometry of the obstacle in the vicinity of the incident ray in the case of corners and edges (a half plane in our case) but it is independent of the type of incident wave [79,81]. Surface plots of the electric field diffracted by a half-plane screen (4.19) can be seen in App. B.

String

We can now construct the GTD electric field in the conical geometry making the angular substitutions $\alpha = \pi - \Delta \mp \theta$ for each half plane in order to work with the coordinates (r,θ). We find [101]

$$E = E_\mathrm{GO} + \frac{\mathrm{e}^{\mathrm{i}kr_0}}{\sqrt{kr_0}}\frac{\mathrm{e}^{\mathrm{i}kr}}{\sqrt{kr}}\,(D^- + D^+), \tag{4.21}$$

with the diffraction coefficients $D^\pm$ (which can also be called "directivity functions") given by

$$D^\pm = -\frac{\mathrm{e}^{\mathrm{i}\pi/4}}{2\sqrt{2\pi}}\frac{1}{\sin\left[\frac{1}{2}(\Delta\pm\theta)\right]}. \tag{4.22}$$

Note that the diffracted (D) waves have a phase shift of $3\pi/4$ whenever the observation point is in the double-imaging region. The terms in Eq. (4.21) are visualised in Fig. 4.7, where each contribution corresponds to a characteristic wave: two GO waves going directly from the sources $A^\pm$ to the observer O and two D waves going from the sources but hitting the edge S – the string location – following extremal paths (Fermat's principle for edge diffraction [79]).

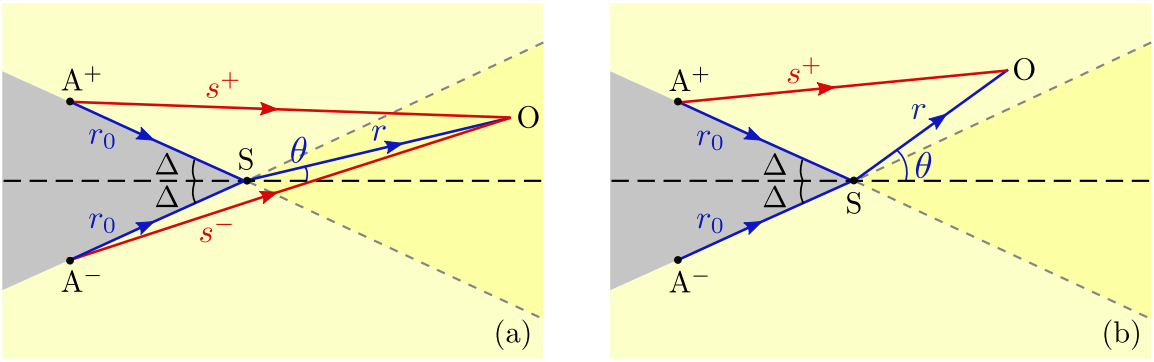

Figure 4.7: Geometrical theory of diffraction in conical space. Direct (red) and diffracted (blue) rays determine the leading order contribution at the observation point O, when O is either in the (a) double-imaging or (b) single-imaging region.

4.3.4 Uniform asymptotic theory

The GTD provides a clear physical interpretation of the diffraction phenomena but the expression diverges at the shadow boundary of the half plane, or equivalently, the double-imaging region boundary for the string. To *regularize* the expressions, one can work in the framework of the uniform asymptotic theory (UAT) to eliminate the singularities [80, 81].

Half-plane

Considering the geometry of Fig. 4.6 and an emitted cylindrical wave described by Eq. (4.18), the solution for the field in the whole space can be expressed as an integral [123, 153–155]

$$E = \sqrt{\frac{2}{\pi}}\, \mathrm{e}^{-\mathrm{i}\pi/4}\, \mathrm{e}^{\mathrm{i}kR} \int_{-w}^{\infty} \frac{\mathrm{e}^{\mathrm{i}u^2}\mathrm{d}u}{\sqrt{u^2+2kR}}, \tag{4.23}$$

where $w = \sigma\sqrt{k(r+r_0-R)}$, with $\sigma \equiv \operatorname{sgn}[\cos(\alpha/2)]$, a sign function giving $+1$ in the illuminated region and -1 in the shadow. Instead of working with the solution in the integral representation (4.23), we apply the UAT [80, 81], which has proved to be quite accurate in finding solutions for the wave field under diffraction. We seek the solution in the form

$$E = E_{\mathrm{i}}\, \mathcal{F}(w) + \mathcal{R}, \tag{4.24}$$

where the first term is the penumbra field with the Fresnel integral defined by

$$\mathcal{F}(w) = \frac{1}{\sqrt{\pi}\mathrm{i}} \int_{-\infty}^{w} \mathrm{e}^{\mathrm{i}u^2}\mathrm{d}u \tag{4.25}$$

and $\mathcal{R}$ offsets the residual arising from substituting the penumbra term in the wave equation. In both Eqs. (4.23) and (4.24), the Neumann boundary condition for the field is assumed on the screen. The residual $\mathcal{R}$ has the form of a ray expansion

$$\mathcal{R} = \mathrm{e}^{\mathrm{i}k(r+r_0)} \sum_{n=1}^{\infty} k^{-n} C_n, \tag{4.26}$$

in which the slowly varying coefficients C_n can be determined by the method of asymptotic matching [81] which consists in comparing the uniform asymptotics (4.24) with the nonuniform asymptotics of the rigorous solution and expanding all the terms with respect to inverse powers

of k. The nonuniform expansion corresponds to the GTD expression (4.19), which is valid at $|w| \gg 1$.

To do the asymptotic matching, the Fresnel integral (4.25) is replaced with its asymptotics at large arguments [78]

$$\mathcal{F}(w) \approx \Theta(w) - \frac{e^{i\pi/4}}{2\sqrt{\pi}} \frac{e^{iw^2}}{w} \equiv \Theta(w) - \tilde{\mathcal{F}}(w). \tag{4.27}$$

By comparing Eqs. (4.24) and (4.19) up to the order $O(k^{-1})$, we see that only C_1 is relevant in the expansion (4.26) and for the residual $\mathcal{R}$ we obtain

$$\mathcal{R} \approx E_i \tilde{\mathcal{F}} + E_i^0 D \frac{e^{ikr}}{\sqrt{kr}}. \tag{4.28}$$

Substituting in Eq. (4.24), one can write the final solution

$$E \approx E_i (\mathcal{F} + \tilde{\mathcal{F}}) + E_i^0 D \frac{e^{ikr}}{\sqrt{kr}}. \tag{4.29}$$

Written in this form, the solution (4.29) corresponds to the uniform asymptotic theory introduced in Ref. [80]. It is called uniform since the poles in the diffraction coefficient D are cancelled out by the poles in the term $\tilde{\mathcal{F}}$, giving a regular solution in the whole space including the light-shadow boundary. It would be convenient to combine both singular terms in one by defining a new diffraction coefficient

$$\tilde{D} = -\frac{e^{i\pi/4}}{2\sqrt{2\pi}} \left[\frac{1}{\cos(\alpha/2)} - \sigma \sqrt{\frac{2rr_0}{R(r + r_0 - R)}} \right], \tag{4.30}$$

and the uniform solution finally becomes

$$E \approx E_i \mathcal{F}(w) + E_i^0 \tilde{D} \frac{e^{ikr}}{\sqrt{kr}}. \tag{4.31}$$

Note that Eq. (4.31) is valid at any distances from the light-shadow boundary, near and away from the edge, i.e. everywhere except for the neighbourhood of the source, since $kR \gg 1$ is assumed. Far from the light-shadow boundary, both asymptotics, the nonuniform (4.19) and uniform one (4.31), coincide. We also observe that the edge wave has a phase shift of $-3\pi/4$ in the illuminated region and $+\pi/4$ in the shadow with respect to the incident field. Crossing the shadow line introduces a phase change of π, which is manifested in the sign change of the diffraction coefficients D and $\tilde{D}$ (See the original work by Fresnel [156,157] who pointed out that the diffracted waves in the shadow and illuminated regions are in complete phase opposition). Supplementary plots of the electric field diffracted by a half-plane screen (4.31) are provided in App. B.

String

Finally, after applying the transformation $\alpha = \pi - \Delta \mp \theta$ to each half plane, we obtain the UAT solution for the electric field in the cosmic string spacetime as [101]

$$E = \frac{e^{iks^-}}{\sqrt{ks^-}} \mathcal{F}(w^-) + \frac{e^{iks^+}}{\sqrt{ks^+}} \mathcal{F}(w^+) + \frac{e^{ikr_0}}{\sqrt{kr_0}} \frac{e^{ikr}}{\sqrt{kr}} \left(\tilde{D}^- + \tilde{D}^+ \right), \tag{4.32}$$

with the modified diffraction coefficients $\tilde{D}^\pm$ defined as

$$\tilde{D}^\pm = -\frac{e^{i\pi/4}}{2\sqrt{2\pi}} \left[\frac{1}{\sin\left[\frac{1}{2}(\Delta \pm \theta)\right]} - \sigma^\pm \sqrt{\frac{2rr_0}{s^\pm(r + r_0 - s^\pm)}} \right], \tag{4.33}$$

and the notations $w^{\pm} = \sigma^{\pm}\sqrt{k(r + r_0 - s^{\pm})}$ and $\sigma^{\pm} = \mathrm{sgn}(\Delta \pm \theta)$.

It is easy to check that for $\Delta = 0$, i.e. when there is no string, both the GTD (4.21) and UAT (4.32) reduce to

$$E_0 = \frac{\mathrm{e}^{\mathrm{i}ks_0}}{\sqrt{ks_0}}, \tag{4.34}$$

which is a usual cylindrical wave with $s_0 = \sqrt{r^2 + r_0^2 + 2rr_0\cos\theta}$. For future analysis, one can define the amplification factor $F = |E/E_0|$ to characterize the effect the presence of the string has over the field.

4.3.5 Plane wave propagation in conical space

If the distance from the source to the string goes to infinity, one can neglect the effects of wavefront curvature and consider the incidence of a plane wave. It should be remarked that the diffraction of a plane wave by a perfectly conducting half-plane screen was solved *exactly* by Sommerfeld [78]. For the geometry we have considered, an infinitely distant source corresponds to a plane wave grazing the screen (see Fig. 4.8). The exact solution for the field at any point (r, α) can be written in the compact form

$$E = \mathrm{e}^{-\mathrm{i}kr\cos\alpha}\mathcal{F}\left(\sqrt{2kr}\cos\frac{\alpha}{2}\right). \tag{4.35}$$

Note that we have taken into account the Neumann boundary condition on the screen, $\partial_\alpha E(r, 0){=}0$. It can be verified that the solution (4.35) contains both the GO and D fields. Indeed, for the angles $0 < \alpha < \pi$, in the limit $kr \to \infty$ far away from the edge, one gets $\mathcal{F} \to 1$ and $E = \mathrm{e}^{-\mathrm{i}kr\cos\alpha}$, which is the GO incident field. Whereas, for the angles $\pi < \alpha < 2\pi$, one obtains $\mathcal{F} \to 0$ giving $E = 0$ at infinity. The Fresnel function $\mathcal{F}$ smooths the discontinuity of the GO solution across the shadow boundary $\alpha{=}\pi$ making the total field continuous everywhere (see App. B for further details and figures). This smooth transition constitutes the diffraction phenomenon [78]. It should also be noted that the original Sommerfeld problem treats two possible boundary conditions on the screen (Dirichlet or Neumann) depending on the polarization of the incident field. However, for grazing incidence, only one polarization can propagate and that corresponds to the Neumann condition. Moreover, the zero field condition would be unphysical for the conical space we consider.

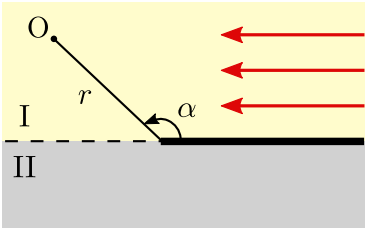

Figure 4.8: Plane wave grazing a half-plane screen (thick line). The entire space is split into two regions: illuminated (I) and shadow (II).

Having defined the solution for a single half plane, we can readily obtain the electric field in the conical geometry [100],

$$E = \mathrm{e}^{\mathrm{i}kr\cos(\Delta+\theta)}\mathcal{F}(u^+) + \mathrm{e}^{\mathrm{i}kr\cos(\Delta-\theta)}\mathcal{F}(u^-) \tag{4.36}$$

with $u^{\pm} = \sqrt{2kr}\sin[(\Delta \pm \theta)/2]$. It is easy to verify that for $\Delta = 0$, it reduces to the unlensed field $E_0 = \mathrm{e}^{\mathrm{i}kr\cos\theta}$, which is a usual plane wave in Minkowskian space. Performing the asymptotic

expansion of the Fresnel integral (4.27), the division in GO and D waves of the GTD can be obtained as [100]

$$E = \mathrm{e}^{\mathrm{i}kr\cos(\Delta+\theta)}h^{+} + \mathrm{e}^{\mathrm{i}kr\cos(\Delta-\theta)}h^{-} + \frac{\mathrm{e}^{\mathrm{i}kr}}{\sqrt{kr}}(D^{-}+D^{+}), \tag{4.37}$$

with the same definition of the diffraction coefficients $D^{\pm}$ of Eq. (4.22). It is important to remark that, even if the solution for the field diffracted by the half-plane screen (4.35) is exact, the expression (4.36) for the string is not. However, as long as the D field decays to 0 as it approaches the opposite half planes, $\theta \to \pm(\pi - \Delta)$, our assumptions in the model are justified. To check that, we plot one of the diffraction coefficients, D^{+}, in Fig. 4.9 as a function of θ for $\Delta = \pi/5$. (Note the discontinuity at the shadow boundary for the A^{+} source, now corresponding to one of the double-imaging region boundaries.) We observe that the coefficient reaches an almost negligible value at the opposite screen, i.e. $\theta = -4\pi/5$. We believe this will not substantially affect the boundary conditions for the A^{-} source, adding only minimal error. Instead of using the two half-plane screens, this problem could also be considered as the diffraction by a wedge or a cone but with different boundary conditions appropriately chosen for the new setting [158–160].

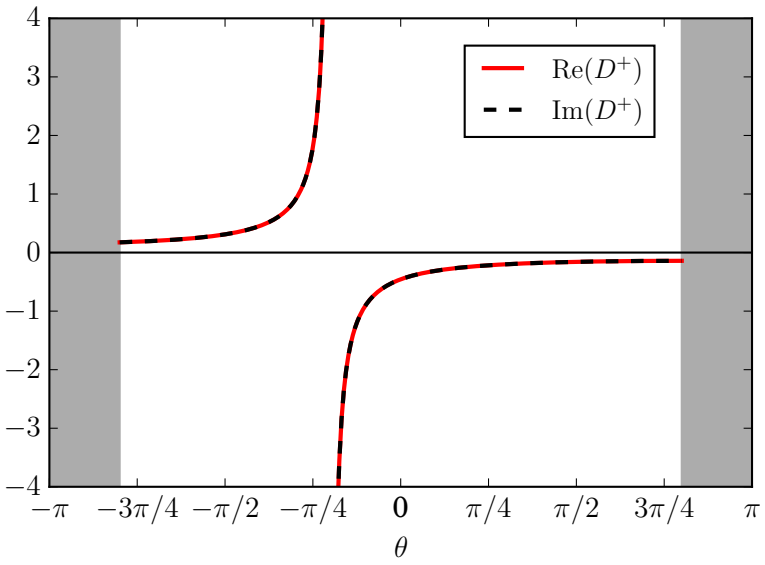

Figure 4.9: Real and imaginary part of the diffraction coefficient D^{+}, given by Eq. (4.22), for a defect with $\Delta = \pi/5$. The shadowed regions correspond to the subtracted wedge in the Minkowskian geometry. (The case for D^{-} would be completely equivalent.)

The plane wave case can be understood as a limit of the cylindrical wave for a distant source. Thus, the expressions for grazing plane wave incidence can also be obtained by multiplying the line-source results by $\sqrt{kr_0}\mathrm{e}^{-\mathrm{i}kr_0}$ and letting $r_0 \to \infty$ [154].

4.4 Fresnel observation zones

The Fresnel-zone concept has been widely used in various branches of wave physics. When the wave field is calculated at a certain observation point, it is advantageous to divide an incoming wavefront into a number of zones, each with an additional path difference of a half-wavelength, so that the wavefront phase changes by π when moving from one zone to the next [78, 123]. The construction of these zones provides a pictorial understanding of the diffraction phenomenon. Indeed, when some of the zones are obstructed by a screen or any other obstacle, the Fresnel

zones are used to determine qualitatively when the diffraction effects become important and the geometrical optics limit is not accurate enough to estimate the resulting field. For example, when radio waves propagate in terrain environment, Fresnel zones are elliptic-shaped regions surrounding the line-of-sight path from source to receiver. Using this construction, one can determine how disturbing objects affect wave transmission [161].

It should be noted that diffraction may appear in the absence of screens or obstacles which might obstruct the direct wave transmission. As Fresnel pointed out in his classical work [156, 157], in order to produce the phenomena of diffraction "all that is required is that a part of the wave should be retarded with respect to its neighbouring parts." This is precisely what happens both in the metamaterial medium with the anisotropic parameters and in the gravitational lensing effect produced by the cosmic string. When a gravitational or electromagnetic wave passes near a massive cosmological object, it deviates and it may give rise to multiple images and diffraction patterns [67–69]. A similar effect appears when the wave propagates near a topological defect like a cosmic string [83, 100, 101, 162], as we will explain in this section.

4.4.1 Hyperbolic vs. elliptic zones

For the problem of transmission of a signal from the source A to the observer O, the Fresnel zones can be constructed about the line of sight AO connecting the points. In this case, the relevant geometry is a set of confocal elliptic-shaped regions with the foci at the points A and O [161]. Indeed, when any obstacle S is not far from the line of sight, an alternative path $AS + SO$ interferes with the direct path AO resulting in constructive or destructive interference. The result depends on the phase difference between the paths [see Fig. 4.10(a)]. If the points A and O are fixed, while S is moved over the space, the line of constant phase difference is elliptic. The objective of such construction is to determine clearance zones in order to achieve perfect transmission between the emitter and the receiver [161].

However, for our case this zone construction is not convenient since (i) we have two image sources instead of one, and (ii) we are interested in just the opposite – in how to detect the scattering object using the presence of wave effects in the observed signal, or in other words, where we should place the observer with the aim to detect the obstacle by virtue of diffraction with the highest efficiency. To this purpose we fix the points A and S, while the observer O is moved over the space [Fig. 4.10(b)]. By this procedure the line of constant phase difference between the two paths will be hyperbolic instead of elliptic (at the moment we assume a Minkowskian geometry).

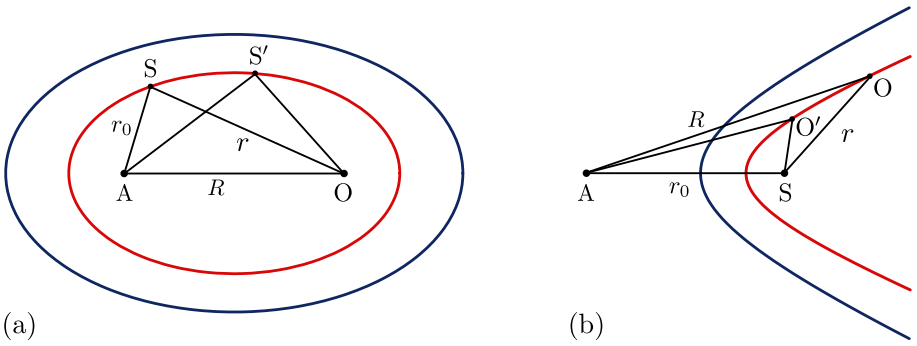

Figure 4.10: Lines of constant phase difference between the direct path $|AO| = R$ and the diffracted path $|AS| + |SO| = r_0 + r$. Their shape is: (a) elliptic when the distance R is fixed; (b) hyperbolic when r_0 is fixed.

4.4.2 Half plane

This idea can easily be implemented to our equations. First, consider the case of a single half plane with the geometry of Fig. 4.6. The penumbra term in Eq. (4.31) is determined by the Fresnel function of argument w, that depends on the path difference $d \equiv r + r_0 - R$. Hence, one can define the zone structure by the condition that d should be an integer number of half wavelengths:

$$r + r_0 - \sqrt{r^2 + r_0^2 - 2rr_0\cos\alpha} = \frac{\lambda}{2}\, j, \tag{4.38}$$

that means the phase between the paths changes by π when moving from one zone to the next – a similar argument used by Fresnel to define the zone boundaries on the wavefront [156, 157]. From this equation, the shape of the zones in polar coordinates (r, α) will be determined by a familiar expression for conic sections [101]

$$r = \frac{r_0}{2e_j}\,\frac{e_j^2 - 1}{1 + e_j\cos\alpha}, \tag{4.39}$$

with eccentricity e_j given by

$$e_j \equiv \left(1 - \frac{\lambda}{2r_0}\, j\right)^{-1}. \tag{4.40}$$

Equation (4.39) describes a set of confocal hyperbolas (for $j = 1, 2, 3, \dots$), all with one focus at the source A and the other at the edge of the screen S, so that the path difference from each focus to a point on the curve is constant [see Fig. 4.11(a)]. Each hyperbola, in principle, should have two symmetrical branches corresponding to either $R > r$ or $R < r$. Since the latter case is not relevant for our physical conditions, we only consider the branches in the neighbourhood of the focus S with $R > r$. Moreover, we are only interested in those parts of the branches which are located in the upper (illuminated) region where the direct and diffracted paths interfere. In the lower (shadowed) region no interference effects are expected since there is only the diffracted wave (this part of the hyperbola is plotted in a dashed line). The vertices of the hyperbolas are given by the coordinates $(\frac{1}{4}\lambda j, 0)$, so that they are equidistantly spaced by $\frac{1}{4}\lambda$ between $r = 0$ and $r = r_0/2$ along the screen. The asymptotes of the hyperbolas determine the limits for the angle α for each zone: $-\alpha_j^* < \alpha < \alpha_j^*$ with $\alpha_j^* = \arccos(-e_j^{-1})$. We also notice that for our geometry and due to the requirement $1 < e_j < \infty$ for hyperbolas, there is an upper limit for the index j given by $j_{\max} = 2r_0/\lambda$. Finally, for an infinitely distant source (incident plane wave, Eq. (4.35)), one focus goes to infinity, $r_0 \to \infty$, and the path difference is simply $d = r(1 + \cos\alpha)$, while the

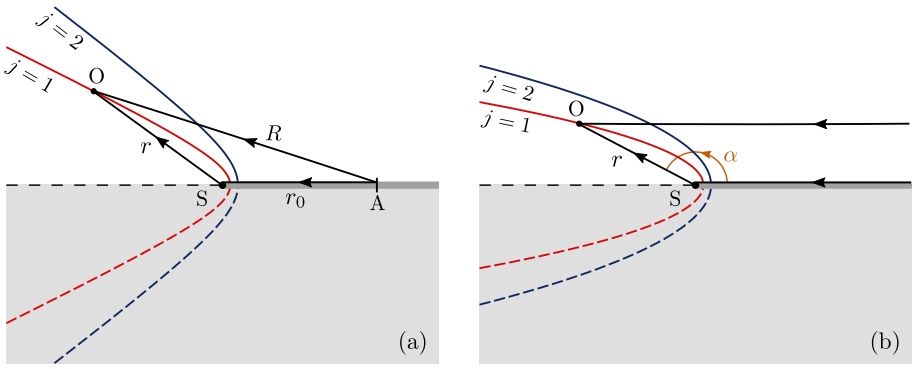

Figure 4.11: Lines of constant phase for the case of diffraction on a half-plane screen: (a) the source A is at a distance r_0 from the edge S, the lines are hyperbolic; (b) the source is at infinity (plane wave incidence), they are parabolic.

hyperbolas become parabolas with the single focus at the edge S [see Fig. 4.11(b)]. The shape of the parabolas is determined by [100]

$$r = \frac{\lambda}{2} \frac{j}{1 + \cos\alpha}. \tag{4.41}$$

4.4.3 String

Next, we consider the geometry of Fig. 4.4(b) corresponding to the string, which is flat space with a wedge removed and two sources located on the faces of the wedge. A qualitative analysis of the GTD expression (4.21) shows that in the most interesting situation, when the observer is in the double-imaging region, the diffraction pattern will be determined by the interference of four characteristic waves: two GO waves coming from the sources and two D waves emanating from the edge [Fig. 4.7(a)].

First of all, from geometrical optics (4.17) we would expect the following picture: two GO waves interfering with each other, constructively or destructively, to produce an interference pattern of bright and dark lines alternating in space. The phase difference between the GO waves is constant along the lines $s^- - s^+ =$ constant, which are confocal hyperbolas with the foci at the sources A^- and A^+. If we specify the path difference in units of the half wavelength:

$$s^- - s^+ = \frac{\lambda}{2} q \tag{4.42}$$

with $q \in \mathbb{Z}$ being an integer, the bright lines (constructive interference) correspond to even $q = 0, \pm 2, \pm 4, \ldots$, while the dark lines (destructive interference) correspond to odd values $q = \pm 1, \pm 3, \ldots$. In the following, we will refer to the bright and dark GO lines as "antinodal" and "nodal" lines, respectively.

The diffracted waves introduce new important features into the overall interference pattern. As we pointed out for the case of a half plane, the phase difference between the GO and D waves is constant along the hyperbolas $r + r_0 - s^- =$ constant and $r + r_0 - s^+ =$ constant, for the sources A^- and A^+, respectively. The condition for destructive and constructive interference will now be different from that of Eq. (4.42). D waves acquire an additional phase shift of $3\pi/4$ by hitting the edge, which is manifested by virtue of the phase in the diffraction coefficients (4.22). Therefore, we would expect the maxima and minima of the field intensity when these two conditions are fulfilled simultaneously:

$$r + r_0 - s^+ = \frac{\lambda}{2} \left(n + \frac{3}{4} \right), \tag{4.43}$$

$$r + r_0 - s^- = \frac{\lambda}{2} \left(m + \frac{3}{4} \right) \tag{4.44}$$

with m, n being non-negative integers: $0, 1, 2, 3, \ldots$ The solutions are the intersection points of two families of hyperbolas corresponding to each source. If we now subtract Eqs. (4.43) and (4.44), we get Eq. (4.42) with $q = n - m$, that means these intersection points lie precisely on the nodal and antinodal GO lines. Thus, we would expect that the additional interference with the D waves may lead to a further amplification of the field on the antinodal lines. The points of most interest are the global maxima, which occur when the two GO and the two D waves are all in phase, that corresponds to having all three numbers, n, m, and q, even. Denoting the intersection points by a pair of numbers (n, m), the highest maximum occurs at the point $(0, 0)$ which is located at the line of sight (central antinodal line). The next-order maxima are $(0, 2)$ and $(2, 0)$ lying symmetrically out of the line of sight at a larger distance from the string and having,

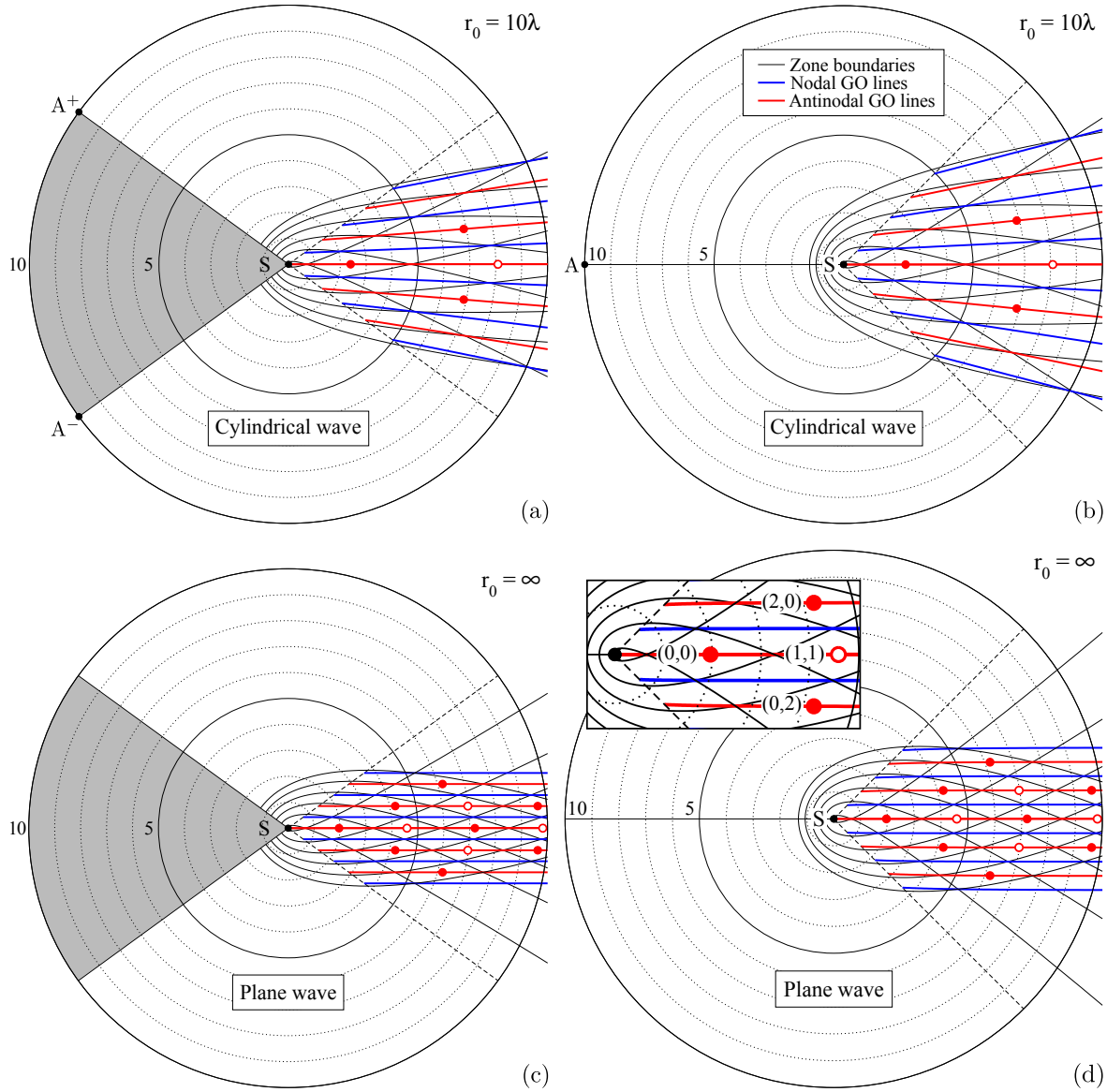

Figure 4.12: Observation zones associated with interference and diffraction of waves by a cosmic string: (a),(b) the source A is at a finite distance $r_0 = 10\lambda$ from the string S; (c),(d) the source is at infinity (incident plane wave). Each case is shown for two coordinate systems: (a),(c) Minkowskian (4.2) with a wedge removed, and (b),(d) the one corresponding to Eq. (4.1). For a better view, a rather large value of the deficit angle $\Delta = \pi/5$ is taken. Dashed lines indicate the limits of the double-imaging region. Red points indicate the maxima of the field intensity, while red circles correspond to saddle points. Inset in (d): the points are labelled with (n, m) indices.

therefore, lower magnitude. They are followed by more distant maxima $(0, 4)$, $(2, 2)$, $(4, 0)$, and so on (see Fig. 4.12). An important special case occurs when n and m are odd simultaneously (accordingly q is even). These are the saddle points of the field intensity which are located at the antinodal GO lines, e.g., $(1, 1)$, $(3, 1)$, $(1, 3)$, etc. This situation corresponds to a local minimum due to the D waves in a bright GO line. On the other hand, on the nodal lines, D waves do not substantially affect the wave field intensity due to the dominating destructive interference between the GO waves.

For further analysis, one can define the observation zones, $\mathcal{Z}_{nm}$, associated with the points (n, m), which are the characteristic points of interference between the GO and D waves. Since

an increase by 1 in indices corresponds to changes by π in phase, we define the zones as delimited by the hyperbolic lines (4.43) and (4.44) with the substitution: $n \to n \pm \frac{1}{2}$ and $m \to m \pm \frac{1}{2}$. In this way, four hyperbolas enclose a region with each interference point (n, m). We refer to $\mathcal{Z}_{nm}$ as "Fresnel observation zones", since the zone structure is basically determined by Fresnel diffraction. The zone boundaries can be defined explicitly by the hyperbolas (see Eq. (4.39) for comparison):

$$r = \frac{r_0}{2e_j} \frac{e_j^2 - 1}{1 - e_j \cos(\Delta \pm \theta)}, \tag{4.45}$$

with eccentricity

$$e_j = \left[1 - \frac{\lambda}{2r_0}\left(j + \frac{3}{4}\right)\right]^{-1}. \tag{4.46}$$

For each zone $\mathcal{Z}_{nm}$ we have to substitute: $j = n - \frac{1}{2}$, $n + \frac{1}{2}$ for the upper sign and $j = m - \frac{1}{2}$, $m + \frac{1}{2}$ for the lower sign in Eq. (4.45). (The two different signs refer to the image sources $A^{\pm}$.) The structure of Fresnel observation zones is depicted in Fig. 4.12. Here, the zones bounded by the hyperbolas (4.45) are shown in black along with the GO antinodal (in red) and nodal (in blue) lines. Note that the interference between the GO waves takes place only in the double-imaging sector (delimited by dashed lines). Outside of it, the wave field is determined by interference of one GO and two D waves. Therefore, one would expect that in the single-imaging region, the bright (antinodal) and dark (nodal) lines to be given by Eq. (4.43) above, and Eq. (4.44) below the string location.

The Fresnel-zone structure for plane wave incidence [see Eq. (4.37)] can be obtained by similar arguments. It is depicted in Fig. 4.12(c),(d). In this case, the antinodal and nodal GO lines of Eq. (4.42) simply become straight lines parallel to the line of sight. They are given by

$$2r \sin\theta \, \sin\Delta = \frac{\lambda}{2} q, \tag{4.47}$$

with q being an integer. One can see that the separation between these lines is constant. This means that the typical fringe separation in the observation plane is $\delta y = \lambda/(2\sin\Delta) \approx \lambda/(2\Delta)$, which is independent of the distance (even in space (4.1) whenever $\Delta \ll 1$). This is different from what happens in the diffraction by a compact object, where they tend to spread out (see, e.g. [68,69]). As seen for the half plane, the lines of constant phase between the GO and D waves become parabolas for plane wave incidence [100]: $r[1 - \cos(\Delta \pm \theta)] =$ constant. On the other hand, the phase shift in diffraction coefficients does not change when the source goes to infinity, therefore the conditions to find the maxima and minima will be similar to Eqs. (4.43) and (4.44), in which the indices n and m will identify the intersection points of the parabolas:

$$r[1 - \cos(\Delta + \theta)] = \frac{\lambda}{2}\left(n + \frac{3}{4}\right), \tag{4.48}$$

$$r[1 - \cos(\Delta - \theta)] = \frac{\lambda}{2}\left(m + \frac{3}{4}\right). \tag{4.49}$$

Since parabolas are the conic sections with eccentricity $e = 1$, the parabolic Fresnel zones will be determined simply by

$$r = \frac{\lambda}{2} \frac{j + 3/4}{1 - \cos(\Delta \pm \theta)}, \tag{4.50}$$

with j defined below Eq. (4.46). These zones are depicted in Fig. 4.12(c).

Finally, in order to obtain the observation zones in space (4.1), the angular transformation $\theta = \beta\varphi$ should be performed. As shown in Fig. 4.12(b),(d), this angular stretching distorts somewhat the shape of the curves, particularly as the angle increases. On the string's line of

sight (θ=φ=0), however, the boundaries between the zones, as well as the maxima, coincide for both backgrounds.

It would be interesting to compare these predictions with the wave field in (r, φ) space. To do that, we provide a density plot of the amplification factor calculated from the full-wave expression (4.36) and we superimpose: the nodal and antinodal lines in Fig. 4.13(a), and the hyperbolas (4.48),(4.49) that determine the diffraction maxima in Fig. 4.13(b). Given the excellent correspondence we observe, the previous equations can be used to estimate some numbers. For instance, the position of the highest diffraction maximum can be found by substituting $m = n = 0$ and $\varphi = 0$. For $\Delta = \pi/6$, this gives $x \approx 2.8\lambda$. The next-order maxima ($n = 2$ and $m = 0$ and vice versa) are at $x \approx 5.9\lambda$ and $y \approx \pm 1.2\lambda$, while the fringe separation for this Δ should be $\delta y \approx 1.2\lambda$. All these values are seen to be in agreement with Fig. 4.13.

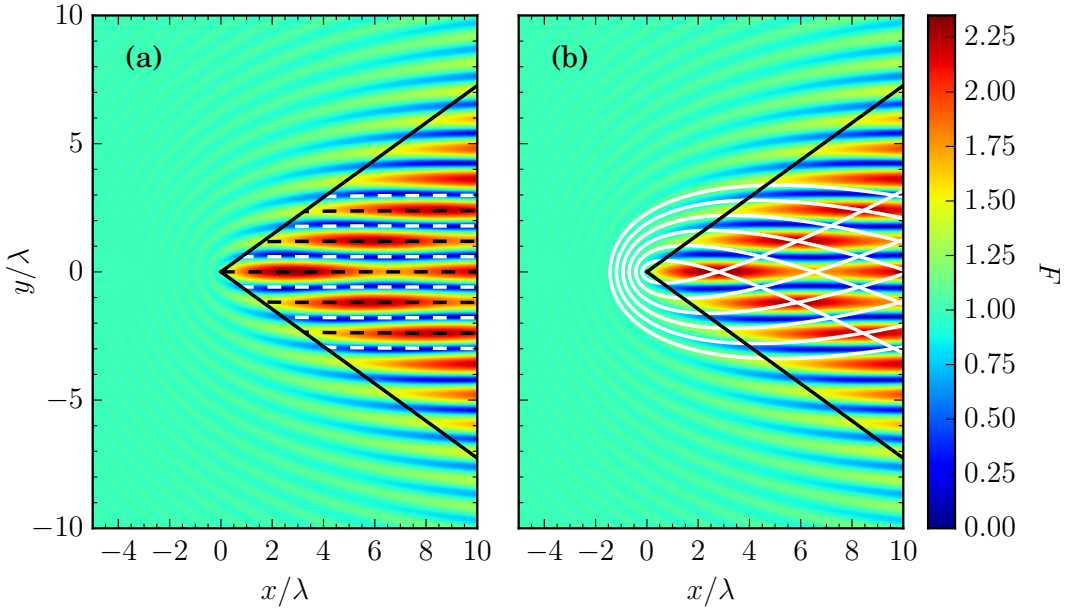

Figure 4.13: Density plot of the amplification factor F for plane-wave propagation in conical space with $\Delta = \pi/6$ calculated from the full-wave expression (4.36). In (a) white and black dashed lines correspond to the nodal and antinodal lines, respectively. Intersection of the interference parabolas depicted in white in (b) determine the diffraction maxima.

The construction of Fresnel zones can also be carried out for other geometries. For instance, one can study a three-dimensional case with a point source emitting spherical waves, for which the analytical formulas for diffraction on a half plane are also known [153, 155]. The surfaces of constant phase between the GO and D waves, though with more involved shapes, can also be obtained. To find the global diffraction maxima, what is needed is the value of the phase shift acquired by the D wave when hitting the string following the shortest path. It does not depend on the type of incident wave but on the obstacle [79, 81], having the value of $3\pi/4$ we have found for the conical space (4.1). We also note that for a far distant source, one can neglect the curvature of the wavefront and use the plane-wave approximation. In this limit, we expect the Fresnel zones to be hyperbolic cylinders having one focus on the string and the position of the other will depend on the tilted angle of incidence. In case of perpendicular incidence, the cylinders will become parabolic.

4.5 Discussion of the results

In this section we present results based on the analytical expressions derived on Secs. 4.3 and 4.4. We study how interference and diffraction effects can be observed in conical topology which can have potential applications in the detection of cosmic strings by gravitational lensing. The plots provided in this section for plane wave incidence may be compared to those obtained by Suyama et al. [83]. We see that they are indeed very similar but, with our approach, we have been able to explain how the wave patterns are formed.

4.5.1 Study of the line of sight

Plane wave

Let us analyse the particular case when the string is on the observer-source line of sight ($\theta = 0$). We begin with the simpler case of plane wave incidence. Due to the symmetry, the contributions from both sides are equal, thus the wave field (4.36) normalized to the unlensed value E_0 is determined only by one parameter N,

$$\left(\frac{E}{E_0}\right)_{\theta=0} = 2\mathrm{e}^{-\mathrm{i}\pi N}\mathcal{F}(\sqrt{\pi N}), \tag{4.51}$$

with

$$N = \frac{kr}{\pi}(1-\cos\Delta), \tag{4.52}$$

which is the number of half-wavelengths matched in the path difference between the GO and D waves [it corresponds to the index $j + 3/4$ of Eq. (4.50)]. In the limit of $\Delta \ll 1$ it reduces to $N \approx r\Delta^2/\lambda$. For the amplification factor we obtain

$$F|_{\theta=0} = 2|\mathcal{F}(\sqrt{\pi N})|. \tag{4.53}$$

The factor of 2 corresponds to the characteristic appearance of double images of equal brightness in the cosmic string spacetime when the observer is on the line of sight or nearby [98, 146]. The amplification factor (4.53) as a function of the dimensionless parameter N is plotted in Fig. 4.14. We see the oscillating pattern similar to that for the straight-edge diffraction [78, 123], but with some differences: for the diffraction by the string, the shadow part of the curve is missing and the magnitude is doubled. The whole range of values of the field can be visualized by means of the Cornu spiral [Fig. 4.14(b)]. Here, the real and imaginary part of the wave field (4.51) are depicted for different values of N. (We omit the phase factor $\mathrm{e}^{-\mathrm{i}\pi N}$ which does not contribute to the absolute value.) In the figure, the length of the cord between the origin and any point of the spiral is precisely the amplification factor F and the length of the Cornu curve between the end point a ($N = 0$) and one on the spiral is $\sqrt{\pi N}$. So, the spiral represents a mapping of real N-axis on the complex $\mathcal{F}$-plane. As $N \to \infty$, both the amplification factor in Fig. 4.14(a) and the spiral approach the value of 2, the limiting GO value. Note that the observed pattern can only be explained when the D waves are taken into account. Some illustrative points in Fig. 4.14 have been highlighted. A simpler expression for the amplification factor can be obtained by means of the GTD:

$$F|_{\theta=0} \approx 2\left[1 + \frac{1}{\pi\sqrt{N}}\cos\left(\pi N - \frac{3\pi}{4}\right)\right]^{1/2}. \tag{4.54}$$

The comparison of the full wave (4.51) and asymptotic (4.54) expressions in Fig. 4.14(a) indicates little difference, which becomes negligible for $N \gtrsim 2$. Note that, as predicted in Sec. 4.4.3, the

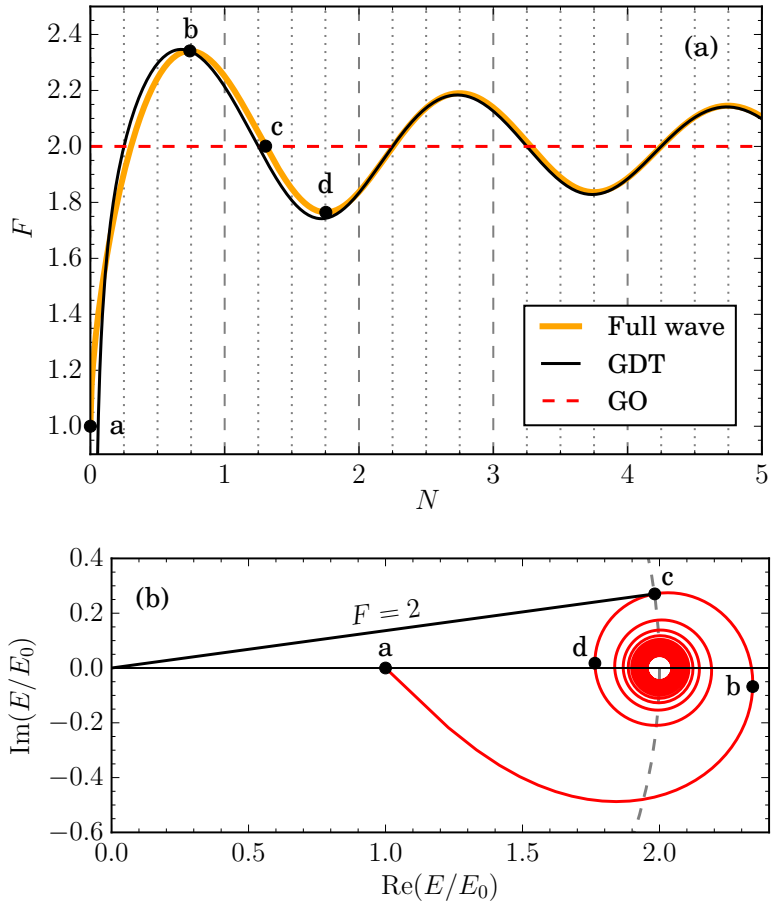

Figure 4.14: (a) Amplification factor and (b) Cornu spiral for the case when the string is on the line of sight. Equivalent points on the two figures are labelled. On (b), the cross points of the circular arc (grey dashes) with the Cornu spiral correspond to $F = 2$, the GO value.

maxima and minima of diffraction are located at

$$N = \frac{3}{4} + n \quad \text{with} \quad \begin{array}{ll} n = 0, 2, 4 \ldots & \text{maxima,} \\ n = 1, 3, 5 \ldots & \text{minima.} \end{array} \tag{4.55}$$

The highest maximum occurs at $N_1 \approx 3/4$ giving the field $F \approx 2[1 + 2/(\pi\sqrt{3})]^{1/2} \approx 2.34$ (point b in Fig. 4.14). This value corresponds to an intensity $I_{\max} = F^2_{\max} \approx 5.47$.

Line source

We can now continue with the case of the line source. The zone structure we have introduced by simple analysis of four-wave interference is based on the GTD prescribed by Eq. (4.21). Despite its asymptotic character, this theory is known to fit almost perfectly the exact solution in diffraction experiments on obstacles as small as two wavelengths, with good predictions down to one wavelength (see, e.g. Ref. [163]). We therefore believe that one can predict the location of the diffraction maxima due to wave scattering on the cosmic string with very high accuracy by the simple procedure described in Sec. 4.4.3. For instance, to find the maximum (n, m) corresponding to the zone $\mathcal{Z}_{nm}$, all we need is to calculate the crossing point of the two hyperbolas given by Eq. (4.45) with $j = n$ and $j = m$ for the two sources, respectively. This determines at which distance r and angle θ from the string a maximum intensity or saddle point should appear. To

confirm our findings, in Fig. 4.15 we plot the amplification factor $F = |E/E_0|$ calculated from the UAT expression (4.32) – which is more accurate than the geometrical theory of diffraction – when the string is on the line of sight ($\theta = 0$). The intersection points of the hyperbolas, (n, m), are superimposed and they are seen to coincide precisely with the maxima and minima of the oscillations in the central antinodal line.

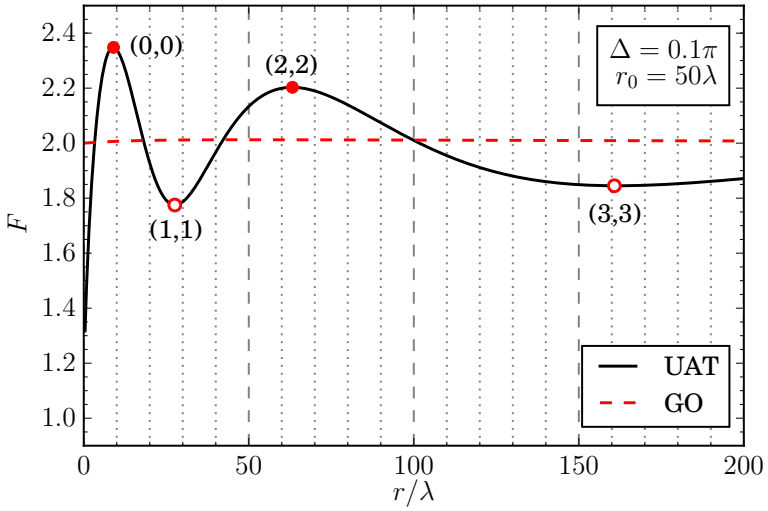

Figure 4.15: Amplification factor F as a function of the distance r when the string is on the line of sight (central antinodal line). Intersection points of the hyperbolas (4.45) determining maxima and minima are labelled.

As seen for plane-wave incidence, the symmetry of this case allows us to write the field in a more compact form. Indeed, the GO paths from the two sources to the observer are equal, $s^- = s^+ \equiv s$. Therefore, the path difference between the GO and D waves is also identical for both sources and equal to $r + r_0 - s$. From the UAT expression (4.32) we obtain the amplification factor at $\theta = 0$ in the form

$$F|_{\theta=0} = \left| 2\sqrt{\gamma}\, \mathrm{e}^{-\mathrm{i}\psi} \mathcal{F}(\sqrt{\psi}) + \frac{\mathrm{e}^{\mathrm{i}\pi/4}}{\sqrt{\pi\psi}} \left(\sqrt{\gamma} - \sqrt{\frac{2\gamma}{\gamma+1}} \right) \right|, \tag{4.56}$$

which is now a function of two parameters (instead of just one as for the infinitely distant source): $\gamma \equiv (r + r_0)/s$ and $\psi \equiv k(r + r_0 - s)$. Taking into account that $0 \leq \Delta \leq \pi/2$, it can be seen that γ only ranges from 1 to $\sqrt{2}$. In the plane-wave limit, $r_0 \to \infty$, one gets $\gamma \to 1$ and recovers our previous result (4.53) with $\psi = \pi N$. A simpler formula can be obtained by using the expansion of the Fresnel integral (4.27). In that way we obtain

$$F|_{\theta=0} \approx 2\sqrt{\gamma} \left[1 - \frac{\sqrt{2}}{\sqrt{\pi\psi(\gamma+1)}} \cos\left(\psi + \frac{\pi}{4} \right) \right]^{1/2}, \tag{4.57}$$

which is similar to the case of a plane-wave diffraction (4.54), but now the function oscillates around the new GO value $F_{\mathrm{GO}}|_{\theta=0} = 2\sqrt{\gamma}$, that can be higher than 2.

4.5.2 Spectrum analysis

The analytical theory we have derived can be of interest in the detection of cosmological cosmic strings by means of electromagnetic or gravitational waves. Consider the situation when the source, string, and observer occupy fixed positions. In this case the diffraction pattern can

still in principle be observed in the energy (frequency) spectrum of the detected signal, since interference and diffraction are wavelength dependent. Several authors pointed out on such a possibility when they studied the interference effects in gravitational lensing by compact objects (see, e.g. [164, 165]). What one would expect is a characteristic intensity modulation over the frequency spectrum that could allow to identify the object. However, if the gravitational lens moves, the path-length differences will change with time, and the intensity oscillations (the maxima and the nodes) will move across the spectrum [164,165]. Let us analyse in the frequency domain the results we have obtained for the diffraction by a cosmic string in the case of an infinitely distant source.

Depending on the angular position θ of the observer, different kinds of patterns can be distinguished, as shown in Fig. 4.16, where the full-wave amplification factor [i.e. using Eq. (4.36)] is plotted as a function of the frequency ω. We normalize the frequency for convenience by the value $\omega^* = \pi/[r(1-\cos\Delta)]$. In this way, the same plots are applicable when the coordinate r of the observer is varied. From the observational point of view, one can obtain information about

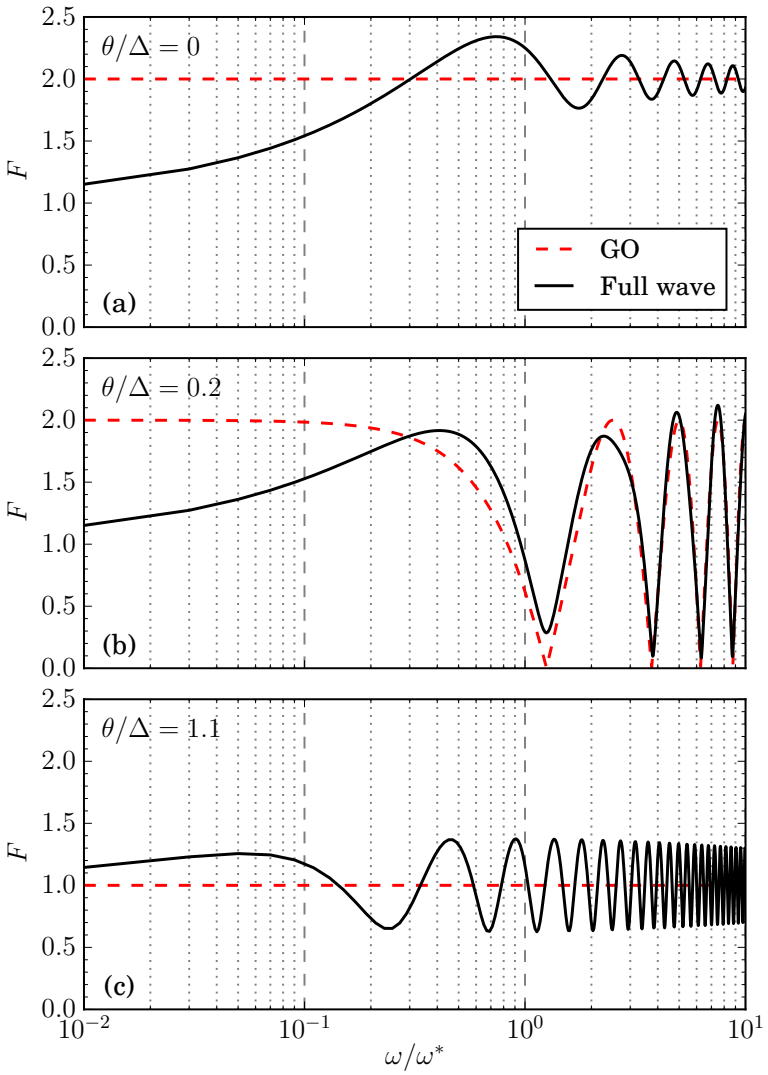

Figure 4.16: Full-wave amplification factor and its geometrical-optics limit as a function of the frequency ω for three different angular positions θ of the observer: (a) line of sight; (b) double-imaging region, off line-of-sight; (c) single-imaging region. Plane-wave incidence on a cosmic string with $\Delta \ll 1$ is assumed. The normalization frequency is $\omega^* \approx 2\pi/(r\Delta^2)$.

the string's parameters by matching the frequency pattern of the detected signal with one of the plots corresponding to the different alignments and finding the characteristic ω^*. In the realistic limit $\Delta \ll 1$, this frequency is simply $\omega^* \approx 2\pi c/(r\Delta^2)$ and the full-wave amplification factor for $\theta \ll 1$ can be written as

$$F = \left| \mathrm{e}^{-\mathrm{i}\phi} \mathcal{F}\left[\sqrt{\frac{\omega}{\omega^*}\pi}\left(1+\frac{\theta}{\Delta}\right)\right] + \mathrm{e}^{\mathrm{i}\phi} \mathcal{F}\left[\sqrt{\frac{\omega}{\omega^*}\pi}\left(1-\frac{\theta}{\Delta}\right)\right]\right| \tag{4.58}$$

with $\phi = (2\pi\omega/\omega^*)(\theta/\Delta)$. We can see from this expression that the only determining geometrical parameter is θ/Δ.

Another distinctive feature is the magnitude of the amplification. The case of most interest is when the source, the string and the observer are all aligned ($\theta = 0$). Given that the observer is on the central antinodal line and the interference between two GO waves is constructive for any ω, the amplification factor in this case oscillates around the value $F_{\mathrm{GO}} = 2$, approaching it as the frequency increases [Fig. 4.16(a)]. The oscillations are due to the interference between the GO and D waves, meaning that diffraction can increase the amplification to values higher than 2. When the string is off the line-of-sight, but the observer is still in the double-imaging region ($-\Delta < \theta < \Delta$), the oscillations become more profound ranging approximately between 0 and 2 [see Fig. 4.16(b)]. They appear due to more complex four-wave interference involving two GO and two D waves. Notice that the variation in frequency when the observation point is fixed is in some sense equivalent to the change in the distance r with fixed θ and ω. For the latter, the oscillations correspond to crossing the nodal and antinodal lines when r increases [see Fig. 4.12(c),(d) or Fig. 4.13]. Finally, for the single-imaging region ($|\theta| > \Delta$) one of the sources is shadowed and F oscillates around $F_{\mathrm{GO}} = 1$. These oscillations are due to interference of one GO wave and two D waves [Fig. 4.16(c)]. We can also confirm from the wave patterns plotted in Fig. 4.16 that even if some wave effects can be observed with just the GO terms [166], diffraction adds important features to the observed wave field.

4.6 Comparison of numerical simulation with analytical theory

To solve numerically the wave equation (2.18), we use a rectangular 2D geometry of (x, y) space as shown in Fig. 4.17. We consider a 2D wave produced by a point source on the left boundary at a distance r_0 from the string S. The source is an electric line current perpendicular to the domain which generates TE-polarized cylindrical waves. The wave equation is solved for the electric field E. The distances are normalized by the wavelength λ, which makes the wave equation independent of the frequency. Therefore, it can be solved for any wavelength as long as it is larger than the unit cells of the metamaterial and within its operating bandwidth [7]. The same value for the source-string distance $r_0 = 10\lambda$ is used for all the simulations presented in this section (for other parameters see App. C). The numerical simulation was carried out by using the COMSOL Multiphysics software package and the resulting data was processed in Python.

In Fig. 4.18 we show typical results of our simulation for the electric field E in a medium which mimics the cosmic string topology. One can see that the emitted wave propagating around the string interferes with itself giving rise to a characteristic pattern. This self-interference is caused by the conical curvature (singularity) at the string location. The wavefronts of the emitted cylindrical wave are affected by this effect as depicted in Fig. 4.18(a). By plotting the squared electric field norm in Fig. 4.18(b), we can also see that the wave field is amplified in some areas behind the string due to the interference and diffraction effects explained in Sec. 4.4.3. It is interesting to compare these figures with those for the diffraction by a single half plane shown

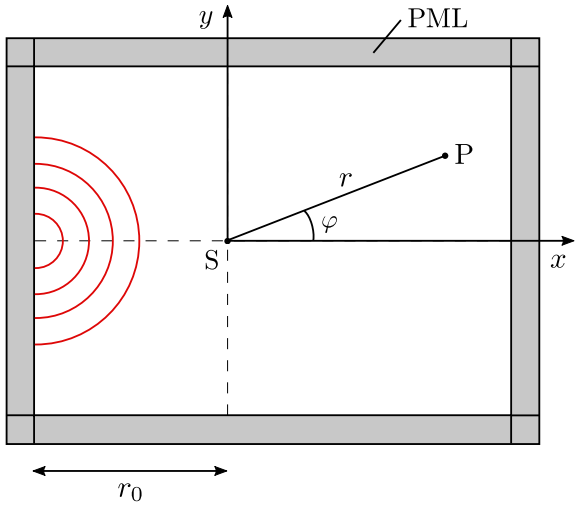

Figure 4.17: Diagram of the geometry for the numerical simulation of wave propagation in a metamaterial mimicking a cosmic string. The wave source is located at a distance r_0 from the string S. The domain is surrounded by a perfectly matched layer (PML) that absorbs the outward waves to ensure that there are no unwanted reflections.

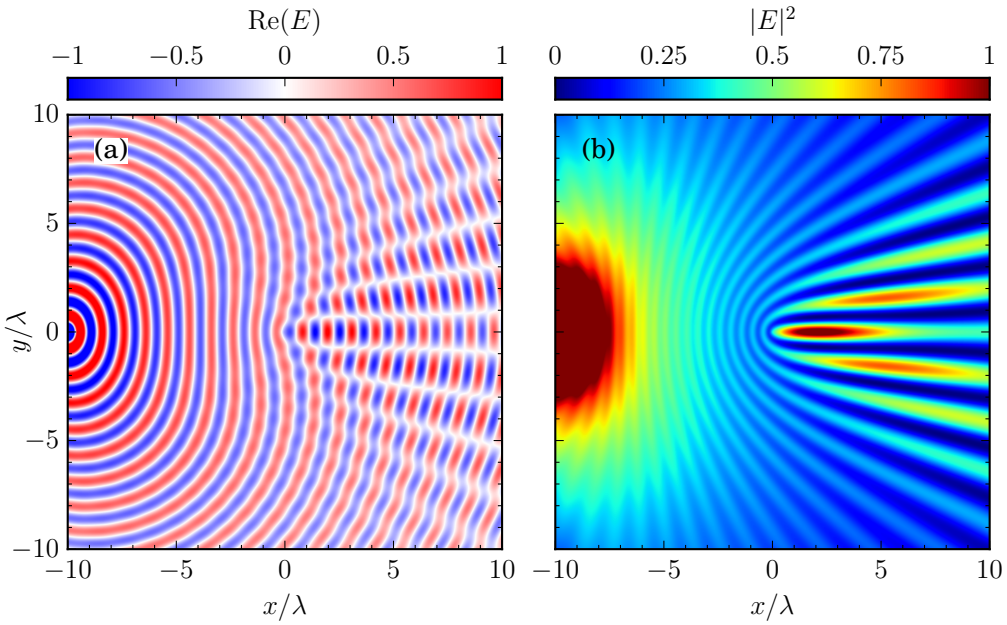

Figure 4.18: Spatial distributions of the (a) real part of the electric field Re(E) and (b) squared norm $|E|^2$ (in arbitrary units) for a medium mimicking the cosmic string topology. The source is located at $r_0 = 10\lambda$ and the deficit angle is $\Delta = \pi/5$.

in App. B. For instance, we can already see that for the string there is no region of complete shadow.

The main interference pattern observed in the numerics can be explained by the nodal and antinodal lines. To see that, we present Fig. 4.19 where we superimpose these lines – given by Eq. (4.42) – to the simulated amplification factor $F = |E/E_0|$ for two values of the deficit angle Δ. A good agreement is observed within the double-imaging region. The lines of field amplification (seen in red in Fig. 4.19) are seen to precisely coincide with the dashed antinodal lines, whereas the nodal lines match the blue regions of field decrease. However, one cannot

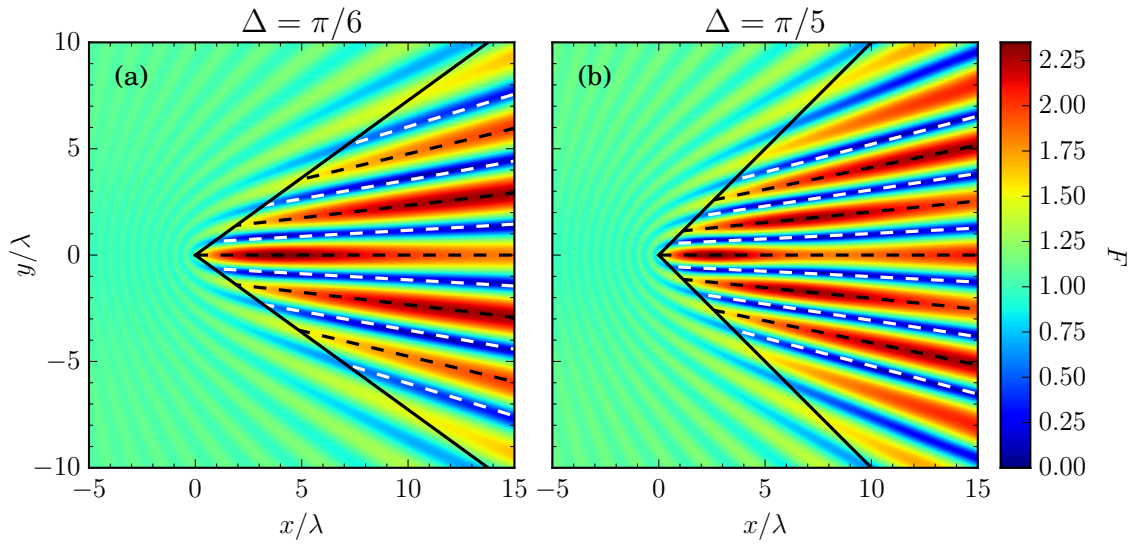

Figure 4.19: Wave pattern for the amplification factor F obtained from numerical simulations in a medium with (a) $\Delta = \pi/6$ and (b) $\Delta = \pi/5$. The nodal and antinodal lines are superimposed in white and black dashed lines, respectively. Solid black lines are the boundaries of the double-imaging region.

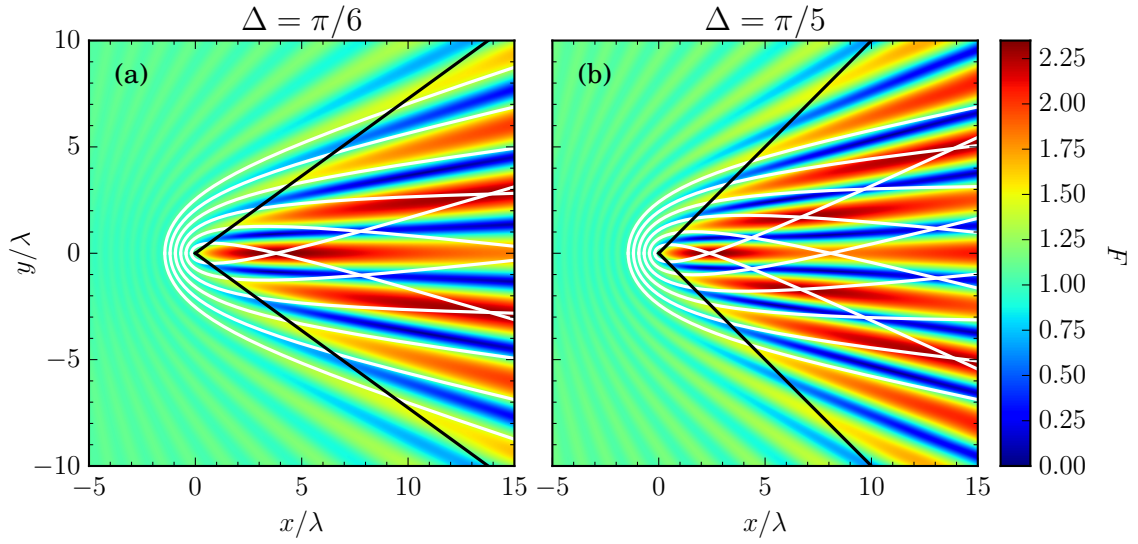

Figure 4.20: Wave pattern for the amplification factor F obtained from numerical simulation for (a) $\Delta = \pi/6$ and (b) $\Delta = \pi/5$. The lines of constant phase between the GO and D waves (superimposed in white) determine the diffraction maxima. Solid black lines are the boundaries of the double-imaging region.

explain the interference pattern outside that region and the variation of the intensity over the antinodal lines within the GO approximation. Therefore, the interference with the D waves must be taken into account by means of the hyperbolas of Eqs. (4.43) and (4.44). In Fig. 4.20 these lines are plotted over the numerical wave pattern. As explained in Sec. 4.4.3, whenever the indices n and m of the hyperbolas are even, their intersection lies precisely on the wave field maxima. Odd n and m correspond to saddle points (local minima on antinodal lines). Moreover, as we expected, in the nodal lines the dominating effect is the destructive interference of the GO waves and the D waves do not affect the wave field significantly. (Figures 4.19 and 4.20 can

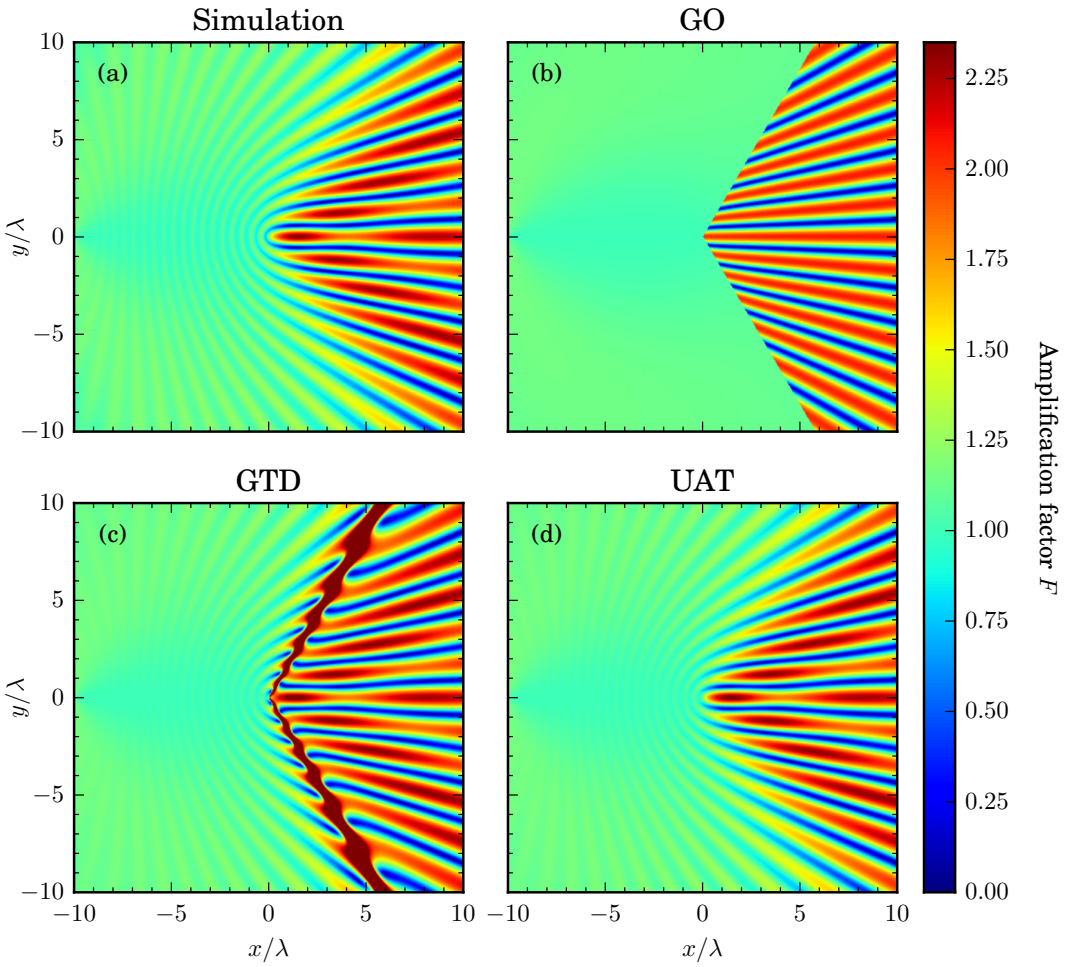

Figure 4.21: Comparison of the wave patterns obtained from: (a) metamaterial simulation, (b) geometrical optics, (c) geometrical theory of diffraction, and (d) uniform asymptotic theory; for a medium with $\Delta = \pi/4$.

be compared with 4.12(b).) A good agreement is seen between the predicted positions and the numerical results. This means that (i) the metamaterial medium reproduces the wave effects expected in the cosmic string spacetime; and (ii) the observed wave pattern can be explained in terms of interference of the two GO and two D waves.

The numerical results for another value of the deficit angle $\Delta = \pi/4$ are shown in Fig. 4.21 in comparison with all the analytical theories discussed in Sec. 4.3. This figure allows to compare all types of approximations in one view and observe the corrections that each one provides. With the GO approximation [Fig. 4.21(b)] one can already observe the main interference effects (the fringes corresponding to the nodal and antinodal lines) in the double-imaging region. Nevertheless, there is an abrupt change of the field at the boundary between the single- and double-imaging zones with no wave effects in the former. The wave pattern is substantially improved by using the diffraction terms in the GTD [Fig. 4.21(c)], which also add some modulation in the antinodal lines. It is seen that the wave effects behind the string are very well reproduced except at the boundary of the double-imaging region, where the diffraction terms diverge. Lastly, the UAT [Fig. 4.21(d)] provides a smooth transition between the single- and double-imaging regions, having the least discrepancy with the numerics in the entire domain[6]. How small the discrepancy is, one can appreciate from 1D plots of Fig. 4.22, where the amplification F is shown as a function

[6]We have also noted that the penumbra terms in equation (4.32) are dominant due to small values of $\tilde{D}$.

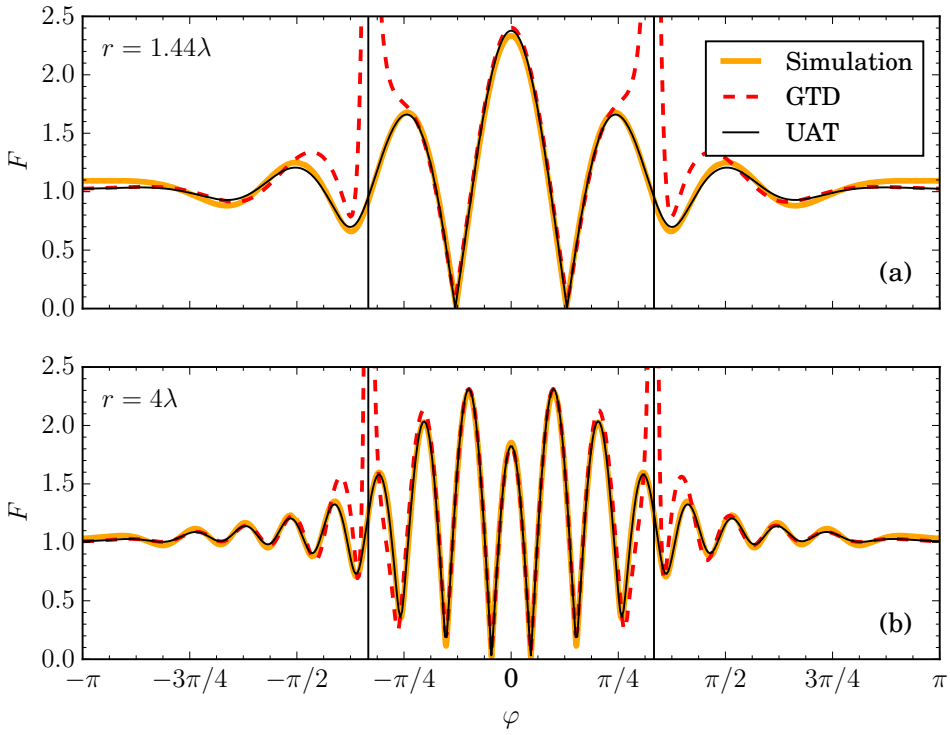

Figure 4.22: Comparison of 1D plots for the amplification factor F of figures 4.21(a), 4.21(c) and 4.21(d). F is shown as a function of the angle φ for two fixed distances between the string and the observation point: (a) $r = 1.44\lambda$, corresponding to the highest diffraction maximum $(0, 0)$, and (b) $r = 4\lambda$. Vertical black lines define the boundaries of the double-imaging region.

of φ for two fixed distances r. One can see that the agreement between the metamaterial simulation and the UAT formula (4.32) is not only qualitative but also quantitative. There is only little discrepancy in the surroundings of the source given that we assumed $w^{\pm} \gg 1$ in our derivations. We also plot the GTD (4.21) and confirm that it is indeed a very good approximation except near the boundary of the double-imaging region. Note that the double-imaging effect results in the field amplification behind the string and, due to diffraction, the factor $F = |E/E_0|$ can even be greater than 2.

For completeness, we also provide the density plots of the electric field, $\mathrm{Re}(E)$ and $|E|^2$, in Figs. 4.23 and 4.24, respectively, for the same parameters of Fig. 4.21. With these representations, we can see how the different analytical theories shape the wavefronts or how the field intensity is distributed. Note that in the double-imaging region boundary of the GTD [Figs. 4.23(c) and 4.24(c)] the phase shift of π of the D waves can be clearly seen, as given by the diffraction coefficients (4.22).

In App. C we provide the numerical simulations for a wider range of parameters r_0 and Δ. In this way, we show how their variation affects the resulting wave pattern. Moreover, we also simulate the propagation of a Gaussian beam and compare the results to the null-geodesics in the cosmic string spacetime (as done in the previous chapter for the Schwarzschild black hole).

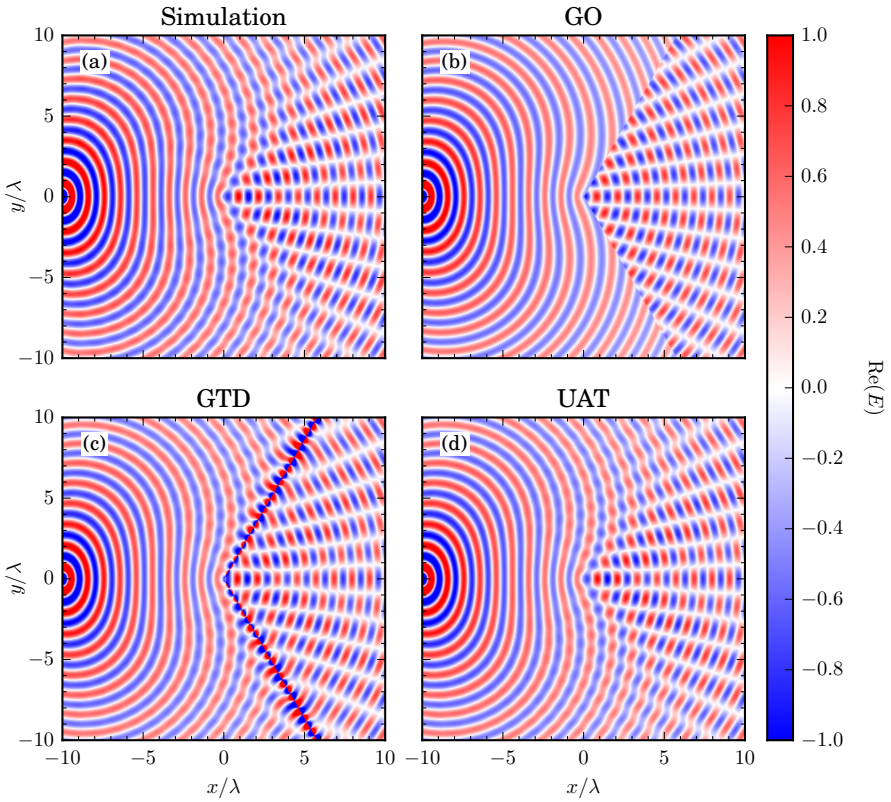

Figure 4.23: Real part of the electric field Re(E) for $\Delta = \pi/4$, given in arbitrary units.

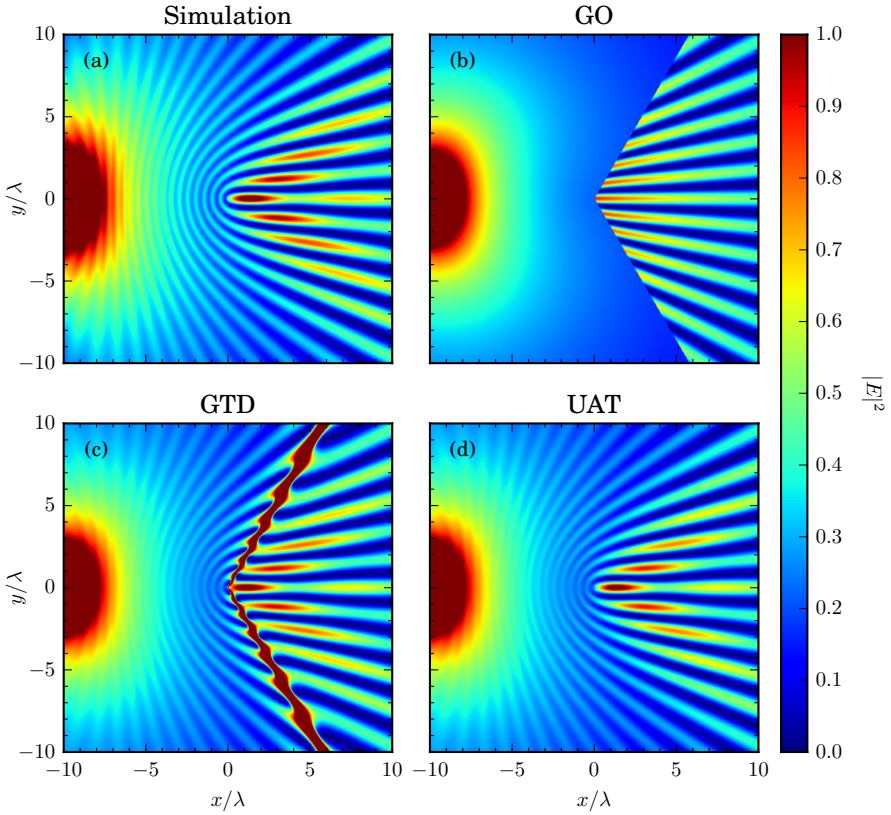

Figure 4.24: Electric field norm $|E|^2$ for $\Delta = \pi/4$, given in arbitrary units.

4.7 Conclusions and outlook

The work of this chapter can be divided into two main parts. On the one hand, we have derived the medium parameters of effective media that mimic the conical topology of a static cosmic string by means of transformation optics. We have numerically solved the wave equation in the material to study the propagation of electromagnetic waves. On the other hand, we have presented analytical models that describe the propagation of scalar waves emitted by a source at a finite and infinite distance from a linear topological defect with conical curvature. We have used asymptotic theories of diffraction which, thus far, have been essentially applied to obstacles with clearly defined boundaries (such as a half-plane or a slit [81]). Here, we have applied them to a topological defect and obtained an excellent agreement with the numerical results of the metamaterial simulation. The use of asymptotic theories presents advantages over other methods used in the literature. The existing solutions for similar problems in the form of integral representation [82] or infinite series [83] exclude the rigorous physical analysis necessary for practical applications. The infinite series solution, for instance, is poorly convergent for distances greater than about a wavelength. These limitations are overcome by the GTD and UAT since they capture the main physics (offering a simple way to interpret the wave effects) and only a few terms are needed to achieve the required accuracy.

One of the distinctive features of the cosmic string spacetime is the emergence of two image sources. At first sight, their mutual interference may look like a familiar Young's double-slit interference experiment Our results, however, indicate that the two models are conceptually different. Young's double-slit setting has a characteristic length – the distance between the slits d, that implies that the interference fringe scales as $\sim \lambda r/d$ [123]. On the contrary, for the conical space, there is no characteristic length but a characteristic angle Δ. As a result, the interference and diffraction effects manifest differently from those in Young's experiment. For instance, we have seen that for plane wave incidence the fringe separation in conical space does not scale with the distance to the string, being $\sim \lambda/(2\beta \sin\Delta)$. In the case of diffraction by a physical object such a slit or a thin wire, the wave pattern occurs near the shadow lines [78, 123] (see the case of the half-plane screen in App. B) but for the linear topological defect there is no shadow at all. Interference effects are due to the localized curvature of the cosmic string spacetime.

We have also shown that the wave effects – interference and diffraction – are of importance and could be used in cosmological observations to identify the string from other cosmological gravitational lenses. For a two-dimensional geometry, we have defined the Fresnel observation zones $\mathcal{Z}_{nm}$ bounded by conic sections: hyperbolas when a source is at finite distance, and parabolas for an infinitely distant source. Our theory allows to predict the location of the diffraction maxima, which are characteristic points of interference between the GO and D waves, corresponding to a specific observation zone. We have contrasted these points with the numerical simulation in the equivalent metamaterial and found very good agreement. Additionally, one can obtain information about the string by matching the frequency pattern of the detected signal with theoretical plots corresponding to different alignments. Taking the typical value $\Delta \sim 10^{-7}$ and a distance to the string within our galaxy, $r \sim 10^{20}\,\mathrm{m}$, one obtains the typical frequency $f^* \sim 100\,\mathrm{Hz}$, which is in LIGO's frequency band [167]. For larger distances, $r \sim 10^{26}\,\mathrm{m}$, the frequency will be of the order $f^* \sim 10^{-4}\,\mathrm{Hz}$, which is within the sensitive frequency range of the Laser Interferometer Space Antenna (LISA) [168]. Therefore, we hope that future observations of gravitational waves in the coming years could confirm the existence of these objects. In the above discussion, it was assumed a static configuration of the lens system. If the string moves with respect to the observer-source line of sight, one would expect the wave amplification to be modulated in time at the observer's position with a time scale $\sim r\Delta$. If the string moves with a relativistic velocity [66], one obtains the time scale of the order of a week for the string moving at a dis-

tance $r \sim 10^{21}$ m. On the other hand, the diffraction pattern will move across the frequency spectrum [164, 165]. The latter effect will probably be more difficult to observe, since limited information on the whole spectrum could be collected during the sweep time.

The equivalent medium needed to mimic the cosmic string spacetime in the laboratory should be a 2D anisotropic metamaterial, however, only one type of anisotropy is needed (either magnetic or electric, as explained in Sec. 2.4.2). Moreover, by rescaling the electric field we have seen that either the permittivity or permeability can be that of empty space [see Eq. (4.6)]. Since the medium parameters for the conical curvature are independent of the length scale (see Fig. 4.2), the easiest way to accomplish this task might be to assemble a large-scaled structure to use for microwave radiation. Another possibility to mimic a conical topology is to use the transformation to Minkowskian geometry with a limitation on the angle. To do that, one should design a wedge in empty space (i.e. $\varepsilon = \mu = 1$) with two identical sources located on the faces, as depicted in Fig. 4.5(b). In this way, the task to create a complex anisotropic medium is transformed to the task to arrange the appropriate (Neumann) boundary conditions for the field on the faces of the wedge and to synchronize the wave sources.

Conical topology presents peculiar features that can open up new opportunities for applications in photonics and other fields. For instance, metamaterials with conical singularities can act as omnidirectional beam-steering devices [52], beam-splitters [52, 85], diffraction-control elements [53], retroreflectors [169], etc. Our results can also potentially be applied to light [75, 152] or sound propagation [74, 77] near a linear topological defect in nematic liquid crystals. It would also be interesting to extend our approach involving the asymptotic diffraction theories to other geometries or types of topological defects. If the medium anisotropy can be transformed away by mapping from physical to virtual space, the problem of wave propagation in a complex material may be reduced to the diffraction on simple shapes with the appropriate boundary conditions, as in the case of the cosmic string. Then, the asymptotic theories, like GTD or UAT, can be applied to obtain the analytical results.

CHAPTER 5

Conclusions and perspectives

In a material medium, light propagation is determined by the permittivity and permeability. In vacuum, light is affected by spacetime curvature. These two phenomena are seen to be analogous in the context of transformation optics, which relates the two mathematically. Owing to the great developments in metamaterial science during the past decades, experiments based on the analogy between media and geometry are realizable in the laboratory. This possibility offers the chance to study gravitational systems in a controlled environment. For instance, one might be able to change certain cosmological parameters such as the small deficit angle of a cosmic string to a larger value to enhance some effects that might be difficult to observe otherwise.

In this thesis, we have used Plebanski's parametrization of the electromagnetic constitutive equations to derive the medium parameters of metamaterials analogous to two types of static cosmological objects with different symmetries and properties. On the one hand, we have studied a spherically symmetric spacetime and applied the obtained expressions to the case of the Schwarzschild black hole. By comparing the numerical simulations of wave propagation in the analogous metamaterial with the null-geodesics, we have verified that the behaviour of light in these two systems is indeed equivalent. We have also derived the optical Hamiltonian under the eikonal approximation and found it to be identical to the one derived in the context of general relativity. We believe that the good agreement of our results may help illustrate and understand why transformation optics can be a useful tool to transfer concepts from celestial mechanics to photonics and vice versa.

On the other hand, we have also studied the cosmic string spacetime, that is, a linear topological defect with conical geometry. We have simulated wave propagation in the equivalent metamaterial as well, but in this case we have also derived analytical models based on diffraction theories applied to half-plane screens. With our method, the wave effects observed in the numerical simulations can be understood as the interference of four characteristic waves and reproduced accurately with analytical expressions. Moreover, the diffraction pattern of the cosmic string has been obtained, which can be of interest in the detection of strings by gravitational lensing (of electromagnetic or gravitational waves). The possibility to detect previously invisible objects such as cosmic strings by means of gravitational waves seemed infeasible some years ago, but fortunately, LIGO's groundbreaking observation of binary black holes merging opened up a new way to *look* at the sky. We are hopeful of the potential this tool holds for the future of exploring our universe.

It is interesting to see how intrinsically different the two studied objects are. For instance, the black hole metric is asymptotically flat. Therefore, when light is far from the event horizon, it

is barely affected by the spacetime curvature. In the metamaterial, this manifests as medium parameters asymptotically equal to those of vacuum, $\varepsilon = \mu = 1$. Contrarily, the conical topology of the cosmic string presents a curvature singularity at $r = 0$ that affects wave propagation in the whole space, making light always deflect the same angle. The medium presents the same singularity; the permittivity and permeability do not scale with the radial distance, they are only a function of the angular coordinate. This also contrasts with the possibility of modelling a spherically symmetric spacetime with an isotropic metamaterial characterized by an inhomogeneous refractive index $n(r)$, which would not be possible for the topological defect.

As seen for the geometries considered in this thesis, analogue gravity with metamaterials (whether it is in the form of numerical simulations or experimental realization) provides an interesting support to the study of their gravitational counterparts. For example, one can investigate wave scattering or changes in polarization in a curved spacetime in a controlled way. In addition, certain well-known properties of the systems we have studied have inspired the design proposal of several photonic devices. The capture of light by a black hole has been mimicked by omnidirectional broadband absorbers. The fact that the deflection angle in conical topology is independent of the impact parameter might be used to design beam-steering devices that always make the incident beam deviate in the same way. Furthermore, the same metamaterial can also play the role of a beam-splitter in the case of zero impact parameter. In the future, devices such as these may have important applications in optical set-ups fulfilling their different functions and in the case of the optical black hole, in photovoltaic systems as well. All this encourages us to believe that metamaterials based on other cosmological objects can also find novel and unexpected uses in photonics.

This thesis has covered diverse topics from electromagnetic waves in anisotropic media to the lensing of gravitational waves. We hope the different elements of the work can be of interest to their corresponding research fields but also foster the transfer of ideas between them.

APPENDIX A

Schwarzschild modelling with alternative medium parameters

In Sec. 3.3 we have noted that the wave equation in the eikonal approximation (3.16) is not changed by the redefinition of the medium parameters: $\tilde{\mu}_\varphi = \mu_\varphi \varepsilon_z$, $\tilde{\mu}_r = \mu_r \varepsilon_z$ and $\tilde{\varepsilon} = 1$. Indeed, the Hamiltonian (3.20) can be multiplied by an arbitrary function of the coordinates without affecting the ray trajectories. Nevertheless, the full wave equation (3.15) cannot be rescaled in this way without affecting the resulting wave pattern. To see how different that would be, the simulation in the renormalized medium for the Schwarzschild metric can be carried out. For this case, the new material parameters are given by

$$\tilde{\varepsilon}^{ij} = \delta^{ij}, \tag{A.1}$$

$$\tilde{\mu}^{ij} = \frac{1}{\left(1 - \frac{\mathrm{r_s}}{r}\right)^2}\left(\delta^{ij} - \frac{x^i x^j}{r^3}\mathrm{r_s}\right), \text{ for } i,j = x,y \tag{A.2}$$

$$\tilde{\mu}^{zz} = 1, \tag{A.3}$$

$$\tilde{\mu}^{xz} = \tilde{\mu}^{yz} = 0. \tag{A.4}$$

In this way, the permittivity becomes isotropic while the anisotropy of permeability is confined to the x and y components. Therefore, this could be implemented in a two-dimensional metamaterial device. As done in Sec. 3.5, we solve the wave equation (2.18) in the medium with the renormalized parameters for a TE-polarized wave with a Gaussian profile injected from the right boundary of the simulation domain (see Fig. 3.3). Note that this redefinition of the permittivity and permeability does not affect the anisotropy angle α, being given by Eq. (3.9). The numerical results for different impact parameters are shown in Fig. A.1. These results should be compared to those of Fig. 3.4. The first difference is that, due to the rescaling, the medium parameters increase faster as they approach the core. A high refractive index (or permeability, in this case) means that light is slow. This can give points or regions where light concentrates. To avoid singularities of the field, we use a larger absorbing core of radius $\mathrm{r_s} + \delta$ with $\delta = 0.25\mathrm{r_s}$. We see that the Gaussian beams in Figs. 3.4 and A.1 follow very similar trajectories but the ripples and sub-beams differ, as we expected. We notice wider beams and higher concentration of the field near the absorber for the cases of capture by the black hole [Figs. A.1(a),(b)]. In the critical case of Fig. A.1(c) this allows us to clearly see that part of the beam is attracted to the core. The high values of the field near the absorber are partly due to the rapid increase of the permeability (A.2) but the change in the geometry (that is, the larger radius of the core) possibly affects the field distribution as well.

Finally, we would like to remind that the case of electric anisotropy can be easily modelled by solving the wave equation (2.18) for the magnetic field H considering a TM-polarized wave and changing $\tilde{\varepsilon}^{ij} \leftrightarrows \tilde{\mu}^{ij}$.

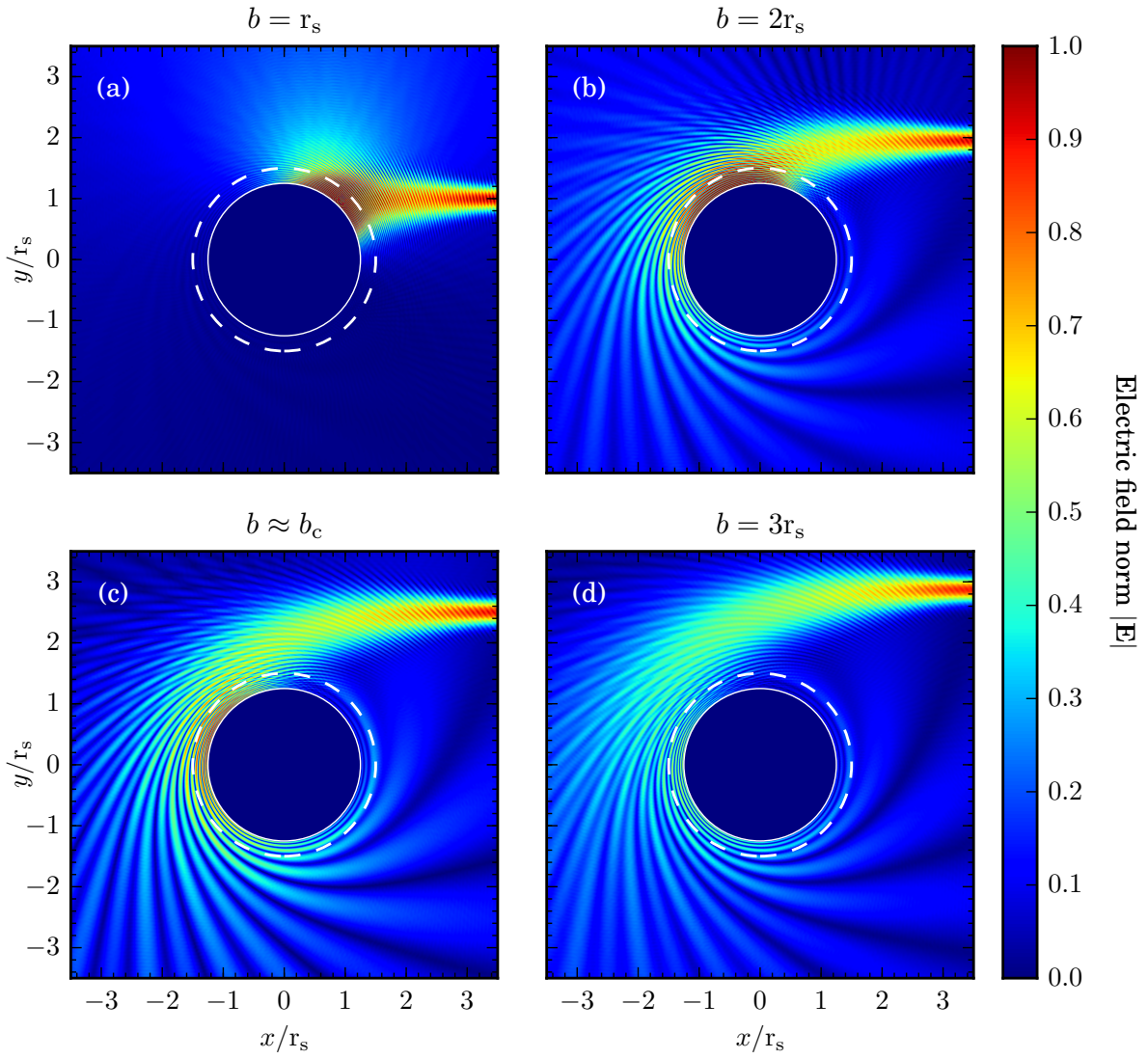

Figure A.1: Simulation of a TE Gaussian beam of wavelength $\lambda = 0.15\mathrm{r_s}$ and waist radius $w_0 = 0.2\mathrm{r_s}$ in a metamaterial with parameters (A.1)-(A.4) mimicking the Schwarzschild spacetime for different impact parameters: (a) $b = \mathrm{r_s}$, (b) $b = 2\mathrm{r_s}$, (c) $b \approx b_\mathrm{c}$ (slightly above), and (d) $b = 3\mathrm{r_s}$. The absorbing core and the photon sphere of radius $3\mathrm{r_s}/2$ are depicted by white circles. The electric field norm $|\mathbf{E}|$ is given in arbitrary units.

APPENDIX B

Wave diffraction by a half-plane screen

B.1 Plane wave

In Sec. 4.3 we use the representation of conical geometry as flat space with a wedge removed (see Fig. 4.4) to describe and obtain analytical expressions of wave diffraction by a cosmic string. By making this transformation, we see that we can treat this situation as the canonical problem of diffraction by a conducting half-plane screen. Through Sec. 4.3 we give the half-plane expressions we use to construct the wave field in the cosmic string spacetime In this appendix, we succinctly remember them and provide the surface plots of the half-plane field for the different models considered. This serves as a visual aid to better understand the results of the case of conical topology.

In Fig. B.1 we show the results for the case of plane wave incidence grazing the screen (according to the geometry of Fig. 4.8). In the geometrical optics limit,

$$E_{\mathrm{GO}} = \mathrm{e}^{-\mathrm{i}kr\cos\alpha}\Theta(\pi-\alpha), \tag{B.1}$$

there is only field in the illuminated region. In the whole shadow region, the electric field is exactly 0. That changes when the diffracted wave is taken into account by means of the GTD,

$$E_{\mathrm{GTD}} = \mathrm{e}^{-\mathrm{i}kr\cos\alpha}\Theta(\pi-\alpha) + \frac{\mathrm{e}^{\mathrm{i}kr}}{\sqrt{kr}}D, \tag{B.2}$$

with the diffraction coefficient D given by Eq. (4.20). Now, there is a cylindrical wave emanating from the edge of the half plane. However, the transition from the illuminated to the shadow region is discontinuous. The exact solution to this problem found by Sommerfeld [78],

$$E = \mathrm{e}^{-\mathrm{i}kr\cos\alpha}\mathcal{F}\left(\sqrt{2kr}\cos\frac{\alpha}{2}\right), \tag{B.3}$$

is continuous in the whole space, including the shadow boundary. Note that for the GTD and exact solutions of Figs. B.1(b) and (c) we see white lines in the shape of parabolas that correspond to the interference of the GO and D waves (see Sec. 4.4). We can see that this perturbs the flat shape of the GO wavefronts. The interference lines can be more clearly seen in Fig. B.1(e),(f); where the squared norm of the field is plotted.

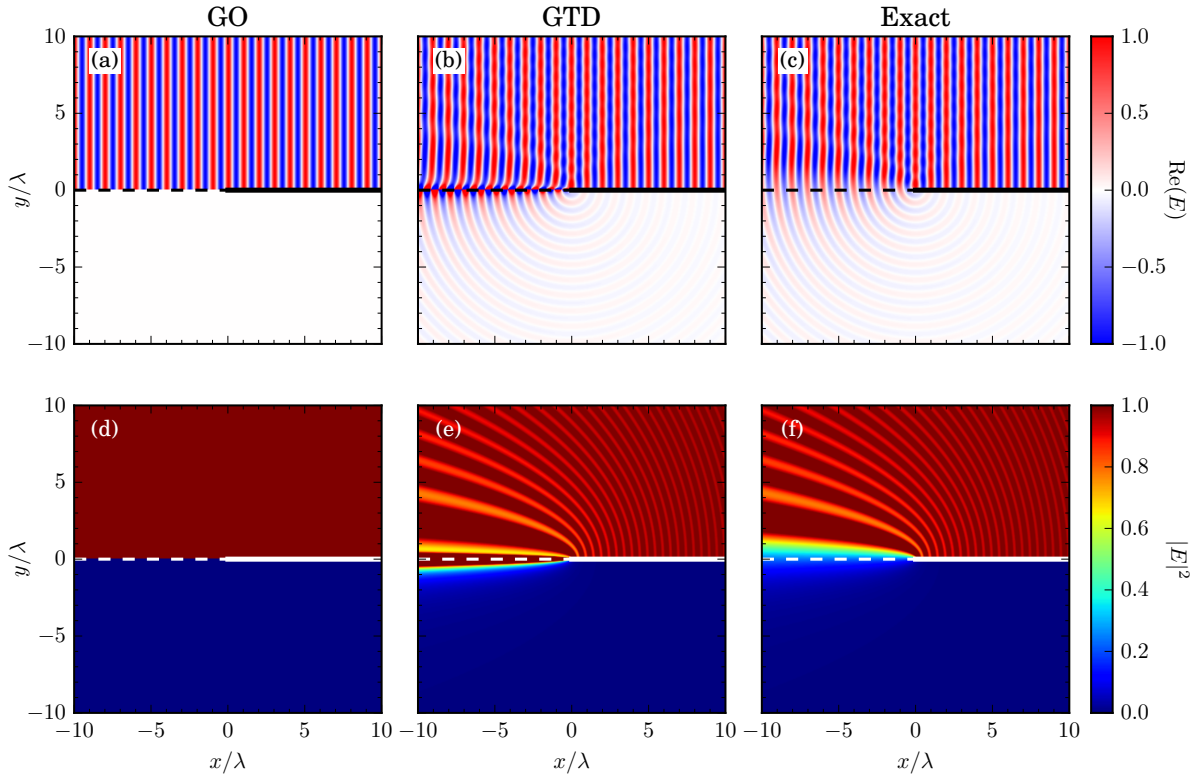

Figure B.1: (a)-(c) Real part of the electric field Re(E) and (d)-(f) squared electric field norm $|E|^2$ of a plane wave grazing on a conducting half-plane screen (denoted by a solid line) for (a),(d) the geometrical optics limit (B.1); (b),(e) geometrical theory of diffraction (B.2) and (c),(f) exact solution (B.3). The dashed line indicates the shadow boundary. The field is given in arbitrary units.

B.2 Cylindrical wave

In Figs. B.2 we consider the case of a cylindrical wave emitted by a line source with the geometry of Fig. 4.6. The electric field in the geometrical optics limit can be written as

$$E_{\mathrm{GO}} = \frac{\mathrm{e}^{\mathrm{i}kR}}{\sqrt{kR}}\Theta(\pi-\alpha). \tag{B.4}$$

Again, there is only field in the illuminated region. When the diffracted field is taken into account using the GTD, we find

$$E_{\mathrm{GTD}} = \frac{\mathrm{e}^{\mathrm{i}kR}}{\sqrt{kR}}\Theta(\pi-\alpha) + \frac{\mathrm{e}^{\mathrm{i}kr_0}}{\sqrt{kr_0}}\frac{\mathrm{e}^{\mathrm{i}kr}}{\sqrt{kr}}D, \tag{B.5}$$

which diverges at the shadow boundary. Note that the diffracted wave is cylindrical for both cases of plane wave incidence and line source (compare the shadow region in Fig. B.1(b) and Fig. B.2(b), for instance). The discontinuity of Eq. (B.5) can be avoided using the UAT, which provides a regularized expression for the whole space,

$$E_{\mathrm{UAT}} = \frac{\mathrm{e}^{\mathrm{i}kR}}{\sqrt{kR}}\mathcal{F}(w) + \frac{\mathrm{e}^{\mathrm{i}kr_0}}{\sqrt{kr_0}}\frac{\mathrm{e}^{\mathrm{i}kr}}{\sqrt{kr}}\tilde{D}, \tag{B.6}$$

with the modified diffraction coefficient $\tilde{D}$ given by Eq. (4.30) and the argument of the Fresnel integral is $w = \sigma\sqrt{k(r+r_0-R)}$, with $\sigma \equiv \mathrm{sgn}\left[\cos\left(\alpha/2\right)\right]$. In this case we can also see lines of

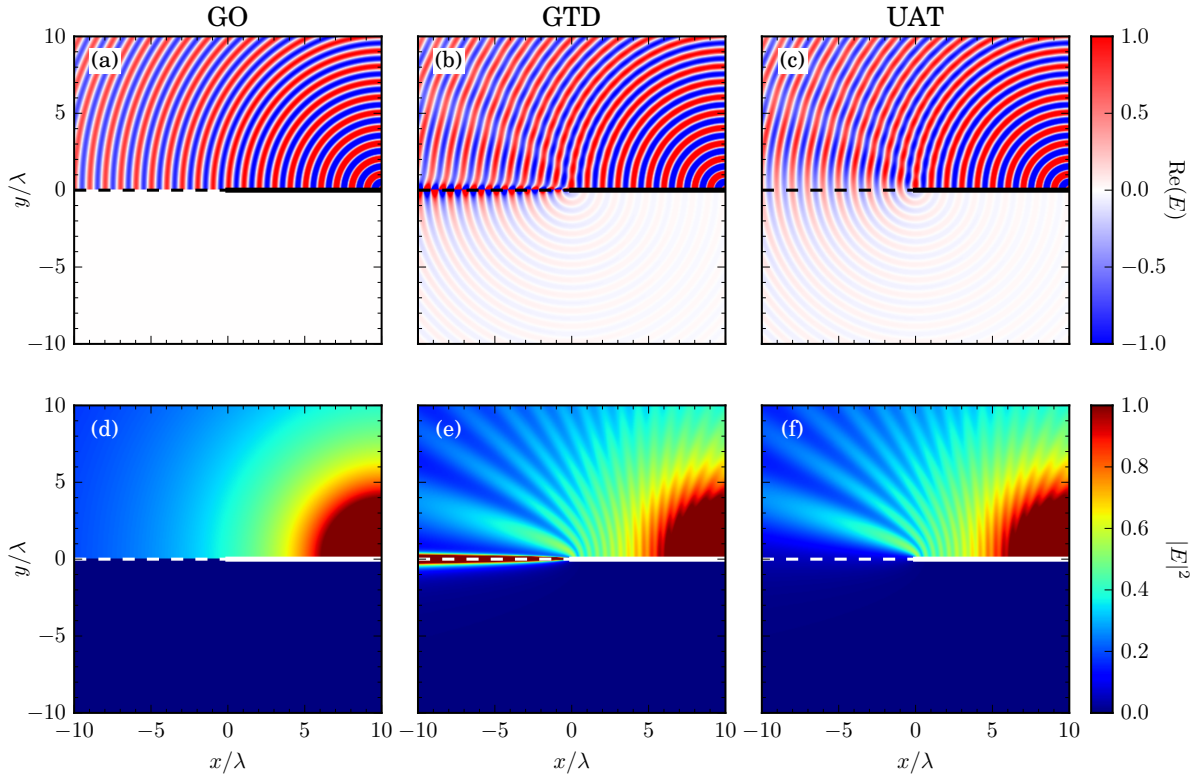

Figure B.2: (a)-(c) Real part of the electric field Re(E) and (d)-(f) squared electric field norm $|E|^2$ of a cylindrical wave emitted by a line source located on conducting half-plane screen (denoted by a solid line) at $r_0 = 10\lambda$ for (a),(d) the geometrical optics limit (B.4); (b),(e) geometrical theory of diffraction (B.5) and (c),(f) uniform asymptotic theory (B.6). The dashed line indicates the shadow boundary. The field is given in arbitrary units.

interference of GO and D waves but in the shape of hyperbolas in Fig. B.2 for the GTD and UAT (see Sec. 4.4).

From these results we can confirm that the GTD is a very good approximation in the whole space except in the surroundings of the shadow boundaries for both the plane wave and cylindrical wave case.

The figures presented in this appendix may be compared with those in Sec. 4.6 (Figs. 4.23 and 4.24, for instance). We can see how different the emerging wave patterns are. Nevertheless, we have seen that by adequately combining two half-plane screens one can analytically describe wave propagation in conical topology.

APPENDIX C

Supplementary metamaterial simulations of cosmic string spacetime

C.1 Cylindrical wave

In Sec. 4.6 we provided some results of numerically solving the wave equation for a TE-polarized wave in a metamaterial mimicking cosmic string topology. However, we only presented some illustrative simulations for one string-source distance r_0 and three deficit angles Δ to support the analytical models exposed in Secs. 4.3 and 4.4.

In this appendix we present Fig. C.1, which includes the simulation results for three different values of r_0 and two values of Δ. We can contrast how the features of the wave field change in the different cases. First, we can see that as the distance from the string to the source increases, more fringes appear in the double-imaging region. In the limit of an infinitely distant source, $r_0 \to \infty$, one would recover the results for the plane wave, i.e. Fig. 4.12(d). We also observe that the fringes become wider as r_0 decreases. Secondly, as the double-imaging region is larger for higher values of Δ, more fringes *fit* into the region. Consequently, as the deficit angle decreases, the wave phenomenon becomes more directional. Moreover, we also notice that as the number of nodal and antinodal lines increases (i.e. large r_0 and Δ), more diffraction maxima appear. Nevertheless, contrary to what happens with plane wave incidence, only a certain amount of maxima are possible in the case of the cylindrical wave before it naturally decays [compare, for instance, Fig. 4.15 with Fig. 4.14(a) or Fig. 4.16(a)]. This effect can be clearly seen in Fig. C.1(c). Note that the hyperbolas that determine the diffraction saddle points can be easily perceived as well in the same figure.

C.2 Gaussian beam

For the metamaterial analogous to the cosmic string, we have only performed simulations of the propagation of a cylindrical wave given that it allows to observe the interference wave pattern. For completeness, we can also be interested in comparing the null-geodesics in the conical geometry with the propagation of a Gaussian beam as done for the black hole case. We proceed in a similar way to that of Sec. 3.5: we consider a rectangular domain surrounded by a perfectly matched layer and inject a TE-polarized wave with a Gaussian shape at (x_0, y_0) from the left boundary. We must take into account that the medium characterized by Eq. (4.5) is anisotropic

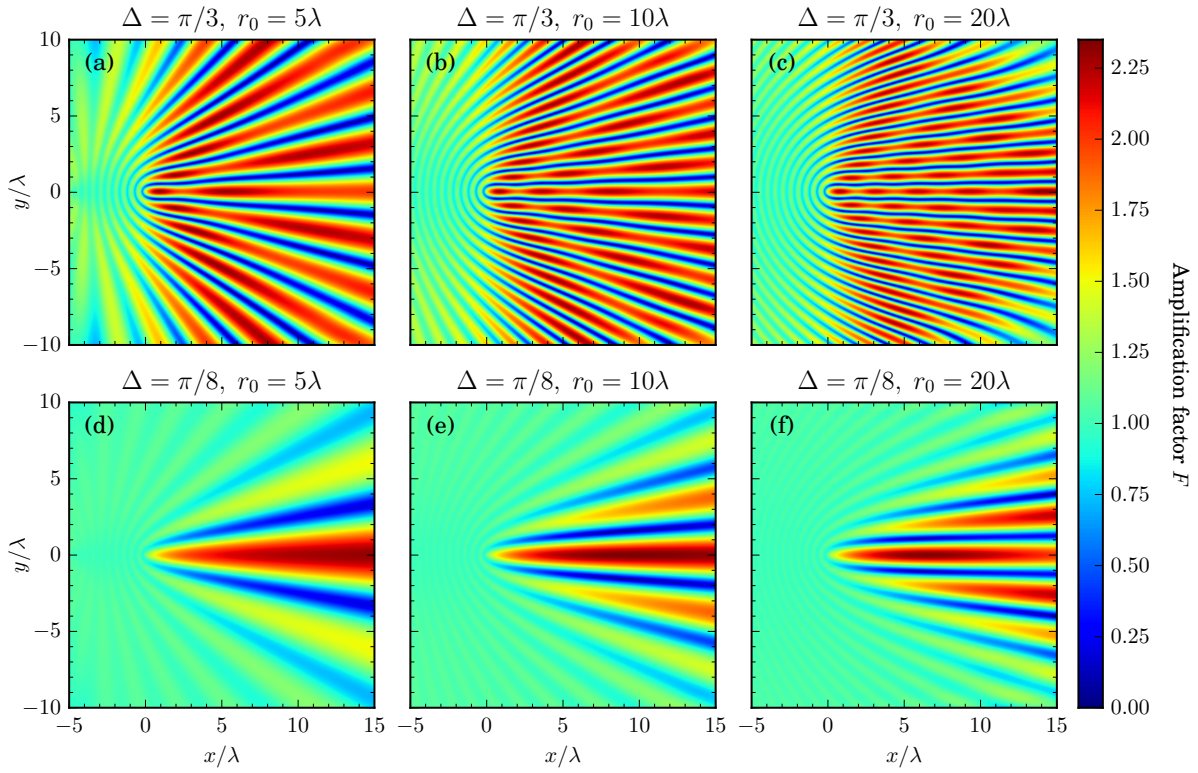

Figure C.1: Spatial distribution of the amplification factor F obtained from simulations in a metamaterial with (a)-(c) $\Delta = \pi/3$ and (d)-(f) $\Delta = \pi/8$. Three different source-string distances have been chosen for comparison: (a),(d) $r_0 = 5\lambda$; (b),(e) $r_0 = 10\lambda$ and (c),(f) $r_0 = 20\lambda$.

and therefore, there will be an angle α between energy and phase propagation given by

$$\tan\alpha = \frac{(1-\beta^2)x_0 y_0}{\beta^2 y_0^2 + x_0^2}. \tag{C.1}$$

Note that, contrarily to the spherically symmetric case, the conical topology cannot transformed to be mimicked by an isotropic metamaterial due to its singular curvature.

In Fig. C.2 we show the numerical results of solving the wave equation (2.18) in media with three different Δ parameters. We superimpose a white line corresponding to the null-geodesics calculated from Eqs. (4.16) and observe a good correspondence with the Gaussian beam in the three cases. It can be observed that the deflection angle is indeed dependent on the deficit angle Δ. We can clearly see – particularly in Figs. C.2(b) and (c) – that the wavefronts are not perpendicular to the direction of propagation. We also observe a broadening of the injected beam, which becomes more significant as the parameter Δ increases. The same effect is seen in some of the figures of Ref. [52] as well. They also stated that media with $\Delta < 0$ had the opposite effect, the beam narrowed in them. We note that a similar pattern to that described by the nodal and antinodal lines appears as ripples on the beam. They may happen because a part of the beam passes on the opposite side of the string (due to the broadening), interfering with the main part of the beam.

It is worth reminding that, as we can see, rays are bent even if they travel along a region of flat spacetime. This is a physical manifestation arising from the singular δ-like curvature of the cosmic string metric, which has been said to be analogous to the Aharonov-Bohm effect [102, 150, 151].

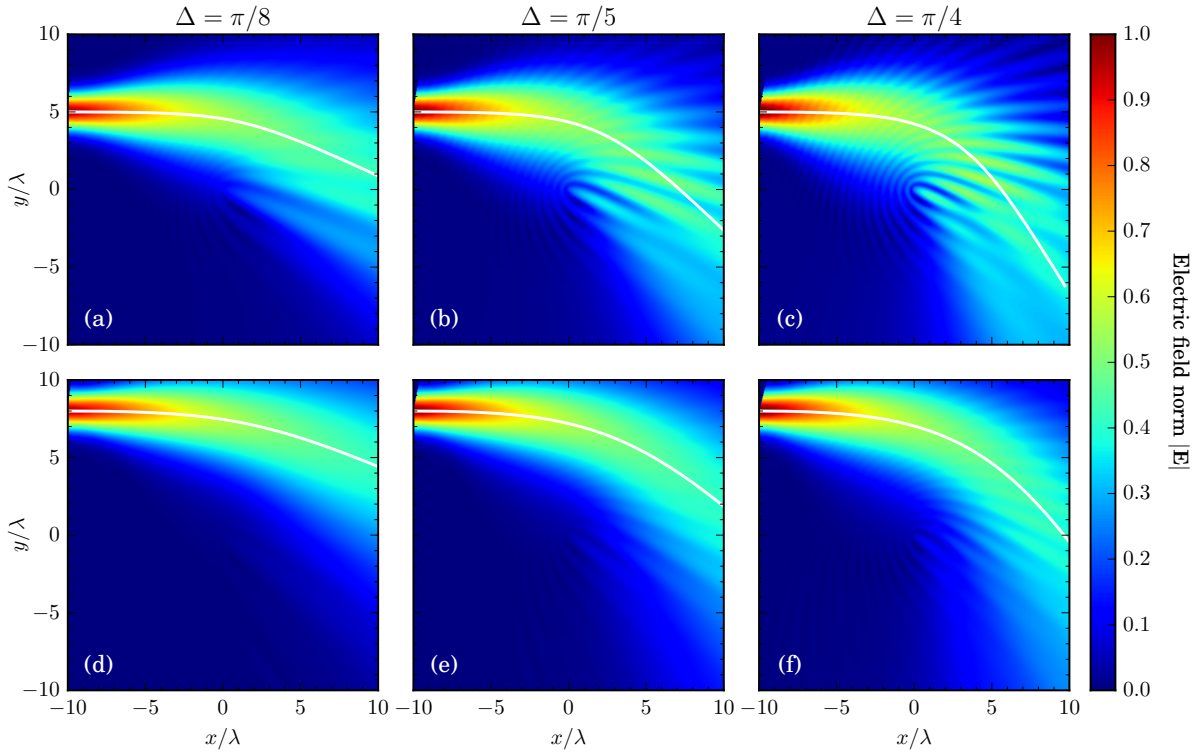

Figure C.2: Simulation of a TE Gaussian beam of waist radius $w_0 = 1.2\lambda$ injected at (a)-(c) $(x_0, y_0) = (-10\lambda, 5\lambda)$ and (d)-(f) $(x_0, y_0) = (-10\lambda, 8\lambda)$ compared with ray path (superimposed in white) in metamaterial mimicking cosmic string spacetimes with different deficit angles: (a),(d) $\Delta = \pi/8$; (b),(e) $\Delta = \pi/5$ and (c),(f) $\Delta = \pi/4$. The electric field norm $|\mathbf{E}|$ is given in arbitrary units.

Bibliography

[1] M. Novello, M. Visser, and G. Volovik (eds.), *Artificial Black Holes*, (World Scientific Publishing, Singapore, 2002).

[2] G. E. Volovik, *The Universe in a Helium Droplet*, (Oxford University Press, New York, NY, 2009).

[3] C. Barceló, S. Liberati, and M. Visser, *Analogue gravity*, Living Rev. Relativ. **14**, 3 (2011).

[4] W. G. Unruh, *Experimental black-hole evaporation?*, Phys. Rev. Lett. **46**, 1351 (1981).

[5] H. Chen, C. T. Chan, and P. Sheng, *Transformation optics and metamaterials*, Nat. Mater. **9**, 387 (2010).

[6] W. Cai and V. Shalaev, *Optical Metamaterials*, (Springer, New York, NY, 2010).

[7] S. N. Burokur, *Transformation Optics-Based Antennas*, (ISTE Press Ltd, London, 2016).

[8] X. C. Tong, *Functional Metamaterials and Metadevices*, vol. 262 of *Springer Series in Materials Science*, (Springer International Publishing, Cham, 2018).

[9] W. Gordon, *Zur Lichtfortpflanzung nach der Relativitätstheorie*, Ann. Phys. **72**, 421 (1923).

[10] I. E. Tamm, *The electrodynamics of anisotropic media in the special theory of relativity*, J. Russ. Phys. Chem. Soc. **56**, 248 (1924).

[11] I. E. Tamm, *The crystal-optical theory of relativity , as it relates to the geometry of bi-quadratic forms*, J. Russ. Phys. Chem. Soc. **57**, 209 (1925).

[12] G. V. Skrotskii, *The influence of gravitation on the propagation of light*, Sov. Phys. Dokl. **2**, 226 (1957).

[13] J. Plebanski, *Electromagnetic waves in gravitational fields*, Phys. Rev. **118**, 1396 (1960).

[14] F. de Felice, *On the gravitational field acting as an optical medium*, Gen. Relativ. Gravit. **2**, 347 (1971).

[15] B. Mashhoon, *Scattering of electromagnetic radiation from a black hole*, Phys. Rev. D **7**, 2807 (1973).

[16] M. Lax and D. F. Nelson, *Maxwell equations in material form*, Phys. Rev. B **13**, 1777 (1976).

[17] W. Schleich and M. O. Scully, *General relativity and modern optics*, in *New Trends At. Physics, Les Houches 1982, Sess. 38*, 995–1124, (Elsevier, Amsterdam, 1984).

[18] D. R. Smith, W. J. Padilla, D. C. Vier, S. C. Nemat-Nasser, and S. Schultz, *Composite medium with simultaneously negative permeability and permittivity*, Phys. Rev. Lett. **84**, 4184 (2000).

[19] F. Capolino (ed.), *Theory and Phenomena of Metamaterials*, (CRC Press, Boca Raton, FL, 2009).

[20] A. Sihvola, *Metamaterials in electromagnetics*, Metamaterials **1**, 2 (2007).

[21] M. A. Noginov and V. A. Podolskiy (eds.), *Tutorials in Metamaterials*, (CRC Press, Boca Raton, FL, 2012).

[22] D. R. Smith, J. B. Pendry, and M. C. K. Wiltshire, *Metamaterials and negative refractive index*, Science **305**, 788 (2004).

[23] J. Valentine, S. Zhang, T. Zentgraf, E. Ulin-Avila, D. A. Genov, G. Bartal, and X. Zhang, *Three-dimensional optical metamaterial with a negative refractive index*, Nature **455**, 376 (2008).

[24] D. Schurig, J. J. Mock, B. J. Justice, S. A. Cummer, J. B. Pendry, A. F. Starr, and D. R. Smith, *Metamaterial electromagnetic cloak at microwave frequencies*, Science **314**, 977 (2006).

[25] J. B. Pendry, *Negative refraction makes a perfect lens*, Phys. Rev. Lett. **85**, 3966 (2000).

[26] N. Fang, H. Lee, C. Sun, and X. Zhang, *Sub–diffraction-limited optical imaging with a silver superlens.*, Science **308**, 534 (2005).

[27] Z. Jacob, L. V. Alekseyev, and E. Narimanov, *Optical hyperlens: Far-field imaging beyond the diffraction limit*, Opt. Express **14**, 8247 (2006).

[28] A. Salandrino and N. Engheta, *Far-field subdiffraction optical microscopy using metamaterial crystals: Theory and simulations*, Phys. Rev. B **74**, 075103 (2006).

[29] Z. Jacob, L. V. Alekseyev, and E. Narimanov, *Semiclassical theory of the hyperlens*, J. Opt. Soc. Am. A **24**, 52 (2007).

[30] J. Sun, M. I. Shalaev, and N. M. Litchinitser, *Experimental demonstration of a non-resonant hyperlens in the visible spectral range*, Nat. Commun. **6**, 7201 (2015).

[31] A. Poddubny, I. Iorsh, P. Belov, and Y. Kivshar, *Hyperbolic metamaterials*, Nat. Photonics **7**, 948 (2013).

[32] P. Shekhar, J. Atkinson, and Z. Jacob, *Hyperbolic metamaterials: Fundamentals and applications*, Nano Converg. **1**, 14 (2014).

[33] L. Ferrari, C. Wu, D. Lepage, X. Zhang, and Z. Liu, *Hyperbolic metamaterials and their applications*, Prog. Quantum Electron. **40**, 1 (2015).

[34] J. Li and C. T. Chan, *Double-negative acoustic metamaterial*, Phys. Rev. E **70**, 055602 (2004).

[35] S. Zhang, C. Xia, and N. Fang, *Broadband acoustic cloak for ultrasound waves*, Phys. Rev. Lett. **106**, 024301 (2011).

[36] S. Brûlé, E. H. Javelaud, S. Enoch, and S. Guenneau, *Experiments on seismic metamaterials: Molding surface waves*, Phys. Rev. Lett. **112**, 133901 (2014).

[37] D. A. Genov, S. Zhang, and X. Zhang, *Mimicking celestial mechanics in metamaterials*, Nat. Phys. **5**, 687 (2009).

[38] E. E. Narimanov and A. V. Kildishev, *Optical black hole: Broadband omnidirectional light absorber*, Appl. Phys. Lett. **95**, 041106 (2009).

[39] Q. Cheng, T. J. Cui, W. X. Jiang, and B. G. Cai, *An omnidirectional electromagnetic absorber made of metamaterials*, New J. Phys. **12**, 063006 (2010).

[40] Y. Yang, L. Yoke Leng, N. Wang, Y. Ma, and C. K. Ong, *Electromagnetic field attractor made of gradient index metamaterials*, J. Opt. Soc. Am. A **29**, 473 (2012).

[41] M. Yin, X. Y. Tian, L. L. Wu, and D. C. Li, *A broadband and omnidirectional electromagnetic wave concentrator with gradient woodpile structure*, Opt. Express **21**, 19082 (2013).

[42] C. Sheng, H. Liu, Y. Wang, S. N. Zhu, and D. A. Genov, *Trapping light by mimicking gravitational lensing*, Nat. Photonics **7**, 902 (2013).

[43] Y. Y. Lee, E. S. Kang, K. H. Jung, J. W. Lee, and D. Ahn, *Elliptic cylindrical pseudo-optical black hole for omnidirectional light absorber*, J. Opt. Soc. Am. B **31**, 1948 (2014).

[44] L. J. Prokopeva and A. V. Kildishev, *Expanding the theory of circular omnidirectional light concentrators to elliptic and spheroidal designs*, J. Opt. **18**, 044014 (2016).

[45] R. T. Thompson and J. Frauendiener, *Dielectric analog space-times*, Phys. Rev. D **82**, 124021 (2010).

[46] H. Chen, R.-X. Miao, and M. Li, *Transformation optics that mimics the system outside a Schwarzschild black hole*, Opt. Express **18**, 15183 (2010).

[47] I. Fernández-Núñez and O. Bulashenko, *Anisotropic metamaterial as an analogue of a black hole*, Phys. Lett. A **380**, 1 (2016).

[48] R. Bekenstein, Y. Kabessa, Y. Sharabi, O. Tal, N. Engheta, G. Eisenstein, A. J. Agranat, and M. Segev, *Control of light by curved space in nanophotonic structures*, Nat. Photonics **11**, 664 (2017).

[49] S. Jia, D. La, and X. Ma, *Numerical simulation of electromagnetic waves in Schwarzschild space–time by finite difference time domain method and Green function method*, Comput. Phys. Commun. **225**, 166 (2018).

[50] D. G. Pires, J. C. A. Rocha, and P. A. Brandão, *Ergoregion in metamaterials mimicking a Kerr spacetime*, J. Opt. **20**, 025101 (2018).

[51] T. G. Mackay and A. Lakhtakia, *Towards a metamaterial simulation of a spinning cosmic string*, Phys. Lett. A **374**, 2305 (2010).

[52] Y.-L. Zhang, X.-Z. Dong, M.-L. Zheng, Z.-S. Zhao, and X.-M. Duan, *Steering electromagnetic beams with conical curvature singularities*, Opt. Lett. **40**, 4783 (2015).

[53] L. Shi, H. Li, C. Xie, and Y. Zhang, *Omnidirectional diffraction control with rotational topological defects*, Opt. Express **23**, 25773 (2015).

[54] I. Fernández-Núñez and O. Bulashenko, *Wave propagation in metamaterials mimicking the topology of a cosmic string*, J. Opt. **20**, 045603 (2018).

[55] J. Hu and H. Yu, *Manipulating lightcone fluctuations in an analogue cosmic string*, Phys. Lett. B **777**, 346 (2018).

[56] A. Greenleaf, Y. Kurylev, M. Lassas, and G. Uhlmann, *Electromagnetic wormholes and virtual magnetic monopoles from metamaterials*, Phys. Rev. Lett. **99**, 183901 (2007).

[57] J. Prat-Camps, C. Navau, and A. Sanchez, *A magnetic wormhole*, Sci. Rep. **5**, 12488 (2015).

[58] R. Schützhold, G. Plunien, and G. Soff, *Dielectric black hole analogs*, Phys. Rev. Lett. **88**, 061101 (2002).

[59] U. Leonhardt, *On cosmology in the laboratory*, Philos. Trans. R. Soc. A **373**, 20140354 (2015).

[60] A. Einstein, *Die Feldgleichungen der Gravitation*, Sitzber. Preuss. Akad. Wiss. Berlin 844–847 (1915).

[61] K. Schwarzschild, *Über das Gravitationsfeld eines Massenpunktes nach der Einsteinschen Theorie*, Sitzber. Preuss. Akad. Wiss. Berlin 189–196 (1916).

[62] M. Fathi and R. T. Thompson, *Cartographic distortions make dielectric spacetime analog models imperfect mimickers*, Phys. Rev. D **93**, 124026 (2016).

[63] S. Dehdashti, H. Wang, Y. Jiang, Z. Xu, and H. Chen, *Review of black hole realization in laboratory based on transformation optics*, Prog. Electromagn. Res. **154**, 181 (2015).

[64] T. W. B. Kibble, *Topology of cosmic domains and strings*, J. Phys. A. Math. Gen. **9**, 1387 (1976).

[65] A. Vilenkin, *Gravitational field of vacuum domain walls and strings*, Phys. Rev. D **23**, 852 (1981).

[66] A. Vilenkin and E. P. S. Shellard, *Cosmic Strings and Other Topological Defects*, (Cambridge University Press, Cambridge, 1994).

[67] S. Deguchi and W. D. Watson, *Wave effects in gravitational lensing of electromagnetic radiation*, Phys. Rev. D **34**, 1708 (1986).

[68] P. Schneider, J. Ehlers, and E. E. Falco, *Gravitational Lenses*, (Springer, New York, NY, 1992).

[69] T. T. Nakamura and S. Deguchi, *Wave optics in gravitational lensing*, Prog. Theor. Phys. Suppl. **133**, 137 (1999).

[70] M. J. Bowick, L. Chandar, E. A. Schiff, and A. M. Srivastava, *The cosmological Kibble mechanism in the laboratory: String formation in liquid crystals*, Science **263**, 943 (1994).

[71] M. O. Katanaev, *Geometric theory of defects*, Phys. Usp. **48**, 675 (2005).

[72] M. Kleman and J. Friedel, *Disclinations, dislocations, and continuous defects: A reappraisal*, Rev. Mod. Phys. **80**, 61 (2008).

[73] M. A. Vozmediano, M. I. Katsnelson, and F. Guinea, *Gauge fields in graphene*, Phys. Rep. **496**, 109 (2010).

[74] E. Pereira, S. Fumeron, and F. Moraes, *Metric approach for sound propagation in nematic liquid crystals*, Phys. Rev. E **87**, 022506 (2013).

[75] S. Fumeron, B. Berche, F. Santos, E. Pereira, and F. Moraes, *Optics near a hyperbolic defect*, Phys. Rev. A **92**, 063806 (2015).

[76] K. A. Seffen, *Fundamental conical defects: The d-cone, its e-cone, and its p-cone*, Phys. Rev. E **94**, 1 (2016).

[77] S. Fumeron, B. Berche, F. Moraes, F. A. Santos, and E. Pereira, *Geometrical optics limit of phonon transport in a channel of disclinations*, Eur. Phys. J. B **90**, 95 (2017).

[78] A. Sommerfeld, *Lectures on Theoretical Physics (Vol. IV): Optics*, (Academic Press, New York, NY, 1954).

[79] J. B. Keller, *Geometrical theory of diffraction*, J. Opt. Soc. Am. **52**, 116 (1962).

[80] D. S. Ahluwalia, R. M. Lewis, and J. Boersma, *Uniform asymptotic theory*, SIAM J. Appl. Math. **16**, 783 (1968).

[81] V. A. Borovikov and B. E. Kinber, *Geometrical Theory of Diffraction*, (The Institution of Electrical Engineers, London, 1994).

[82] B. Linet, *On the wave equations in the spacetime of a cosmic string*, Ann. l'lnstitut Henri Poincaré **45**, 249 (1986).

[83] T. Suyama, T. Tanaka, and R. Takahashi, *Exact wave propagation in a spacetime with a cosmic string*, Phys. Rev. D **73**, 024026 (2006).

[84] B. P. Abbott, R. Abbott, T. D. Abbott, M. R. Abernathy, F. Acernese, K. Ackley, C. Adams, T. Adams, P. Addesso, R. X. Adhikari, et al., *Observation of gravitational waves from a binary black hole merger*, Phys. Rev. Lett. **116**, 061102 (2016).

[85] P.-H. Chang, C.-Y. Kuo, and R.-L. Chern, *Wave splitting and double-slit like interference by a pseudochiral metamaterial slab*, J. Phys. D. Appl. Phys. **48**, 295103 (2015).

[86] E. Tonti, *The origin of analogies in physics*, in *Systemics of Emergence: Research and Development*, 695–706, (Springer-Verlag, New York, NY, 2006).

[87] M. Visser, *Acoustic black holes: Horizons, ergospheres and Hawking radiation*, Class. Quantum Gravity **15**, 1767 (1998).

[88] T. A. Jacobson and G. E. Volovik, *Event horizons and ergoregions in ^3He*, Phys. Rev. D **58**, 064021 (1998).

[89] S. Basak and P. Majumdar, *'Superresonance' from a rotating acoustic black hole*, Class. Quantum Gravity **20**, 3907 (2003).

[90] L. J. Garay, J. R. Anglin, J. I. Cirac, and P. Zoller, *Sonic analog of gravitational black holes in Bose-Einstein condensates*, Phys. Rev. Lett. **85**, 4643 (2000).

[91] R. Balbinot, A. Fabbri, S. Fagnocchi, A. Recati, and I. Carusotto, *Nonlocal density correlations as a signature of Hawking radiation from acoustic black holes*, Phys. Rev. A **78**, 021603 (2008).

[92] I. Carusotto, S. Fagnocchi, A. Recati, R. Balbinot, and A. Fabbri, *Numerical observation of Hawking radiation from acoustic black holes in atomic Bose-Einstein condensates*, New J. Phys. **10**, 103001 (2008).

[93] O. Lahav, A. Itah, A. Blumkin, C. Gordon, S. Rinott, A. Zayats, and J. Steinhauer, *Realization of a sonic black hole analog in a Bose-Einstein condensate*, Phys. Rev. Lett. **105**, 240401 (2010).

[94] R. Schützhold and W. G. Unruh, *Gravity wave analogues of black holes*, Phys. Rev. D **66**, 044019 (2002).

[95] G. Rousseaux, C. Mathis, P. Maïssa, T. G. Philbin, and U. Leonhardt, *Observation of negative-frequency waves in a water tank: A classical analogue to the Hawking effect?*, New J. Phys. **10**, 053015 (2008).

[96] A. Cortijo and M. A. Vozmediano, *Effects of topological defects and local curvature on the electronic properties of planar graphene*, Nucl. Phys. B **763**, 293 (2007).

[97] M. Katsnelson and K. Novoselov, *Graphene: New bridge between condensed matter physics and quantum electrodynamics*, Solid State Commun. **143**, 3 (2007).

[98] A. Vilenkin, *Cosmic strings as gravitational lenses*, Astrophys. J. **282**, L51 (1984).

[99] D. L. Osipov, *Diffraction of light by a cosmic string*, JETP Lett. **62**, 765 (1995).

[100] I. Fernández-Núñez and O. Bulashenko, *Wave diffraction by a cosmic string*, Phys. Lett. A **380**, 2897 (2016).

[101] I. Fernández-Núñez and O. Bulashenko, *Emergence of Fresnel diffraction zones in gravitational lensing by a cosmic string*, Phys. Lett. A **381**, 1764 (2017).

[102] K. Kraus, *Remarks on a class of almost trivial solutions of the gravitational field equation*, Ann. Phys. **50**, 102 (1968).

[103] S. Weinberg, *Gravitation and Cosmology*, (Wiley, New York, NY, 1972).

[104] D. V. Gal'tsov and E. Masar, *Geodesics in spacetimes containing cosmic strings*, Class. Quantum Gravity **6**, 1313 (1989).

[105] A. de Padua, F. Parisio-Filho, and F. Moraes, *Geodesics around line defects in elastic solids*, Phys. Lett. A **238**, 153 (1998).

[106] J. D. Joannopoulos, S. G. Johnson, J. N. Winn, and R. D. Meade, *Photonic Crystals: Molding the Flow of Light*, (Princeton University Press, Princeton and Oxford, 2008).

[107] V. Veselago, L. Braginsky, V. Shklover, and C. Hafner, *Negative refractive index materials*, J. Comput. Theor. Nanosci. **3**, 189 (2006).

[108] V. G. Veselago, *The electrodynamics of substances with simultaneously negative values of ϵ and μ*, Sov. Phys. Usp. **10**, 509 (1968).

[109] J. D. Jackson, *Classical Electrodynamics*, 3rd edn., (Wiley, New York, NY, 1999).

[110] J. B. Pendry, A. J. Holden, W. J. Stewart, and I. Youngs, *Extremely low frequency plasmons in metallic mesostructures*, Phys. Rev. Lett. **76**, 4773 (1996).

[111] J. B. Pendry, A. J. Holden, D. J. Robbins, and W. J. Stewart, *Magnetism from conductors and enhanced nonlinear phenomena*, IEEE Trans. Microw. Theory Tech. **47**, 2075 (1999).

[112] C. M. Soukoulis and M. Wegener, *Past achievements and future challenges in the development of three-dimensional photonic metamaterials*, Nat. Photonics **5**, 523 (2011).

[113] Z. J. Wong, Y. Wang, K. O'Brien, J. Rho, X. Yin, S. Zhang, N. Fang, T.-J. Yen, and X. Zhang, *Optical and acoustic metamaterials: Superlens, negative refractive index and invisibility cloak*, J. Opt. **19**, 084007 (2017).

[114] Y. K. Ahn, H. J. Lee, and Y. Y. Kim, *Conical refraction of elastic waves by anisotropic metamaterials and application for parallel translation of elastic waves*, Sci. Rep. **7**, 10072 (2017).

[115] J. P. Turpin, J. A. Bossard, K. L. Morgan, D. H. Werner, and P. L. Werner, *Reconfigurable and tunable metamaterials: A review of the theory and applications*, Int. J. Antennas Propag. **2014**, 429837 (2014).

[116] N. I. Zheludev and E. Plum, *Reconfigurable nanomechanical photonic metamaterials*, Nat. Nanotechnol. **11**, 16 (2016).

[117] W. Rotman, *Plasma simulation by artificial dielectrics and parallel-plate media*, IRE Trans. Antennas Propag. **10**, 82 (1962).

[118] S. Jahani and Z. Jacob, *All-dielectric metamaterials*, Nat. Nanotechnol. **11**, 23 (2016).

[119] S. J. Corbitt, M. Francoeur, and B. Raeymaekers, *Implementation of optical dielectric metamaterials: A review*, J. Quant. Spectrosc. Radiat. Transf. **158**, 3 (2015).

[120] A. Selimis, V. Mironov, and M. Farsari, *Direct laser writing: Principles and materials for scaffold 3D printing*, Microelectron. Eng. **132**, 83 (2015).

[121] D. R. Smith, D. C. Vier, T. Koschny, and C. M. Soukoulis, *Electromagnetic parameter retrieval from inhomogeneous metamaterials*, Phys. Rev. E **71**, 036617 (2005).

[122] X. Zhang and Y. Wu, *Effective medium theory for anisotropic metamaterials*, Sci. Rep. **5**, 7892 (2015).

[123] M. Born and E. Wolf, *Principles of Optics*, 7th edn., (Cambridge University Press, Cambridge, 1999).

[124] L. D. Landau and E. M. Lifshitz, *Electrodynamics Of Continuous Media, Vol. 8*, 2nd edn., (Pergamon, New York, NY, 1984).

[125] D. R. Smith and D. Schurig, *Electromagnetic wave propagation in media with indefinite permittivity and permeability tensors*, Phys. Rev. Lett. **90**, 077405 (2003).

[126] I. I. Smolyaninov and Y.-J. Hung, *Modeling of time with metamaterials*, J. Opt. Soc. Am. B **28**, 1591 (2011).

[127] J. J. Sakurai, *Advanced Quantum Mechanics*, (Addison-Wesley, Reading, MA, 1967).

[128] I. I. Smolyaninov, Y. J. Hung, and E. Hwang, *Experimental modeling of cosmological inflation with metamaterials*, Phys. Lett. A **376**, 2575 (2012).

[129] I. I. Smolyaninov, E. Hwang, and E. Narimanov, *Hyperbolic metamaterial interfaces: Hawking radiation from Rindler horizons and spacetime signature transitions*, Phys. Rev. B **85**, 235122 (2012).

[130] D. Figueiredo, F. Moraes, S. Fumeron, and B. Berche, *Cosmology in the laboratory: An analogy between hyperbolic metamaterials and the Milne universe*, Phys. Rev. D **96**, 105012 (2017).

[131] U. Leonhardt and T. G. Philbin, *General relativity in electrical engineering*, New J. Phys. **8**, 247 (2006).

[132] U. Leonhardt and T. Philbin, *Geometry and Light: The Science of Invisibility*, (Dover Publications, Mineola, NY, 2010).

[133] C. W. Misner, K. S. Thorne, and J. A. Wheeler, *Gravitation*, (W. H. Freeman and Company, San Francisco, CA, 1973).

[134] I. V. Lindell, A. H. Sihvola, S. A. Tretyakov, and A. J. Viitanen, *Electromagnetic Waves in Chiral and Bi-isotropic Media*, (Artech House, Norwood, MA, 1994).

[135] F. W. Dyson, A. S. Eddington, and C. Davidson, *A determination of the deflection of light by the Sun's gravitational field, from observations made at the total eclipse of May 29, 1919*, Philos. Trans. R. Soc. A **220**, 291 (1920).

[136] S. Chandrasekhar, *The Mathematical Theory of Black Holes*, (Oxford University Press, Oxford, 1983).

[137] J. McCleary, *Geometry from a Differentiable Viewpoint*, (Cambridge University Press, Cambridge, 1994).

[138] L. D. Landau and E. M. Lifshitz, *The Classical Theory of Fields, Vol. 2*, 4th edn., (Pergamon, New York, NY, 1975).

[139] S. M. Barnett and R. Loudon, *The enigma of optical momentum in a medium*, Philos. Trans. R. Soc. A **368**, 927 (2010).

[140] B. E. A. Saleh and M. C. Teich, *Fundamentals of Photonics*, 2nd edn., (Wiley, Hoboken, NJ, 2007).

[141] R.-Q. Li, X.-F. Zhu, B. Liang, Y. Li, X.-Y. Zou, and J.-C. Cheng, *A broadband acoustic omnidirectional absorber comprising positive-index materials*, Appl. Phys. Lett. **99**, 193507 (2011).

[142] A. Climente, D. Torrent, and J. Sánchez-Dehesa, *Omnidirectional broadband acoustic absorber based on metamaterials*, Appl. Phys. Lett. **100**, 144103 (2012).

[143] H. Zhang, B. Liang, X.-y. Zou, J. Yang, J. Yang, and J.-c. Cheng, *Omnidirectional broadband acoustic deflector based on metamaterials*, Appl. Phys. Express **10**, 027201 (2017).

[144] T. G. Mackay, *Towards metamaterials with giant dielectric anisotropy via homogenization: An analytical study*, Photonics Nanostructures - Fundam. Appl. **13**, 8 (2015).

[145] H. Jung, C. In, H. Choi, and H. Lee, *Anisotropy modeling of terahertz metamaterials: Polarization dependent resonance manipulation by meta-atom cluster*, Sci. Rep. **4**, 5217 (2014).

[146] J. R. Gott, *Gravitational lensing effects of vacuum strings: Exact solutions*, Astrophys. J. **288**, 422 (1985).

[147] D. D. Sokolov and A. A. Starobinskii, *The structure of the curvature tensor at conical singularities*, Sov. Phys. Dokl. **22**, 312 (1977).

[148] J. A. G. Vickers, *Generalised cosmic strings*, Class. Quantum Gravity **4**, 1 (1987).

[149] K. Jusufi, İ. Sakallı, and A. Övgün, *Effect of Lorentz symmetry breaking on the deflection of light in a cosmic string spacetime*, Phys. Rev. D **96**, 024040 (2017).

[150] J. S. Dowker, *A gravitational Aharonov-Bohm effect*, Nuovo Cim. B **52**, 129 (1967).

[151] L. H. Ford and A. Vilenkin, *A gravitational analogue of the Aharonov-Bohm effect*, J. Phys. A. Math. Gen. **14**, 2353 (1981).

[152] A. M. d. M. Carvalho, C. Sátiro, and F. Moraes, *Aharonov-Bohm–like effect for light propagating in nematics with disclinations*, Europhys. Lett. **80**, 46002 (2007).

[153] H. M. Macdonald, *A class of diffraction problems*, Proc. London Math. Soc. **14**, 410 (1915).

[154] P. C. Clemmow, *A note on the diffraction of a cylindrical wave by a perfectly conducting half-plane*, Q. J. Mech. Appl. Math. **3**, 377 (1950).

[155] J. J. Bowman, T. B. A. Senior, and P. L. E. Uslenhi, *Electromagnetic and Acoustic Scattering by Simple Shapes*, (North-Holland Publishing Company, Amsterdam, 1969).

[156] A. Fresnel, *Mémoire sur la diffraction de la lumière*, Mém. Acad. Sci. **5**, 339 (1821).

[157] H. Crew (ed.), *The Wave Theory of Light: Memoirs of Huygens, Young and Fresnel*, (American Book Company, New York, NY, 1900).

[158] J. S. Dowker, *Quantum field theory on a cone*, J. Phys. A. Math. Gen. **10**, 115 (1977).

[159] S. A. Fulling, C. S. Trendafilova, P. N. Truong, and J. Wagner, *Wedges, cones, cosmic strings and their vacuum energy*, J. Phys. A Math. Theor. **45**, 374018 (2012).

[160] Y. Z. Umul, *Wedge diffraction model in gravitational lensing by cosmic strings*, Optik **157**, 1227 (2018).

[161] H. L. Bertoni, *Radio Propagation for Modern Wireless Systems*, (Prentice Hall PTR, Upper Saddle River, NJ, 1999).

[162] C. M. Yoo, R. Saito, Y. Sendouda, K. Takahashi, and D. Yamauchi, *Femto-lensing due to a cosmic string*, Prog. Theor. Exp. Phys. **2013**, 013E01 (2013).

[163] N. S. Kapany, J. J. Burke, and K. Frame, *Diffraction by apertures of wavelength dimensions*, Appl. Opt. **4**, 1229 (1965).

[164] J. B. Peterson and T. Falk, *Gravitational lens interference*, Astrophys. J. **374**, L5 (1991).

[165] A. Gould, *Femtolensing of gamma-ray bursters*, Astrophys. J. **386**, L5 (1992).

[166] K. Yamamoto and K. Tsunoda, *Wave effect in gravitational lensing by a cosmic string*, Phys. Rev. D **68**, 1 (2003).

[167] B. P. Abbott, R. Abbott, T. D. Abbott, M. R. Abernathy, K. Ackley, C. Adams, P. Addesso, R. X. Adhikari, V. B. Adya, C. Affeldt, et al., *Exploring the sensitivity of next generation gravitational wave detectors*, Class. Quantum Gravity **34**, 044001 (2017).

[168] C. Caprini, M. Hindmarsh, S. Huber, T. Konstandin, J. Kozaczuk, G. Nardini, J. M. No, A. Petiteau, P. Schwaller, G. Servant, et al., *Science with the space-based interferometer eLISA. II: Gravitational waves from cosmological phase transitions*, J. Cosmol. Astropart. Phys. **2016(04)**, 001 (2016).

[169] Y. G. Ma, C. K. Ong, T. Tyc, and U. Leonhardt, *An omnidirectional retroreflector based on the transmutation of dielectric singularities*, Nat. Mater. **8**, 639 (2009).